ON THE ROLE OF 4-METHOXYPYRIDINE IN THE ELECTROCHEMICAL FORMATION OF PLASMONIC GOLD NANOPARTICLES

A Thesis Submitted to the College of Graduate and Postdoctoral Studies and Research

In Partial Fulfillment of the Requirements for the Degree of

Doctor of Philosophy

In the Department of Chemistry

University of Saskatchewan

Saskatoon

By

SAJNA SIMON

PERMISSION TO USE

In presenting this thesis in partial fulfillment of the requirements for a Postgraduate degree from the University of Saskatchewan, I agree that the Libraries of this University may make it freely available for inspection. I further agree that permission for copying of this thesis in any manner, in whole or in part, for scholarly purposes may be granted by the professor or professors who supervised my thesis work or, in their absence, by the Head of the Department or the Dean of the College in which my thesis work was done. It is understood that any copying or publication or use of this thesis or parts thereof for financial gain shall not be allowed without my written permission. It is also understood that due recognition shall be given to me and to the University of Saskatchewan in any scholarly use which may be made of any material in my thesis/dissertation.

Requests for permission to copy or to make other uses of materials in this thesis in whole or part should be addressed to:

Dean
College of Graduate and Postdoctoral studies
University of Saskatchewan
116 Thorvaldson building, 110 Science Place
Saskatoon, Saskatchewan S7N 5C9
Canada

Or

Department of Chemistry
110 Science Place
University of Saskatchewan
Saskatoon, Saskatchewan S7N 5C9
Canada

ABSTRACT

This thesis details an electrochemical approach to generate homogenous and densely populated films of anisotropic gold nanoparticles. The electrochemistry of coinage metals in the presence of the ligand 4-methoxypyridine (MOP) is described in detail and the role of the ligand in the formation of nanoparticle films on conductive substrates is discussed. The thesis demonstrates application of Stopped-flow UV-Vis spectroscopy to evaluate and study the kinetics of the homogenous chemistry of MOP with the gold salt precursor. It discusses the role of Au^{I} ions, and the different species involved in the complex Au-MOP system by thermodynamic and kinetic analysis. The thesis illustrates the excellent suitability of these nanoparticle films for surface-enhanced Raman scattering (SERS) applications utilizing near-IR excitation sources. The chronoamperometric study described in the thesis demonstrates the nucleation and growth mechanism of the electrodeposited gold nanostructures. Overall, the work described in this thesis outlines the advancement of electrochemical platforms that pertains to the potential applications of anisotropic gold nanostructures by tuning the shapes and size of the nanostructures.

ACKNOWLEDGEMENTS

First and foremost, I would like to express my sincere gratitude to Dr. Ian J. Burgess for his immense support and guidance from the very start of the program in helping me learn the basics of electrochemistry and throughout the course of my Ph.D. project.

I would like to extend my appreciation to the members of my advisory committee, Dr. Robert Scott, Dr. Lee Wilson, and Prof. Badea Ildiko for their valuable suggestions. I am also very thankful to my examination committee members.

My sincere thanks to University of Saskatchewan and the Department of Chemistry for giving me an opportunity to pursue my Ph.D. research with scholarships and teaching assistantship. I also acknowledge the financial support that I received from the Natural Sciences and Engineering Research Council of Canada during my maternity leave.

This journey of Ph.D. would not have been possible without the training from many experts of the University of Saskatchewan. I would like to thank Ms. Rhonda Sobchishin and Dr. Eiko Kawamura (Western College of Veterinary Medicine) for their training and assistance with TEM and SEM, and Scott Group for the use of UV-Vis spectrometer. Special thanks to Dr. Alexandra Bartole-Scott, Dr. Valarie MacKenzie, and Dr. Pia Wennek for their teaching assistantships.

I need to thank all the former and present members of Burgess Group for creating an ambient working atmosphere that never let me down and made each day in my journey full of joyful moments. I would like to express my appreciation to other faculty, staff and students who helped me one way or another in fulfilling my dream.

Finally, my deepest appreciation to my family who strongly supported me through this journey. The unwavering love and support that my two-year-old daughter, Sitara, gave me was far beyond my understanding as an adult. I would not have completed this journey, without the support of my husband James, my pillar of strength and I will be grateful to you forever.

DEDICATION

To James and Sitara, for their love and patience.

TABLE OF CONTENTS

LIST OF TABLES

LIST OF FIGURES

LIST OF ABBREVIATIONS

ATP	4-aminothiophenol
CFT	Crystal Field Theory
CV	Cyclic Voltammetry
CTAB	cetyltrimethylammonium bromide
DAQ	Data Acquisition
DMAP	4,4-dimethylaminopyridine
EF	Enhancement Factor
ESI-MS	Electrospray Ionization Mass Spectrometry
FT-Raman	Fourier Transformed Raman Spectroscopy
ITO	Indium Tin Oxide
LSPR	Localised Surface Plasmon Resonance
MOP	4-methoxypyridine
OCP	Open Circuit Potential
Pb-UPD	Lead Under Potential Deposition
Py	Pyridine
SEM	Scanning Electron Microscopy
SERS	Surface Enhanced Raman Scattering
SPR	Surface Plasmon Resonance
TEM	Transmission Electron Microscopy
UPD	Under Potential Deposition
UV-Vis-NIR	Ultraviolet-Visible-Near Infra Red
XRD	X-ray Diffraction

CHAPTER 1

INTRODUCTION

Metal nanoparticles of the size regime 1-100 nm are the building blocks of many nano-based applications. Compared to bulk metals of the same element, nanoparticles often exhibit different physical and chemical properties and are potentially attractive for various technical applications in electronics, optics, and catalysis as well as sensing [1-5], biolabeling [6, 7] and drug delivery.[8, 9] Both the synthesis and application of metal nanoparticles have been discussed numerous times in the literature.[10-12] In most instances where the application of metal nanoparticles requires their dispersion in a liquid phase, capping agents, often called stabilizing agents, must cover the metal nanoparticle to prevent particle aggregation. There is a wide variety of capping agents such as surfactant molecules, polymers, small organic molecules, and simple anions[13] that play a primary role in stabilizing nanostructures from extensive colloidal aggregation. Although the primary role of a capping agent is to stabilize the metal nanoparticle, it has been only relatively recent that their role in directed shape formation has become more apparent.[14, 15] However, the fundamental knowledge needed to understand the role of the capping agent in the growth and stability of metal nanoparticles is greatly eclipsed by reports of empirical observations of selective particle shape formation. This is understandable given the inherent difficulty associated with measuring small molecule/ion adsorption on metal surfaces dispersed in a solution that often contains a large excess of the stabilizing species.

Nevertheless, the tools for quantifying molecular and ionic adsorption on well-defined metal surfaces are well-established in the electrochemical community. The theory and methodologies used to extract qualitative and quantitative information about adsorbed molecular layers are now well developed.[16, 17] The Burgess group was one of the first to use such electrochemical methods to understand the fundamentals of capping agent adsorption on metal surfaces and relate

the information extracted from millimeter sized electrodes to nanoparticle dispersions.[18] This group has advocated that electrochemical methods can benefit nanoparticle research by offering more profound understanding of the behaviour of stabilizers in nanoparticle synthesis.[19]

The work contained in this thesis was inspired by the initial goal to apply such methods to the study of the shape directing effects of a pyridine derivative (4-methoxypyridine, MOP) on the formation of gold nanoparticles. As will be demonstrated, the behaviour of MOP is far more multifaceted than originally expected and electrochemical methods coupled with chemical characterization tools offer an extensive analysis of the complex chemical system from which highly anisotropic metal nanoparticles can be formed both in solution and on electrode surfaces.

1.1. Objectives

The following objectives, which reflect different aspects related to highly anisotropic nanoparticle electrodeposition, were pursued as specific research goals.

1. To use an electrochemical approach to precisely control the reduction conditions and to generate homogenous and densely populated metal nanoparticle films that are anisotropic in nature.
2. To evaluate the kinetics and understand the homogenous chemistry of MOP with the gold salt precursor.
3. To understand the nucleation and growth mechanism of electrodeposited gold nanostructures.

1.2 Research background and literature review

1.2.1 Metal nanostructures

Metallic nanostructured materials are of tremendous interest for sensing, electronic, catalytic and biomedical applications. Many approaches are reported in the literature to synthesize metal nanostructures of various shapes and sizes.[20] Different possibilities in the various fields of applications opens up as the size, shape, and other physical properties, surface chemistry and functionalization of the metal nanostructures are altered.[21] Although metal nanostructures with

specific optical properties have been the interest of researchers for over a century, serious consideration need to be made in tuning the optical properties with high control.

1.2.1.1 Surface Plasmon Resonance

Plasmons are the collective oscillation of the free charge in a metal. The positive charge in the metal remains fixed, and conductive electrons are so delocalized as to be considered uncoupled from individual nuclei. When an external electric field (such as that carried by light) is incident on a metal, the free electrons on the surface of the metal collectively vibrate to give rise to surface plasmons if the incident light is resonant with the plasmon excitation conditions. This vibration of free electrons generates an electric field that oscillates at the same frequency of the external electric field, resulting in surface plasmon resonance, a phenomenon present at the surface of the metal. Localized surface plasmon resonance (LSPR) is a phenomenon that arises due to the confinement of a surface plasmon in a nanoparticle of a size comparable to or smaller than the wavelength of light used to excite the plasmon as shown in the Figure 1.1.[22]

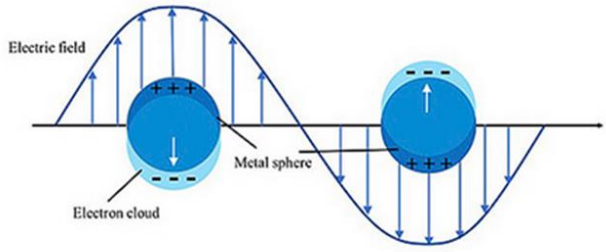

Figure 1.1. Schematic illustration of localized surface plasmon resonance (LSPR) of a spherical noble metal nanoparticle, resulting from the collective oscillations of delocalized electrons in response to an external electric field. Reprinted from an open access journal. Copyright © 2012 Yoochan Hong et al.

When the light irradiates the nanoparticles, the electric field generated on the metal varies with the presence of an adjacent nanoparticle. The generated electric field concentrates within the gap between two adjacent metal nanoparticles, whereas it is dispersed on either side of the metal nanoparticle perpendicular to the direction of the incident light for a single particle. As the gap

between the metal nanoparticles becomes narrow, the electric field density grows more prominent, as depicted in the Figure 1.2.[23]

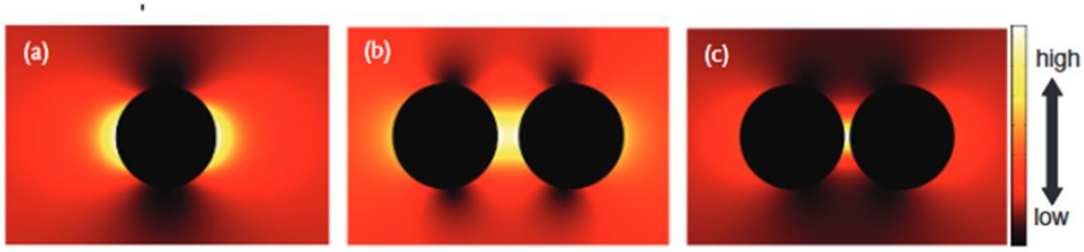

Figure 1.2. Images of electric field distribution on the gold nanoparticle surface under visible light irradiation visualised with Comsol Multiphysics 4.2a (a) Single gold nanoparticle (b) two gold nanoparticles with 4nm gap, and (c) two gold nanoparticles with 1nm gap. Reprinted with permission from Horikoshi, S. and N. Serpone. Introduction to nanoparticles. 2013. Wiley-VCH Verlag GmbH & Co. KGaA.

The wavelength corresponding to LSPR not only depends on the nature of the metal but also on the shape and the extent of aggregation of metal nanoparticles. For example, the wavelength corresponding to a surface plasmon band maximum for a spherical gold nanoparticle is 520-550 nm. So, when a colloidal solution of a gold nanoparticle is irradiated with light of wavelength ~ 520 nm, the particles absorb a green colour of the visible light and display a red colour, complementary to the green colour.

1.2.1.2 Size and Shape control of nanoparticles

The physical and chemical properties of the nanomaterial depend greatly on the size and shape of the nanoparticles. Thus, control over the nanoparticle structure becomes an important factor. Any change in the size and shape of the nanoparticles significantly changes its optical characteristics, and hence size distribution plays a significant role in optical applications. For example, as the size of the gold nanosphere increases, the surface plasmon resonance is shown to shift to a longer wavelengths (see Figure 1.3).[24]

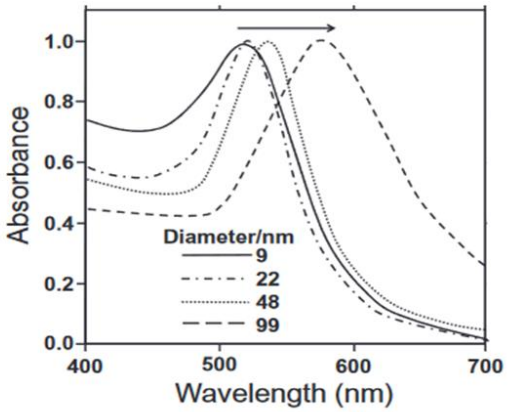

Figure 1.3. Visible-light spectra of gold nanospheres with various particle sizes. Reprinted with permission from Liz-Marzán, L.M., Tailoring Surface Plasmons through the Morphology and Assembly of Metal Nanoparticles. Langmuir, 2006. 22(1): p. 32-41. Copyright (2006) American Chemical Society.

Also, as the aspect ratio (length/width) of rod-shaped metal nanoparticles changes, the nature of the surface plasmon band also varies, as shown in Figure 1.4.[25] It is seen that a shift in the maximal absorption band to longer wavelength occurs with an increase in the aspect ratio. The change in the nanoparticle structure is a direct reflection of potential optical applications, and thus fabricating a nanoparticle of a target size and shape remains important, but often extremely challenging.

Generally, to prepare monodispersed nanoparticles, the nanoparticles must grow slowly once the seeds (nuclei) are generated rapidly.[26] If the nanoparticle size decreases, then an increase in the specific surface area and the nanoparticles' surface energy would lead to their aggregation. Consequently, once the nanoparticle has reached an optimal size, the addition of a stabilizing agent can prevent aggregation and stabilize the nanostructures. The surface of nanoparticles often derives charge when introduced into an aqueous (polar) or organic solvent. Thus, electrostatic repulsive forces prevent particle-particle aggregation. Aggregation is driven when the magnitude of attractive van der Waal forces between the charged surfaces is greater than the electrostatic repulsive forces. Even though the attractive forces are opposed by the electrostatic repulsive forces, the role of stabilising agent is enormous as they provide additional stability to the metal nanoparticles through steric hindrance.

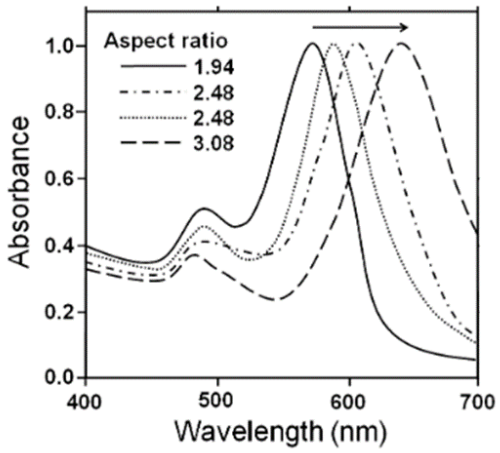

Figure 1.4. Visible-light spectra of Au rod-shaped nanoparticles with various aspect ratios. Reprinted with permission from Yu, et al., Gold Nanorods: Electrochemical Synthesis and Optical Properties. The Journal of Physical Chemistry B, 1997. 101(34): p. 6661-6664. Copyright (1997) American Chemical Society.

Different types of traditional stabilizing agents, such as citrate, thiols, and phosphines can stabilize homogeneous dispersions of metal nanoparticles. However, stabilizing agents can also play an important role in directing anisotropic growth during nanoparticle formation. For example, the use of cetyltrimethyl ammonium bromide (CTAB) is known to selectively adsorb onto the {100} and {110} crystal faces of gold nanoparticles allowing the {111} direction to grow, resulting in gold nanorods.[27-29] Thus, nanoparticles of various sizes and shapes have been controlled by the stabilizing agent's adsorption characteristics. The importance of interactions between a stabilising agent (sometimes also referred to as a ligand) and metal, which subsequently results in the asymmetry of the shapes of nanostructures are discussed in the next two sections.

1.2.1.3 Applications

The wide range of applications for different metal nanoparticles relative to the bulk metal is due to their unique characteristics. One of the topmost to be discussed is their optical function. With a change in the size and shape of the nanoparticle, the surface plasmon absorption band can be tuned across the visible and near IR region of the electromagnetic spectrum. Whereas bulk gold has a distinctive yellow colour, thin gold films have a characteristic blue colour in transmission.

However, this blue colour changes to shades of purple and red as the thickness decreases. Metal nanoparticles can act as surface-enhanced Raman scattering (SERS) agents for biomolecular imaging.[30] The localized field enhancement due to the use of metal nanoparticles provides a highly sensitive molecular detection platform for biomedical research.

As the nanoparticle diameter decreases, physical properties such as melting point and boiling point are also lowered. This brings the application of nanoparticles in micro-wiring. The electronic industry uses metal nanoparticle paste [31] for circuit pattern formation on a printed wired board. Since the wiring width is thin to a nano-level, the use of an inexpensive and shorter time method such as an ink-jet method could be advantageous over other typical methods such as metal evaporation. Other characteristics of metal nanoparticles worth noting are their mechanical and electrical functions. As the mechanical characteristics of a nanoparticle improve due to the volume, surface and quantum effects, mixing the nanoparticles with metals or ceramics improve mechanical strength.[32] Furthermore, with an improved electrical function such as resistance to extreme heat, metal nanoparticles can be applied to create high-temperature superconductivity materials.[33]

Another major application of metal nanoparticles is catalysis. In the nanoparticle regime, the specific surface area is large, which enhances the reaction efficiency. Particle size, shape, composition, and porosity are other characteristics that offer a potential heterogeneous catalytic application for metal nanoparticles. The effect of support enhances the thermal stability of the catalyst and thus provides improved surface area characteristics.[34] For example, it has been reported that CO oxidation by pure gold particles exhibited no catalytic activity at 227 °C, whereas gold nanoparticles dispersed on titania support showed acceptably high catalytic activity at lower temperatures.[35] In many cases, a highly active catalyst with high selectivity can be prepared.

1.2.2 Role of ligand stabilizers

Metal nanostructures with high surface area to volume, when unprotected, are thermodynamically quite unstable and hence need the role of ligand stabilizers to protect them. These stabilizers protect the metal nanostructures by preventing them from aggregation and flocculation. Stable metal nanostructures can be synthesized either in an organic or aqueous phase, depending on the nature

of the ligand stabilizers. Alkanethiols, being nonpolar in nature, aid synthesis of metal nanoparticles in organic solvents and citrate ions being charged allows synthesis in aqueous solutions. Importantly, if the ligands on the capped metal nanoparticles can be exchanged, the stabilizers can impart new chemistry onto the metal nanoparticles.

Labile ligand stabilizers with amino functionalities enable complete ligand exchange in solutions of varying polarity with ease. Here, the term 'labile' refers to the relative strength of the metal-ligand bond, or it is also referred to as the facility for the metal-ligand bond to be broken easily. Physisorbed ligands offer greater advantages over other ligands in the post-synthesis applications through easy nanoparticle phase transfer and subsequent exchange of stabilizer molecules for others with preferred surface chemistry.[36] This is largely in contrast to alkanethiols [37-41] that protect the metal nanostructures through a covalent metal-sulphur bond. Covalent bond interactions between the thiols and the metals also introduce the possibility of modification of the chemical functionality of the nanoparticle surface through judicious choice of the terminating group on the thiol molecules. However, post-synthesis surface modification is difficult due to the strong bonding character of the metal-sulphur bond.[42] Alternatively, ionic ligand stabilizers such as citrate ions [43] rely on electrostatic repulsive forces to prevent particle aggregation. In recent years, there have been several reports of metal nanoparticles' being stabilized by ligands with amino functionalities such as pyridine derivatives.[36, 44-47] These capped (protected) metal nanostructures are relatively stable but, due to the weaker nature of the physisorption metal-ligand interaction, these protecting layers are much more easily replaced by immersing the particles in solutions containing an excess of new ligand.

1.2.3 Nanoparticle anisotropy

Non-spherical metal nanostructures such as nanorods, nanoplates, nanoprisms, and nanopods with unique shape-dependent properties and functionalities are generally termed as anisotropic metal nanostructures (Figure 1.5).[48]

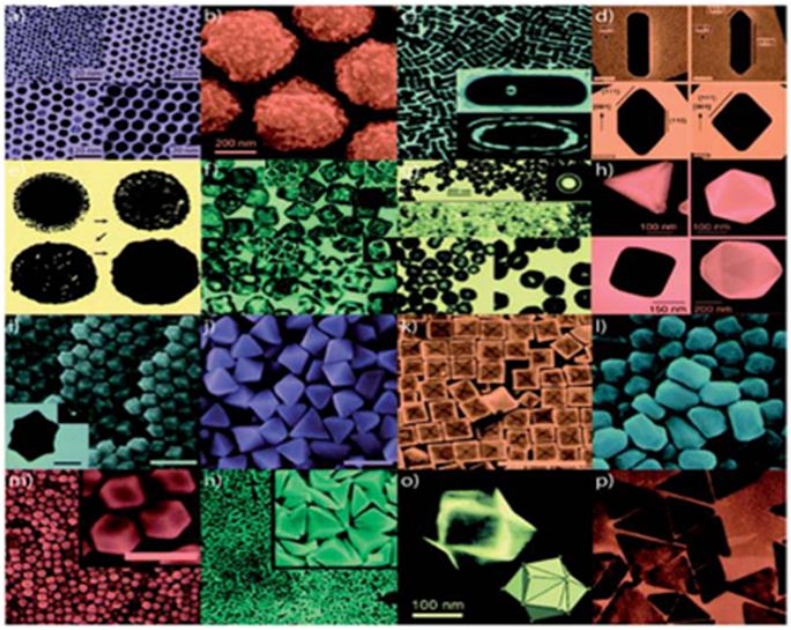

Figure 1.5. Various gold nanostructures with potential biomedical applications. Reproduced from Huang, Y., et al., Biomedical nanomaterials for imaging-guided cancer therapy. Nanoscale, 2012. 4(20): p. 6135-6149 with permission from The Royal Society of Chemistry.

Capping agents not only produce stable nanostructures but also promote anisotropy by selective adsorption. These anisotropic metal nanostructures continue to be the subject of active research due to their wide applications in photonic devices [19], electronics [49], electrocatalysis [50], and medicine.[51] Controlling the shapes of nanostructures and promoting anisotropy is challenging as it involves both kinetic and thermodynamic factors, as explained by Xia *et al.* [14] The concept, typically used in literature, of thermodynamic versus kinetic controlled nanocrystal synthesis is illustrated in Figure 1.6.[50, 52] The schematic representation provides the current insight into the shape evolution of colloidal metal nanocrystals with the use of well-defined seeds. Here, the synthesis of nanocrystals is considered as a chemical reaction, and the term "reactants" refers to the reduced metal atoms derived from the precursor ions and the term "products" as the anisotropic nanocrystals.

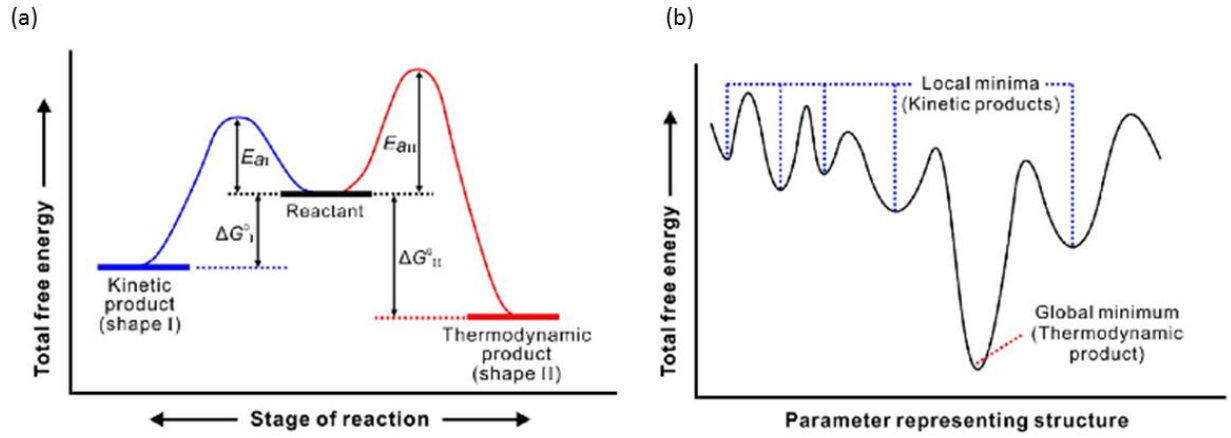

Figure 1.6. Schematic illustrations of two different scenarios of thermodynamic versus kinetic control that involve (a) two parallel reactions (b) a series of sequential reactions. Reprinted with permission from Xia, Y., X. Xia, and H.-C. Peng, Shape-Controlled Synthesis of Colloidal Metal Nanocrystals: Thermodynamic versus Kinetic Products. J. Am. Chem. Soc., 2015. 137(25): p. 7947-7966. Copyright (2015) American Chemical Society.

Figure 1.6a represents the scenario where anisotropic nanocrystals are formed from multiple parallel reactions. In this case, the product I refers to a thermodynamically less stable species relative to product II, however the activation energy barrier involved in the formation of the product I is lower. Hence, product I is favoured if the reaction is conducted under kinetic conditions and product II under thermodynamic conditions. According to the Arrhenius equation, reaction rate constant$= Ae^{-Ea/RT}$, and the effective way to reduce the activation energy is by elevating the reaction temperature. As a result, the simplest way to prefer thermodynamic and kinetic products will be when the reactions are favoured at lower and higher temperatures, respectively. Figure 1.6b represents the reality where the formation of anisotropic nanocrystals occurs through a set of sequential reactions. The energy landscape illustrated in this Figure 1.6b represents the formation of different products with different chemical compositions but the same elemental composition. However, the thermodynamically controlled product in both figures is the one with the lowest Gibbs free energy (global minimum). This basic concept, as explained by Xia and co-workers [14], shows how the diversified shapes in the colloidal metal nanocrystals can be obtained by adjusting various thermodynamic or kinetic parameters.

Though it is challenging to control the kinetic conditions of nanoparticle synthesis, it is not impossible to overcome the normal tendency to form the much thermodynamically favoured quasi-spherical nanostructures.[15] The role of capping agents in the preferential growth along a crystallographic facet leading to shape anisotropy has been explained extensively in the literature. An example is the preferential C_{16}TAB adsorption on {100} surfaces and allowing preferred Au^0 deposition on the uncovered {111} facets resulting in gold nanorods [53] which was already described above. Another example is the preferential adsorption of piperazine on non {111} facets leading to highly branched Au metal nanocrystals formed by the reduction of gold salts in the presence of HEPES buffer [54]. There are also several reports of preferential peptide adsorption on high-energy {110} facets leading to the observation of nanocrystals of different shapes [55].

Although chemical reduction methods are the most commonly used means of synthesizing metal nanostructures, there is considerable appeal in applying electrochemical methods. An electrochemical approach can more precisely control the thermodynamic driving force for the conversion of metal ion into metal atom. Furthermore, the kinetics of electron transfer processes are inherently linked to the applied electrical potential through formulism's such as the Butler-Volmer equation or Marcus theory. Thus, in principle, electrochemistry offers an exciting means to the formation of anisotropic metal nanostructures and the generation of homogenous metal nanoparticle films of controlled surface density.

1.3 The motivation for thesis work

The impetus for this body of work derives from previous studies of homogenous ligand stabilized gold nanoparticles. Danger *et al*. described the use of 4-dimethyl aminopyridine (DMAP) to synthesize anisotropic gold nanocrystals via the borohydride reduction of gold (III) salts.[18] In this work, it was proposed on the basis of electrosorption and potentiometry studies, that anisotropic nanocrystal growth resulted from the formation of Au^I intermediates and the selective adsorption of pyridine derivatives on specific crystallographic facets of the growing nanoparticles. One of the significant challenges faced in the synthesis described by Danger *et al.* was the difficulty in achieving control over the seed-growth conditions. The conventional method of forming citrate capped gold seeds resulted in small gold nanoparticles in the presence of DMAP, showing no signs of anisotropy. Whereas, the direct addition of $NaBH_4$ (borohydride) to a solution

containing $AuCl_4^-$ and a large excess of DMAP resulted in coloured dispersions, as shown in the Figure 1.7a, highly indicative of anisotropic metal nanoparticle formation.

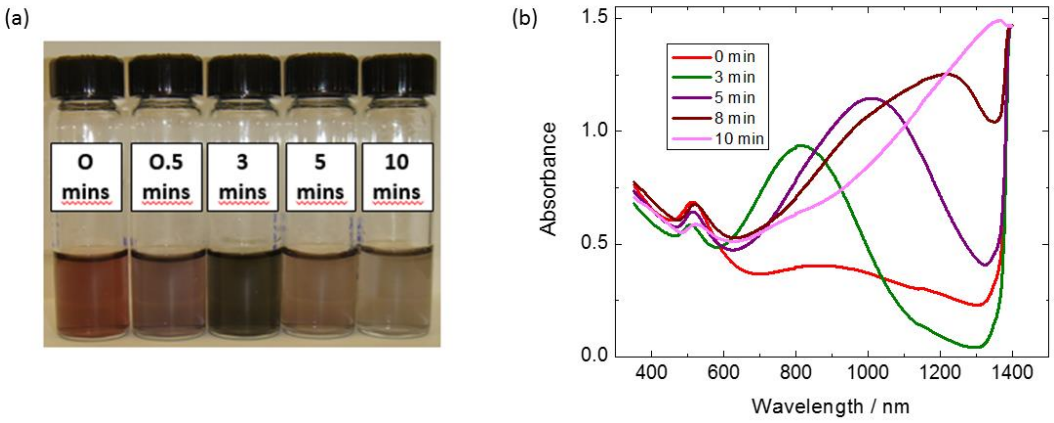

Figure 1.7. (a) Color of colloidal gold solutions resulting from the addition of borohydride to $HAuCl_4$-DMAP mixtures and (b) UV-vis-NIR optical spectra of the resulting dispersions. The time between mixing the Au^{III} and DMAP and the addition of borohydride (τ) is indicated. Reprinted with permission from Danger, B.R., et al., Electrochemical Studies of Capping Agent Adsorption Provide Insight into the Formation of Anisotropic Gold Nanocrystals. ACS Nano, 2012. 6(12): p. 11018-11026. Copyright (2012) American Chemical Society.

Instead of immediate precipitation of Au^0, which usually occurs due to the strong reduction potential of borohydride, coloured solutions dependent on the time-lapse, τ, between the preparation of the $AuCl_4^-$-DMAP mixture and the addition of the reducing agent were observed. Ruby-red colours were observed for smaller values of τ, which is indicative of smaller spherical particles and brown to taupe coloured solutions were observed for longer values of τ indicating anisotropy in the nanostructures. Vis-NIR spectra revealed a second plasmon mode that redshifted with longer τ values indicating increasing anisotropy in the nanostructures as a function of τ. TEM images, shown in Figure 1.8, provided an explanation for the varying optical appearances of the gold dispersions. Four major shapes, reflecting increasing τ values, were dominant from the TEM images that included small similar-sized nanoparticles, quasi-rod-shaped particles, boomerangs, and tripods. Further investigation of the tripodal structures, observed only at larger values of τ, with high-resolution TEM showed the preferential growth along the <111> directions and was primarily supported by the literature for Au [54] and Pt [55-58] nanopods.

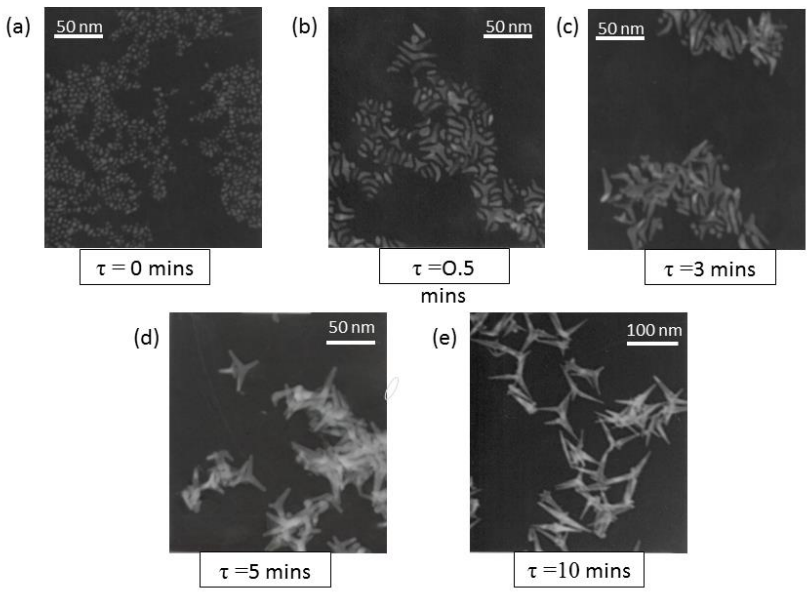

Figure 1. 8. Transmission electron micrographs of Au nanocrystals formed from the borohydride reduction of $HAuCl_4$-DMAP mixtures as a function of τ. (a) τ = 0 min, (b) τ = 0.5 min, (c) τ = 3 min, (d) τ = 5 min, and (e) τ =10 min. Reprinted with permission from Danger, B.R., et al., Electrochemical Studies of Capping Agent Adsorption Provide Insight into the Formation of Anisotropic Gold Nanocrystals. ACS Nano, 2012. 6(12): p. 11018-11026. Copyright (2012) American Chemical Society.

Even though the observation of anisotropic particles was attributed to the ability of the adsorbed DMAP to direct growth, this work did not provide an answer as to why these shapes were preferentially rod-like for smaller values of τ and multipodal for larger values of τ.

The role of DMAP was purported to be multifunctional in forming the anisotropic nanoparticles. Its role as a stabilizer and in creating lower gold monomer deposition rates onto growing seed crystals that resulted in anisotropy was reported in Danger *et al.'s* work. There were a few important aspects explained in the mechanism of seed growth behaviour. This included the initial reduction of Au^{III} ions by the borohydride that resulted in the number density of the Au^0 monomers, the slow reduction of Au^{III} to Au^I by DMAP over a certain period of time and the electrochemical potential of the solution during secondary growth. The formation of various shapes of the nanoparticles eventually produced is explained due to the slow, anisotropic, growth conditions on

a variety of seed structures. Thus, the work describes the formation of anisotropic gold nanostructures under conditions of thermodynamic, kinetic, and mass-transport control.

The two significant challenges met by the authors were a) the use of borohydride in reducing the gold salt and b) the use of DMAP as the capping agent. The non-reproducibility of the results due to the use of borohydride concentration was a critical issue. The change in the reduction strength with every use of borohydride was crucial as it affects the growth of the nanocrystals. This change in the reduction strength was proposed to be eliminated by employing an electrochemical approach, where the potential applied to an electrode surface offers a precisely controllable variable that can control the driving force that reduces gold salts as opposed to the variability of borohydride in the wet chemistry method.

The high basicity of DMAP complicates the Au(III) pyridine chemistry as high pH can lead to rapid ligand exchange and the formation of various $Au(OH)_xCl_{(4-x)}$ species and the precipitation of poorly soluble $Au(OH)_3$. Therefore, another approach proposed in this thesis was the use of a less basic pyridine ligand in stabilizing the metal nanoparticles. The highly electron-donating behaviour of the para-substituted tertiary amine of DMAP makes it highly basic with a pKa value of 9.7 and readily protonates in aqueous solutions. Therefore, substituting DMAP with 4-methoxypyridine (MOP), whose pKa value is 6.6, was introduced. The binding energies of both MOP and DMAP on gold are similar.[59] Although studies also show that the adsorption of pyridine derivatives on Au {111} tends to increase with increasing electron-donating ability of the *para* substituent.[60] In a related study, MOP was found to exhibit the same preferential adsorption behaviour [61] as its more basic analog.

Thus, one of the primary goals of this thesis was to test the hypothesis that the electrochemical reduction of Au ions from solutions in the presence of MOP would allow the creation of well-defined arrays of highly anisotropic gold nanoparticles. This thesis will present the electrodeposition of anisotropic gold nanostructures controlled by the presence of a pyridine capping agent, 4-methoxypyridine (*Py* derivative) followed by the electrochemical, kinetic and nucleation studies on MOP stabilized gold nanoparticles.

1.4 Overview of thesis

This thesis consists of eight chapters. A brief introduction to the research background and literature review has been provided in this Chapter. Details of the experimental methods employed are provided in Chapter 2. Chapter 3 describes a survey carried out on the electrochemistry of different metal-pyridine systems. Chapter 3 also provides an introduction and a literature review on the different coinage metal-pyridine systems but, importantly, indicates the unique behaviour of the Au-MOP system. The uniqueness of the gold-pyridine system is explored further in the subsequent chapters of the thesis.

Chapter 4 focuses on understanding the homogenous chemistry of 4-methoxypyridine with the gold salt of interest. Two different methods in UV-Vis analysis: the stopped-flow method and the scan method are used to provide an understanding of the kinetics of the Au-MOP system under open circuit conditions and hence gives a kinetic model for important, non-electrochemical reactions. Chapter 5 details the electrochemical formation of highly anisotropic gold nanostructures. An in-depth voltammetric study is performed for the Au-MOP complexes and reveals the important role of Au(I) intermediates in the electrodeposition of gold nanostructures. The characterization of these nanostructures was performed using UV-Vis-NIR analysis, XRD, Pb underpotential deposition and SEM and is described in Chapter 6. This chapter also describes the use of these nanostructures for surface enhanced spectroscopy.

Chapter 7 describes a nucleation and growth study of 4-methoxypyridine stabilized gold nanostructures. Chronoamperometric analysis was performed to understand the type of nucleation that led to the growth of these nanostructures The current transients at lower overpotential are shown to fit well to the limiting case of instantaneous nucleation and growth whereas the transients at larger overpotentials are intermediate between the two limiting scenarios - instantaneous and progressive nucleation and growth. The importance of this study, as it helps to tune the size and shapes of the nanostructures, is revealed in this chapter. Finally, concluding remarks on the work presented in this thesis and scope for future research in this direction are discussed in Chapter 8.

1.5 References

1. Baron, R., M. Zayats, and I. Willner, *Dopamine-, L-DOPA-, Adrenaline-, and Noradrenaline-Induced Growth of Au Nanoparticles: Assays for the Detection of Neurotransmitters.* Anal. Chem., 2005. **77**(6): p. 1566-1571.

2. Katz, E., I. Willner, and J. Wang, *Electroanalytical and bioelectroanalytical systems based on metal and semiconductor nanoparticles*. Electroanalysis, 2004. **16**(1-2): p. 19-44.

3. Murphy, L., Biosensors and bioelectrochemistry. Curr. Opin. Chem. Biol., 2006. **10**(2): p. 177-184.

4. Storhoff, J.J. and C.A. Mirkin, *Programmed Materials Synthesis with DNA*. Chem. Rev. (Washington, D. C.), 1999. **99**(7): p. 1849-1862.

5. Wang, J., *Nanomaterial-based electrochemical biosensors.* Analyst (Cambridge, U. K.), 2005. **130**(4): p. 421-426.

6. Schultz, S., et al., *Single-target molecule detection with nonbleaching multicolor optical immunolabels.* Proc. Natl. Acad. Sci. U. S. A., 2000. **97**(3): p. 996-1001.

7. Tan, M., et al., *Development of functionalized fluorescent europium nanoparticles for biolabeling and time-resolved fluorometric applications*. J. Mater. Chem., 2004. **14**(19): p. 2896-2901.

8. Sandhu, K.K., et al., *Gold Nanoparticle-Mediated Transfection of Mammalian Cells. Bioconjugate Chem.*, 2002. **13**(1): p. 3-6.

9. Tokareva, I. and E. Hutter, *Hybridization of Oligonucleotide-Modified Silver and Gold Nanoparticles in Aqueous Dispersions and on Gold Films*. J. Am. Chem. Soc., 2004. **126**(48): p. 15784-15789.

10. Daniel, M.-C. and D. Astruc, *Gold Nanoparticles: Assembly, Supramolecular Chemistry, Quantum-Size-Related Properties, and Applications toward Biology, Catalysis, and Nanotechnology*. Chem. Rev. (Washington, DC, U. S.), 2004. **104**(1): p. 293-346.

11. McConnell, W.P., et al., *Electronic and optical properties of chemically modified metal nanoparticles and molecularly bridged nanoparticle arrays*. J. Phys. Chem. B, 2000. **104**(38): p. 8925-8930.

12. Shipway, A.N., E. Katz, and I. Willner, *Nanoparticle arrays on surfaces for electronic, optical, and sensor applications*. ChemPhysChem, 2000. **1**(1): p. 18-52.

13. Xiao, J. and L. Qi, *Surfactant-assisted, shape-controlled synthesis of gold nanocrystals.* Nanoscale, 2011. **3**(4): p. 1383-1396.

14. Xia, Y., X. Xia, and H.-C. Peng, *Shape-Controlled Synthesis of Colloidal Metal Nanocrystals: Thermodynamic versus Kinetic Products*. J. Am. Chem. Soc., 2015. **137**(25): p. 7947-7966.

15. Xia, Y., et al., *Shape-controlled synthesis of metal nanocrystals: simple chemistry meets complex physics?* Angew. Chem., Int. Ed., 2009. **48**(1): p. 60-103.

16. Damaskin, B.B., A.N. Frumkin, and A.V. Chizhov, *Generalized model of the surface layer for the case of adsorption of organic molecules on the electrode*. J. Electroanal. Chem. Interfacial Electrochem., 1970. **28**(1): p. 93-104.

17. Grahame, D.C., *The electrical double layer and the theory of electrocapillarity*. Chem Rev, 1947. **41**(3): p. 441-501.

18. Danger, B.R., et al., *Electrochemical Studies of Capping Agent Adsorption Provide Insight into the Formation of Anisotropic Gold Nanocrystals*. ACS Nano, 2012. **6**(12): p. 11018-11026.

19. Dietl, T. and H. Ohno, *Engineering magnetism in semiconductors*. Mater. Today (Oxford, U. K.), 2006. **9**(11): p. 18-26.

20. Qazi, U. and R. Javaid, *A Review on Metal Nanostructures: Preparation Methods and Their Potential Applications*. Advances in Nanoparticles, 2016. **05**: p. 27-43.

21. Castagnola, V., et al., *Towards a classification strategy for complex nanostructures.* Nanoscale Horiz., 2017. **2**(4): p. 187-198.

22. Hong, Y., et al., *Review Article Nanobiosensors Based on Localized Surface Plasmon Resonance for Biomarker Detection*. Journal of Nanomaterials, 2013. **759830**.

23. Horikoshi, S. and N. Serpone. *Introduction to nanoparticles*. 2013. Wiley-VCH Verlag GmbH & Co. KGaA.

24. Liz-Marzán, L.M., *Tailoring Surface Plasmons through the Morphology and Assembly of Metal Nanoparticles*. Langmuir, 2006. **22**(1): p. 32-41.

25. Yu, et al., Gold Nanorods: *Electrochemical Synthesis and Optical Properties*. The Journal of Physical Chemistry B, 1997. **101**(34): p. 6661-6664.

26. Shah, D.O., *Fine Particles: Synthesis, Characterization, and Mechanisms of Growth.* Edited by T. Sugimoto, Surfactant Science Series, Vol. 92. Journal of Nanoparticle Research, 2002. **4**(1): p. 179-179.

27. Jana, N.R., L. Gearheart, and C.J. Murphy, *Wet Chemical Synthesis of High Aspect Ratio Cylindrical Gold Nanorods*. The Journal of Physical Chemistry B, 2001. **105**(19): p. 4065-4067.

28. Jana, N.R., L. Gearheart, and C.J. Murphy, *Evidence for Seed-Mediated Nucleation in the Chemical Reduction of Gold Salts to Gold Nanoparticles*. Chemistry of Materials, 2001. **13**(7): p. 2313-2322.

29. Nikoobakht, B. and M.A. El-Sayed, *Evidence for Bilayer Assembly of Cationic Surfactants on the Surface of Gold Nanorods*. Langmuir, 2001. **17**(20): p. 6368-6374.

30. Ando, J. and K. Fujita, *Metallic nanoparticles as SERS agents for biomolecular imaging*. Curr. Pharm. Biotechnol., 2013. **14**(2): p. 141-149.

31. Kravchuk, O., et al., *Sintering Methods of Inkjet-Printed Silver Nanoparticle Layers*. 2018. p. 317-339.

32. Wu, Q., et al., *Mechanical properties of nanomaterials: A review*. Nanotechnology Reviews, 2020. **9**(1): p. 259.

33. Jasim, S.E., et al., *Fabrication of Superconducting YBCO Nanoparticles by Electrospinning*. Procedia Engineering, 2016. **148**: p. 243-248.

34. Tauster, S.J., et al., *Strong interactions in supported-metal catalysts.* Science, 1981. **211**(4487): p. 1121-5.

35. Masatake, H., et al., *Novel Gold Catalysts for the Oxidation of Carbon Monoxide at a Temperature far Below 0 °C*. Chemistry Letters, 1987. **16**(2): p. 405-408.

36. Gittins, D.I. and F. Caruso, *Spontaneous phase transfer of nanoparticulate metals from organic to aqueous media.* Angew. Chem., Int. Ed., 2001. **40**(16): p. 3001-3004.

37. Ackerson, C.J., P.D. Jadzinsky, and R.D. Kornberg, *Thiolate Ligands for Synthesis of Water-Soluble Gold Clusters*. J. Am. Chem. Soc., 2005. **127**(18): p. 6550-6551.

38. Chen, S. and K. Kimura, *Synthesis and Characterization of Carboxylate-Modified Gold Nanoparticle Powders Dispersible in Water*. Langmuir, 1999. **15**(4): p. 1075-1082.

39. Cliffel, D.E., et al., *Mercaptoammonium-Monolayer-Protected, Water-Soluble Gold, Silver, and Palladium Clusters*. Langmuir, 2000. **16**(25): p. 9699-9702.

40. Shon, Y.-S., W.P. Wuelfing, and R.W. Murray, *Water-Soluble, Sulfonic Acid-Functionalized, Monolayer-Protected Nanoparticles and an Ionically Conductive Molten Salt Containing Them*. Langmuir, 2001. **17**(4): p. 1255-1261.

41. Templeton, A.C., W.P. Wuelfing, and R.W. Murray, *Monolayer-Protected Cluster Molecules*. Accounts of Chemical Research, 2000. **33**(1): p. 27-36.

42. Di Felice, R. and A. Selloni, *Adsorption modes of cysteine on Au(111).* Thiolate, amino-thiolate, disulfide. J. Chem. Phys., 2004. **120**(10): p. 4906-4914.

43. Turkevich, J., P.C. Stevenson, and J. Hillier, *A study of the nucleation and growth processes in the synthesis of colloidal gold*. Discussions of the Faraday Society, 1951. **11**(0): p. 55-75.

44. Gandubert, V.J. and R.B. Lennox, *Assessment of 4-(dimethylamino)pyridine as a capping agent for gold nanoparticles*. Langmuir, 2005. **21**(14): p. 6532-6539.

45. Gittins, D.I., et al., *Dense nanoparticulate thin films via gold nanoparticle self-assembly*. Adv. Mater. (Weinheim, Ger.), 2002. **14**(7): p. 508-512.

46. Larson, I., et al., *Use of Atomic Force Microscopy Force Measurements to Monitor Citrate Displacement by Amines on Gold in Aqueous Solution.* Langmuir, 1997. **13**(9): p. 2429-2431.

47. Yu, A., et al., *Nanostructured Electrochemical Sensor Based on Dense Gold Nanoparticle Films*. Nano Lett., 2003. **3**(9): p. 1203-1207.

48. Huang, Y., et al., *Biomedical nanomaterials for imaging-guided cancer therapy*. Nanoscale, 2012. **4**(20): p. 6135-6149.

49. Murphy, C.J., et al., *Surfactant-directed synthesis and optical properties of one-dimensional plasmonic metallic nanostructures*. MRS Bull., 2005. **30**(5): p. 349-355.

50. Oh, A., et al., *Skeletal Octahedral Nanoframe with Cartesian Coordinates via Geometrically Precise Nanoscale Phase Segregation in a Pt@Ni Core-Shell Nanocrystal.* ACS Nano, 2015. **9**(3): p. 2856-2867.

51. Li, N., P. Zhao, and D. Astruc, *Anisotropic Gold Nanoparticles: Synthesis, Properties, Applications, and Toxicity.* Angew. Chem., Int. Ed., 2014. **53**(7): p. 1756-1789.

52. Simek, J.W. and L.G. Wade, *Solutions manual : L.G. Wade, Jr., Organic chemistry,* second edition. 1991, Englewood Cliffs, N.J.: Prentice Hall.

53. Nikoobakht, B. and M.A. El-Sayed, *Preparation and growth mechanism of gold nanorods (NRs) using seed-mediated growth method.* Chem. Mater., 2003. **15**(10): p. 1957-1962.

54. Xie, J., J.Y. Lee, and D.I.C. Wang, *Seedless, Surfactantless, High-Yield Synthesis of Branched Gold Nanocrystals in HEPES Buffer Solution.* Chem. Mater., 2007. **19**(11): p. 2823-2830.

55. Ruan, L., et al., *Synthesis of Platinum Single-Twinned Right Bipyramid and {111}-Bipyramid through Targeted Control over Both Nucleation and Growth Using Specific Peptides*. Nano Lett., 2011. **11**(7): p. 3040-3046.

56. Chen, J., T. Herricks, and Y. Xia, *Polyol synthesis of platinum nanostructures: Control of morphology through the manipulation of reduction kinetics.* Angew. Chem., Int. Ed., 2005. **44**(17): p. 2589-2592.

57. Chen, J., B.J. Wiley, and Y. Xia, *One-dimensional nanostructures of metals: large-scale synthesis and some potential applications*. Langmuir, 2007. **23**(8): p. 4120-4129.

58. Li, Y. and Y. Huang, *Morphology-Controlled Synthesis of Platinum Nanocrystals with Specific Peptides*. Adv. Mater. (Weinheim, Ger.), 2010. **22**(17): p. 1921-1925.

59. Lange, H., et al., *Adsorption behavior of 4-methoxypyridine on gold nanoparticles*. Langmuir, 2011. **27**(11): p. 7258-7264.

60. Mollenhauer, D., et al., *Accurate quantum-chemical description of gold complexes with pyridine and its derivatives.* J. Comput. Chem., 2011. **32**(9): p. 1839-1845.

61. Unni, B., S. Simon, and I.J. Burgess, *Electrochemical investigations of 4-methoxypyridine adsorption on Au(111) predict its suitability for stabilizing Au nanoparticles.* Langmuir, 2015. **31**(36): p. 9882-9888.

CHAPTER 2

EXPERIMENTAL METHODS

The primary objective of this chapter is to describe the instrumental set-up and methods that were used in the experimental aspects of this thesis (Chapter 3-7). Although many of the analysis are well-established techniques, efforts have been made to describe important adaptations used for this study. The main methods described in this chapter include the electrochemical set-up, chronoamperometric measurements followed by the basic information on several characterization techniques.

2.1 Electrochemical set-up

A computer-controlled system, consisting of HEKA PG590 potentiostat was used for all the electrochemistry experiments. Data were collected using a multi-function DAQ card (PCI 6251 M Series, National Instruments) and in-house software written by the Burgess group in the LABVIEW environment.

2.1.1 Electrochemical cell

The electrochemical cell was made of glass and had a solution capacity of 25 mL. It consists of two units: the main cell unit, which is shaped like a train and hence nicknamed the train cell (Figure 2.1) and a mixing unit. The electrochemical studies were performed in the main cell unit and the mixing unit was used to mix all the solutions and degas prior to any electrochemical measurements. The train cell has four joints on the top, two joints on either side (10 mm joints) and three ground joints at the bottom. One of the 10 mm side joints is connected to the salt bridge, which is also made of glass. Two of the top joints are used to allow an argon purge of the electrolyte solution

and create an argon blanket on top of the electrolyte surface, which is, in turn, vented through an exhaust bubbler connected to one of the top 10 mm joints. The other side joint is used for the counter electrode. The bottom three ground joints are for the working electrodes. Mostly, one working electrode is used at a time but the presence of three working electrodes allows for serial measurement without the need to disassemble the cell. This was particularly useful in experiments where it was desirable to make measurements on fresh pieces of ITO, uncontaminated by previous gold deposition. The remaining top joint is connected to the mixing unit. The mixing unit has three top joints. One of the mixing unit joints is used for purging argon of the electrolyte solution once mixed. This extra purge of the electrolyte solution before it enters the train cell helps to exclude any dissolved oxygen. Any analytically useful electrochemical signal is obtained in the absence of dissolved oxygen and hence degassing is an important step prior to an electrochemical measurement. The electrochemical cell was enclosed in a Faraday cage – a grounded conductive shield made of copper mesh. The Faraday cage protects the electrochemical set up against electrostatic and electromagnetic interferences from external sources.

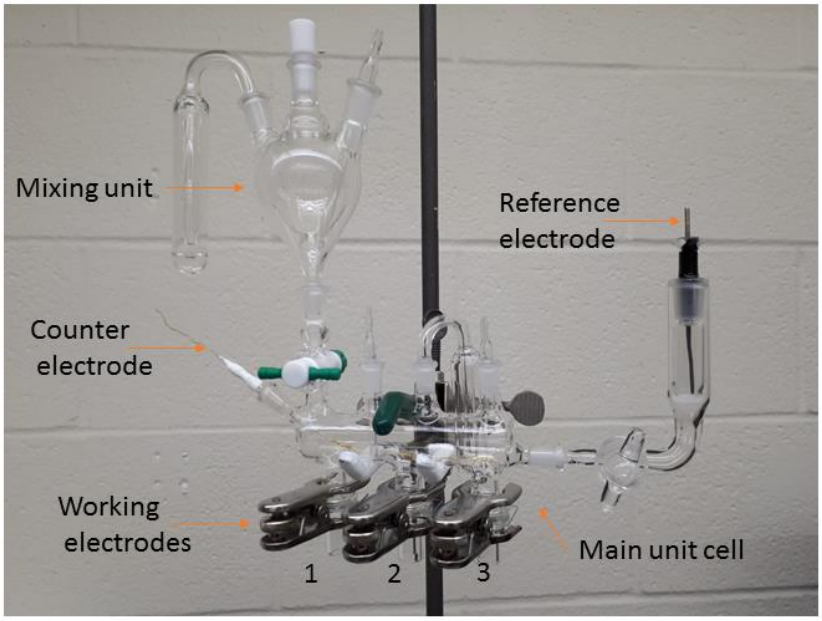

Figure 2.1. Electrochemical cell set-up comprising of the main cell unit and the mixing unit.

All glassware for the electrochemical cell, including the salt bridge, was washed in a hot acid bath containing 1:3 v/v mixture of nitric acid and sulphuric acid and then rinsed thoroughly with Milli-Q water before use. All other glassware used for preparing solutions needed for the electrochemical measurements are also washed in a similar manner. Electrolyte and all other aqueous solutions were prepared using Milli-Q water of resistivity 18.2MΩ cm.

2.1.2 Electrodes

A saturated silver-silver chloride electrode (Ag/AgCl) connected to the train cell through a salt bridge was used as a reference electrode. All potentials reported in this thesis were measured with respect to the Ag/AgCl saturated KCl reference potential. A gold coil wire, flame annealed before each experiment, was used as a counter electrode. Indium Tin Oxide (ITO) coated glass electrodes were used as the working electrodes. These working electrodes, with a sheet resistance of 15-25 Ω.sq., were commercially purchased from Delta Technologies. Prior to each experiment, the ITO-coated glass was sonicated in Milli-Q water for 15 minutes and dried in a stream of argon.

2.2 Cyclic Voltammetry

To record a cyclic voltammogram, a linear voltage scan (typically 20mV s^{-1}) was applied to the working electrode, and the resulting current was recorded as a function of the electrode potential. Any changes on the electrode surface were reflected in the recorded current, and this was used to probe reactions that involve electron transfer processes.

2.3 Chronoamperometry

As the name implies, chronoamperometry is the measurement of current with time. These studies were particularly useful in probing the nucleation and initial stages of nanoparticle growth on the ITO substrates as described in Chapters 5 and 7. A schematic diagram outlining double potential step chronoamperometry is shown in Figure 2.2. Panel (a) shows the sequence of potential steps applied to the working electrode. The electrode potential was preset to attain a constant base value (E_b) for time (t_b), where no electrochemical process are operative. Then the working electrode potential was stepped to a potential E_c for a period of time t_c ,then stepped again and held at a potential E_d for a specific period of time t_d, sufficiently long enough to allow nucleation at specific

sites of the working electrode. During the hold time, t_c and t_d, the current flowing to the interface was acquired over time equal to t_{acq}. After the data acquisition, the process was repeated on a new working electrode (pristine ITO) starting from the base potential, E_b,. Typical current transients are shown in the inset of Figure 2.2.

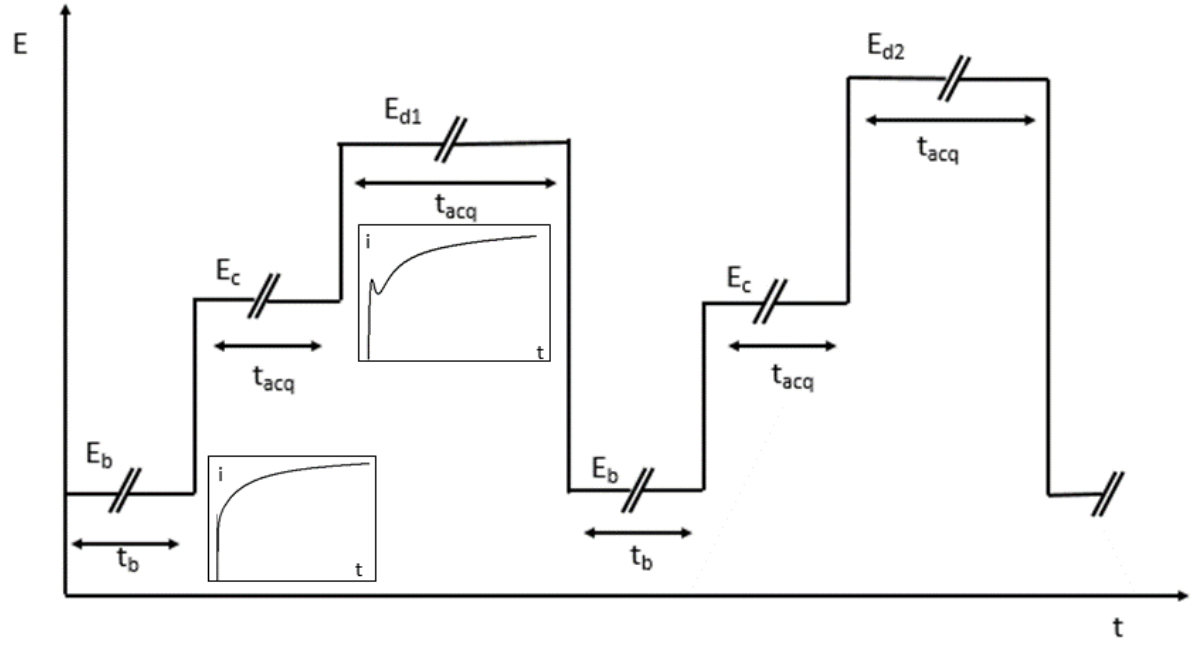

Figure 2.2. A schematic diagram outlining the step sequences of double potential step chronoamperometry measurement. Inset shows typical current transients obtained at E_c and E_d in a chronoamperometry experiment.

The above set-method was used to nucleate and study the growth of the existing gold islands. Whereas, for the nucleation study detailed in Chapter 7, single-step chronoamperometric measurements (as shown in Figure 2.3) were conducted rather than a double step measurement. Here, the electrode potential was initially set to hold at a base potential value (E_b) for time (t_b), where potentially no changes were recorded and then stepped to another potential E_d for a specific period of time t_d, to allow nucleation at specific sites of the working electrode. Once the current transient for the nucleation step is acquired, the process is repeated either on a pristine ITO or on the same ITO by stripping off the gold deposits from previous nucleation study.

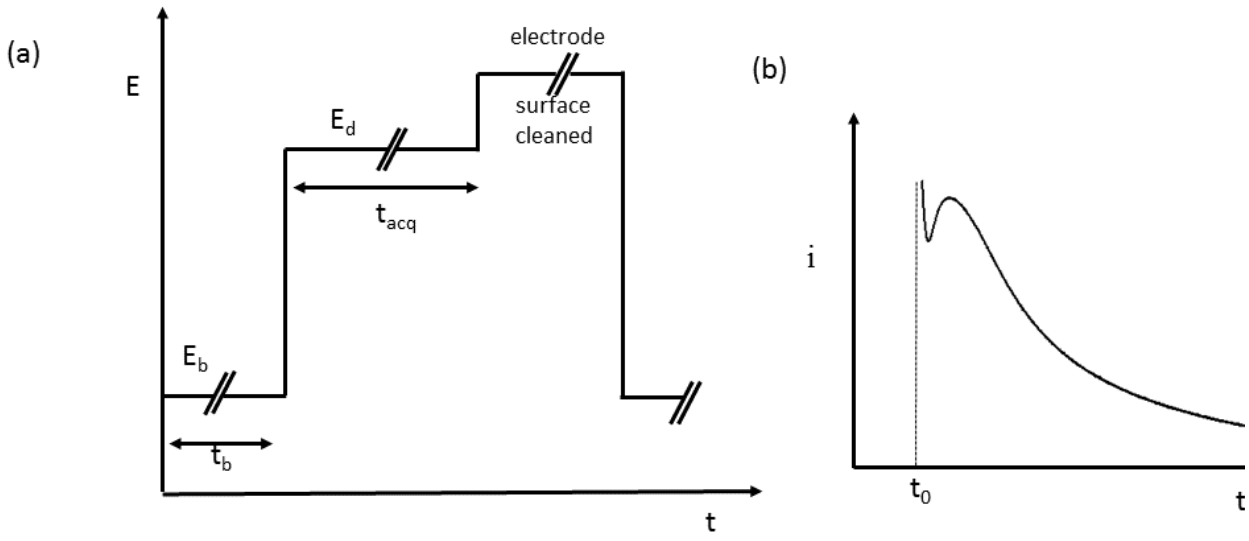

Figure 2.3. Panel (a) A schematic diagram outlining the single potential step chronoamperometry measurement. Panel (b) Typical current transient for nucleation obtained at E_d in a chronoamperometry experiment.

2.4 Scanning Electron Microscopy (SEM)

Scanning electron micrographs were obtained by placing metal nanostructure deposited ITO substrates on mounts with double-stick copper tapes. Samples were examined using a Hitachi SU8010 electron microscope operated at 3 kV and 10 μA and the SEM images were obtained at several different magnifications.

2.5 UV-Vis-NIR analysis of nanostructures

Nanoparticles have unique optical properties that are sensitive to size, shape, concentration, agglomeration state and refractive index near the nanoparticle surface that makes the UV-Vis-NIR a valuable tool in identifying, characterizing, and studying nanostructures. Gold nanoparticles of diameters larger than *ca.* 2-100 nm interact strongly with visible light. At a specific wavelength (frequency) of light, a collective oscillation of electrons on the gold nanoparticle surface causes a phenomenon known as surface plasmon resonance (SPR), resulting in strong extinction of light (absorption and scattering). The frequency of this oscillation depends on the electron density and the size and shape of the electronic charge distribution on the nanoparticle surface. So, the dielectric properties of the environment (solvent, ligands) are essential in determining the SPR

frequency. The wavelength (frequency) that corresponds to the surface plasmon resonance (SPR) can be measured using UV-Vis-NIR spectroscopy. UV-Vis-NIR spectra were obtained using Varian Cary 6000i spectrophotometer from Agilent technologies, and a quartz cuvette of 1 cm path length was used. Cuvettes were cleaned using soap water, then washed with distilled water, finally rinsed with Milli-Q water and allowed to dry at room temperature.

2.6 XRD analysis

The surface structure and the orientation of the electrodeposited nanostructures were determined using X-ray diffraction, which provides the stereographic projection of the lattice planes reflecting X-rays normal to the irradiated electrodeposited crystal surface. In this method, a beam of white X-rays is incident on a stationary surface of interest, and the image of the back-reflected X-rays are collected on a photographic plate. These white X-rays are produced with a copper target at an accelerating voltage of 40 kV. The maximum energy of a photon produced by an electron of charge (e) accelerated through a voltage (V) is given by,

$$h\upsilon_{max} = \frac{hc}{\lambda_{min}} = eV \qquad 2.1$$

where h is the Plank's constant, c is the speed of light and υ_{max} is the highest frequency X-ray produced that corresponds to the shortest wavelength λ_{min}. Each crystallographic structure has its image in reciprocal space. The projection of this image on film and the real space lattice parameters are related through Bragg's law, which gives the relation between the X-ray wavelength, λ and the interplanar distance d:

$$n\lambda = 2\mathrm{dSin}\theta \qquad 2.2$$

where n is the order of interference.

2.7 Pb-UPD analysis of nanostructures

Pb-UPD analysis is a surface-sensitive technique that provides more sensitivity to atoms near the surface than in bulk and therefore most of the signal originates from the point of interest on the metal surface. The structure of the electrode surface was modified by depositing a second metal

(lead) on it by a potentiostatic procedure. Bulk metal deposition is preceded by the gradual build-up of a monolayer at potentials more positive than the reversible Nernst potential of the bulk deposition, in what is called the underpotential deposition (UPD). In UPD, the adsorbate-substrate interactions are stronger than the adsorbate-adsorbate ions.[2] There is a strong dependence of the adsorption behaviour of lead on the crystallographic orientation[3-5] of the gold substrates following an ideal monolayer model. The electrodeposited gold nanostructures on the working electrode were analyzed using the Lead underpotential deposition (Pb UPD) technique. This technique allowed assessment of the crystallographic facets of the electrodeposited structures.

The deposition and the stripping (dissolution) of upd lead on the gold surface was carried out by cyclic voltammetry in a glass electrochemical cell. The electrochemical set-up consisted of a HEKA PG590 potentiostat and the three-electrode train cell described above. The polycrystalline gold bead was formed by the melting and cooling of gold wire. Before its introduction to the electrochemical cell, the gold bead was cleaned through flame annealing, cooled in Milli-Q water and protected with a drop of water. The counter electrode was also a gold wire, flame annealed and cooled before immersion into the cell. The electrodeposited gold nanostructures on the ITO coated glass were the working electrodes to be compared to the polycrystalline gold bead, and they were placed on the three ground joints of the train cell. All potentials were measured with respect to a silver/silver chloride reference electrode connected to the train cell by a salt bridge. The stripping electrolyte was 0.1 M KOH and 1.0 mM $Pb(NO_3)_2$. Since the deposition of lead and its removal on different facets of the gold surface is irreversible, the evidence of strong signals indicated the presence of high energy crystallographic facets. The behaviour of Pb upd on gold electrodeposited structures was similar to that on the polycrystalline gold bead. By comparison of the characteristic peaks to the gold bead, the dominance of the preferential Au {111} facets was discovered.[6]

2.8 FT-Raman analysis of nanostructures

Raman experiments were carried out on a Bruker Equinox 55 spectrometer with an integrated FRA 106/S module. The spectrometer is equipped with a liquid nitrogen-cooled germanium diode detector and an Nd: YAG laser (1064 nm) as an excitation source. Unlike dispersive Raman spectroscopy, where spectra are typically measured using an excitation wavelength in the visible

region [7], the FT-Raman spectrometer uses a 1064 nm laser that virtually eliminates fluorescence.[8]

The samples analyzed were metal nanostructure deposited ITO substrates. The interaction of metal nanoparticles with light generates localized surface plasmon resonances (LSPR) that produce an intense electric field enhancement at the metal surface and gives rise to a dominant surface-enhanced Raman spectroscopy (SERS) mechanism. A maximum SERS signal enhancement is achieved when the excitation source is nearly resonant with the LSPR of the substrate.[9, 10] The Near-IR excitation, particularly at 1064 nm, generates a weaker Raman signal. This weak signal is because the Raman scattering intensity scales directly with the source intensity but inversely with the fourth power of the wavelength. However, despite their inherently lower Raman signal, samples with NIR plasmonic resonances offer distinct advantages, including the absence of fluorescence background signals, and much higher compatibility with samples otherwise prone to photobleaching.[11]

The as-deposited samples were incubated in 0.1mM 4-amino thiophenol (4-ATP) solutions in 95% ethanol for 12 hours and subsequently rinsed thoroughly with Milli-Q water. The laser power used for sample excitation was 400 mW with a 90^{o} spatial geometry at 4 cm^{-1} resolution. The desired signal to noise ratio (S/N) and a good Raman scattering of the samples was obtained with 512 scans.

2.9 References

1. Elgrishi, N., et al., *A Practical Beginner's Guide to Cyclic Voltammetry*. *Journal of Chemical Education*, 2018. **95**(2): p. 197-206.

2. Zeng, X. and S. Bruckenstein, *Underpotential Deposition and Adsorption of Lead on Gold Polycrystalline Electrodes: I. XPS and TOF-SIMS Investigations in 0.1 M NaCl Electrolytes.* Journal of The Electrochemical Society, 1999. **146**(7): p. 2549-2554.

3. Hernández, J., et al., *Characterization of the Surface Structure of Gold Nanoparticles and Nanorods Using Structure Sensitive Reactions*. The Journal of Physical Chemistry B, 2005. **109**(26): p. 12651-12654.

4. Hernández, J., et al., *In Situ Surface Characterization and Oxygen Reduction Reaction on Shape-Controlled Gold Nanoparticles*. Journal of Nanoscience and Nanotechnology, 2009. **9**(4): p. 2256-2273.

5. Sánchez-Sánchez, C.M., et al., *Scanning electrochemical microscopy for studying electrocatalysis on shape-controlled gold nanoparticles and nanorods*. Vol. 55. 2010. 8252-8257.

6. Simon, S., et al., *Role of Au(I) Intermediates in the Electrochemical Formation of Highly Anisotropic Gold Nanostructures with Near-IR SERS Applications*. The Journal of Physical Chemistry C, 2016. **120**(45): p. 26150-26158.

7. Bumbrah, G.S. and R.M. Sharma, *Raman spectroscopy – Basic principle, instrumentation and selected applications for the characterization of drugs of abuse*. Egyptian Journal of Forensic Sciences, 2016. **6**(3): p. 209-215.

8. Edwards, H.G., *Fourier Transform Raman Instrumentation, in Encyclopedia of Analytical Chemistry*. John Wiley & Sons, Ltd, 2006. p. 1-24.

9. Chase, D.B., *Fourier transform Raman spectroscopy*. Journal of the American Chemical Society, 1986. **108**(24): p. 7485-7488.

10. Guerrini, L. and D. Graham, *Molecularly-mediated assemblies of plasmonic nanoparticles for Surface-Enhanced Raman Spectroscopy applications*. Chemical Society Reviews, 2012. **41**(21): p. 7085-7107.

11. Le Ru, E.C. and P.G. Etchegoin, *Chapter 7 - Metallic colloids and other SERS substrates, in Principles of Surface-Enhanced Raman Spectroscopy*, E.C. Le Ru and P.G. Etchegoin, Editors. 2009, Elsevier: Amsterdam. p. 367-413.

CHAPTER 3

SURVEY OF ELECTROCHEMISTRY OF DIFFERENT METAL-PYRIDINE SYSTEMS

3.1 Introduction and literature review of metal-pyridine complexes

Pyridine and other pyridine-derived derivatives are important nitrogen-containing heterocyclic systems, whose synthesis, properties, and reactivity are of great interest. They have become important ligands in organometallic chemistry due to their wide applications (Figure 3.1) especially in catalysis.[1]

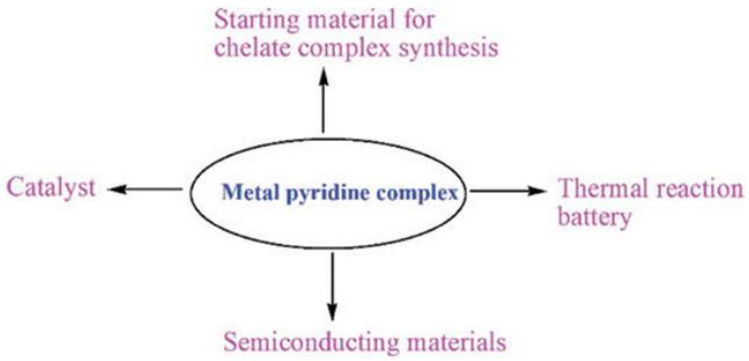

Figure 3.1. Major applications of metal-pyridine complexes. Reprinted from an open access book chapter. Copyright © 2018 Satyanarayan Pal.

Owing to its Lewis base character (Figure 3.2), pyridine is well suited to act as a ligand for transition metals and forms complexes with many different metal centres. Pyridine is a monodentate ligand and is capable of binding to metal centres in different proportions to produce

a range of metal complexes. There is a rich literature of pyridine coordinated complexes of transition metals that has grown over many years [2]

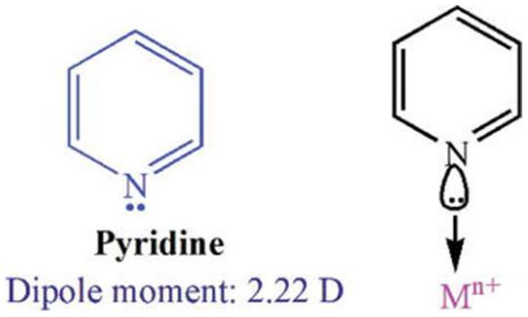

Figure 3.2. Structure of pyridine and its bonding to metal. Reprinted from an open access book chapter. Copyright © 2018 Satyanarayan Pal.

In crystal field theory (CFT), the spectrochemical series of ligands shows the relative d-orbital splitting capability of ligands and depicts pyridine as a moderately strong ligand.[3] Despite being neutral, pyridine causes moderately large d-orbital splitting implying strong bonding interaction to metal centers. Apart from nitrogen lone pair orbitals, the ring π-electron system is also capable of bonding interactions with metal ions. The delocalized π* anti-bonding orbitals can also act as acceptors of metal electron density.

Thus, pyridine provides multiple orbitals for bonding interactions with metal ions. Pyridine is observed to coordinate most of the transition metals producing the variety of metal complexes in their different oxidation states. The research of pyridine derivatives such as 4-methoxypyridine (MOP) has attracted more attention in recent years because of their use as ligands to form stable metal colloids. The discussion here is confined to the domain of pyridine and its coordination to coinage metals such as copper, silver and gold.

3.1.1. Brief history on the existence of different coinage metal pyridine complexes

Coinage metal pyridine complexes have established their importance in various applications in different fields and only the metal-pyridine complexes most pertinent to this thesis are reviewed

in this section. Copper and silver are capable of forming complexes in three oxidation states (I–III), whereas gold only displays two oxidation states (I and III). Copper can have varied number of pyridine ligands in the coordination sphere such as $[Cu(Py)_2(C_2O_4^{2-})]$[3], $[Cu(Py)_3(NCS)_2]$[4], and $[Cu(Py)_4(H_2O)_2]^{2+}$[5]. Complexes with six pyridine ligands, $[Cu(Py)_6]Br_2$ [6] have also been reported. The latter species was prepared by mixing $CuBr_2$ with pyridine in ethanol medium. The compound is stable in dry atmosphere conditions but readily decomposes in the presence of moisture resulting in the compound $[Cu(Py)_2Br_2]2H_2O$. The Ag(I) pyridine complexes observed in the literature are mostly unstable and difficult to isolate. The synthesis of Ag(I)-pyridine complexes involves the reaction of pyridine with Ag(I) salt in a solvent (water is often preferred) or in neat pyridine. Some of the examples from literature include [Ag(Py)(SCN)][7], [Ag(Py)(CN)] [8], and $[Ag(Py)_4]NO_3$ [9]. Ag(II)-pyridine complexes are usually derived from Ag(I) counterpart with the help of suitable oxidizing agents. The square planar geometry of Ag(II)-bis(pyridine-2,3-dicarboxylate) [10], shows an interesting crystal structure where silver(II) is coordinated through pyridine nitrogen and two oxygen atoms of carboxylate groups at the 2-position. Gold has numerous pyridine complexes when compared to silver [11-15]. The gold metal- pyridine chemistry develops with Au (I) and Au (III) states where pyridine and its derivatives were employed to derive desired complexes. For instance, Au(I) pyridine complexes can be made from the reaction of bis(acetonitrile) gold(I) perchlorate and 2-, 3- or 4-cyanopyridine in carbon tetrachloride. The corresponding cyanopyridine was used in the excess amount to produce $[Au(n\text{-}CN\text{-}Py)]ClO_4$ (n = 2, 3, 4) [16]. Au (III) complexes could be prepared from Au (III) starting materials. Some of the most common starting materials used are $AuCl_3$ or $HAuCl_4$.

3.1.2. Optical properties of coinage metal nanoparticles

Traditional coinage metals such as copper, silver and gold have extensive optical properties in their nano dimensions. The optical properties of the coinage metal nanoparticles are inherently dependent both on the particle's size and shape because of strong surface plasmon oscillations within these metals [17] [18]. Non-spherical metal nanoparticles are often termed as anisotropic nanoparticles as described in Chapter 1. Shape anisotropy in metal nanostructures is considered the principal source of the plasmon absorption in the longer wavelengths of the visible region as well as the Near-IR (NIR) region.

In this chapter, an electrochemical survey of different coinage metal ions in the presence of excess MOP is described. By combining electrochemical characterization with SEM measurements, the surface morphology of the electrodeposited nanoparticles is examined to see which metal-MOP complexes give rise to anisotropic structures on ITO substrates.

3.2 Results and Discussions

3.2.1 Survey of coinage metal - 4-methoxypyridine (MOP) electrochemistry

Cyclic voltammetry was used to study coinage metal - MOP electrochemistry on ITO electrodes. The use of planar ITO surfaces provides a reproducible surface and an electrochemical approach allows better control of the reduction potentials.

The measurements were carried out using a customized electrochemical setup (details are provided in Chapter 2). The working electrodes in these experiments were ITO coated glass. A gold coil used as the counter electrode was immersed in aqua regia (3:1 HCl:HNO_3) to remove surface impurities and was flame annealed. The electrolyte solution was deaerated by purging with argon for at least 30 min prior to the experiments, and an argon blanket was maintained over the solution throughout the experiment. Measurements were carried out at room temperature (20 ± 2^0 C).

3.2.1.1 Gold-MOP electrochemistry

The first scan cyclic voltammetry of the Au-MOP complex spontaneously formed in solution by the addition of 0.25 mM $KAuCl_4$ to an aqueous solution of 100 mM NaCl and 100 mM MOP is shown in Figure 3.3.

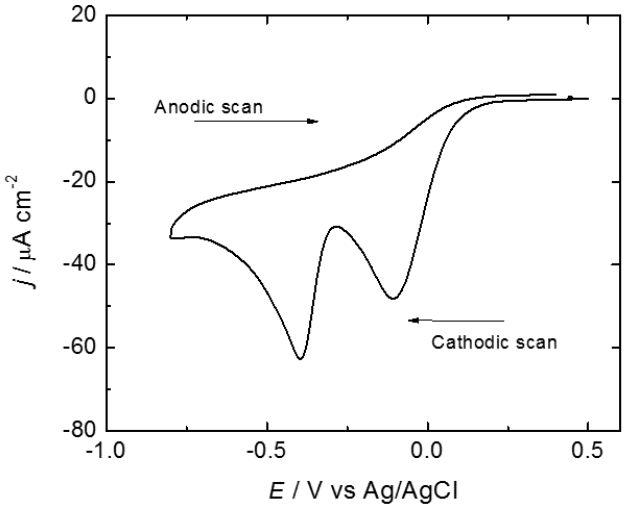

Figure 3.3. Cyclic voltammogram (20 mV/s) of ITO electrode in 0.25 mM $KAuCl_4$ aqueous solution of 0.1 M NaCl and 0.1 M 4-methoxypyridine.

The CV is similar in appearance to the voltammograms reported for Au^{III} complexes involving pyridine ligands in nonaqueous solvents [11-14]. Two irreversible voltammetric peaks were seen while scanning the potential of the ITO working electrode negative from the open circuit potential (~ 0.4V). Peak I appears at ca. -0.10V and has a magnitude roughly two-thirds that of the more intense signal, peak II, observed at ca. -0.4V. The voltammetry implies a two-step reduction process involving the formation of an Au^{I} intermediate species (peak I) and its subsequent reduction to Au^{0} (peak II). It was observed that the reductive electrochemistry is largely identical if the NaCl supporting electrolyte is replaced by NaF or NaBr, as shown in Figure 3.4. However, if the electrolyte and MOP were allowed to react for extended periods, new shoulders were seen in the voltammetry, as shown in Figure 3.5, which is indicative of the likely formation of the different Au^{III} complexes of F^-, Cl^-, and MOP.

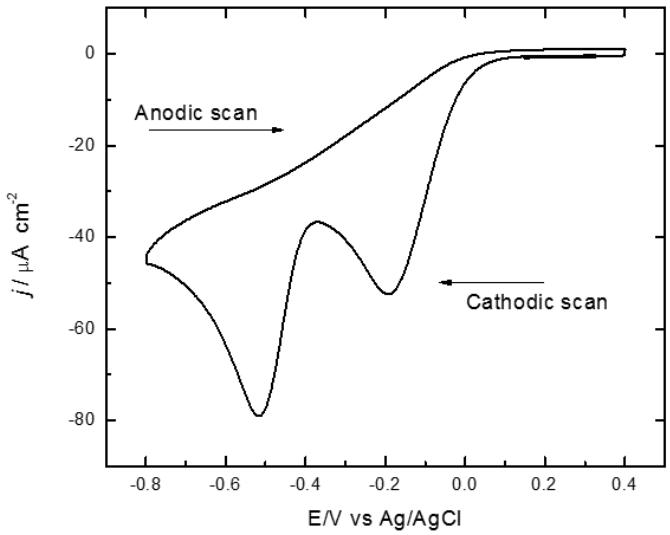

Figure 3.4. Cyclic voltammogram (20 mV/s) of ITO electrode in 0.25 mM $KAuCl_4$ aqueous solution of 0.1 M NaF and 0.1 M 4-methoxypyridine.

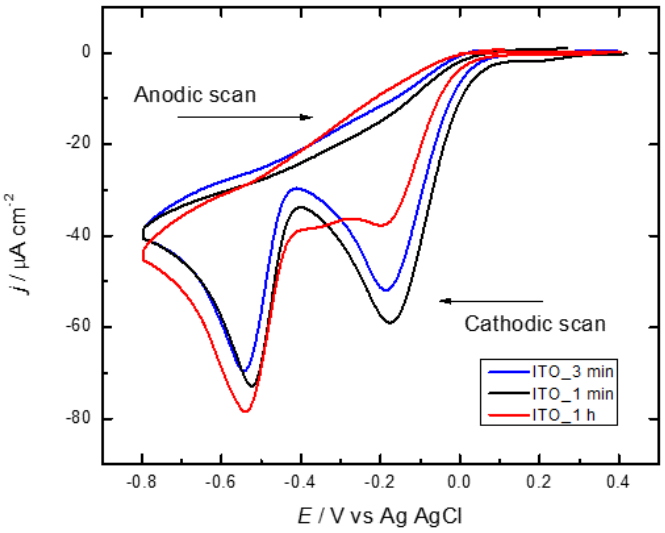

Figure 3.5. Cyclic voltammogram (20 mV/s) of ITO electrodes in 0.25 mM $KAuCl_4$ aqueous solution of 0.1 M NaF and 0.1 M 4-methoxypyridine for different ageing times of Au-*Py* solution.

3.2.1.2 Silver- MOP electrochemistry

To test the influence of MOP on the Ag^{I} complex, a cyclic voltammogram similar to the Au-MOP system was run. The first scan cyclic voltammetry of the Ag-MOP complex spontaneously formed in solution by the addition of 0.25mM $AgNO_3$ to an aqueous solution of 100mM KNO_3 and 100mM MOP is shown in Figure 3.6a.

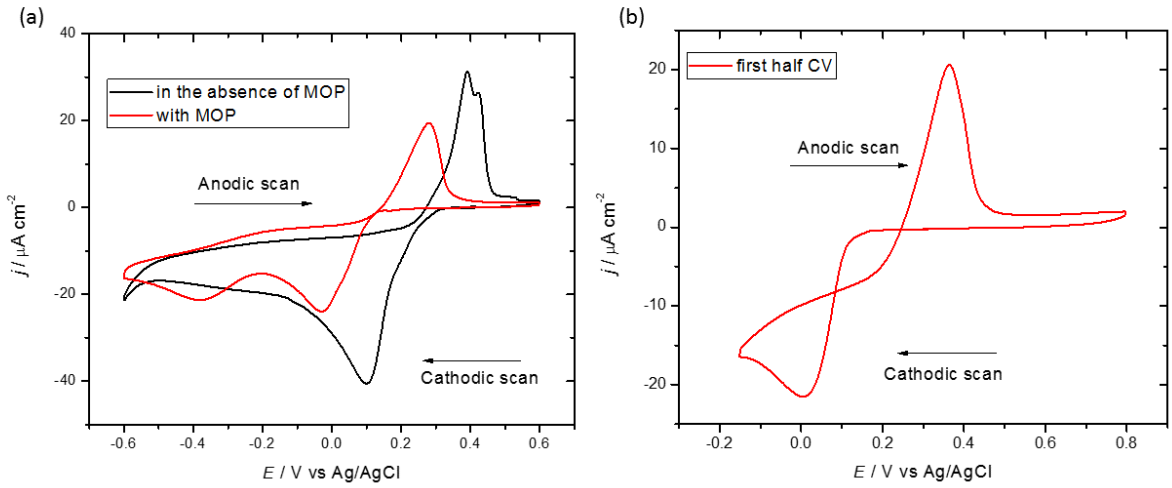

Figure 3.6. Cyclic voltammogram (20 mV/s) of ITO electrode in (a) 0.25 mM $AgNO_3$ aqueous solution of 0.1 M KNO_3 in the presence and absence of 0.1 M 4-methoxypyridine (b) the cathodic and anodic scan of the first half CV in the presence of 0.1 M 4-methoxypyridine.

Even though the situation is markedly different as the experiment started with Ag(I) oxidation state, the voltammogram was very similar to the Au(III) electrochemistry. The cyclic voltammogram indicated the presence of more than one complex species in solution in the cathodic scan followed by an interesting anodic response. Two irreversible voltammetric peaks are seen while scanning the potential of the ITO working electrode negative from the open circuit potential (~0.4V). Peak I was observed at ca. -0.05V and has a magnitude roughly the same as that of the second signal, peak II, observed at ca. -0.40V. Peak I represents the reduction of Ag^{I} complex to Ag^{0} as it could be stripped off with an anodic sweep to the high positive potentials as shown in Figure 3.6b. The presence of the second peak (peak II) is suspected to be caused by the presence of a different Ag complex with MOP. Different studies of the interaction of silver (I) ions with

pyridine ligands in solutions have been reported.[19-25] Among these, the possibility of different complex compositions obtainable in solution (Ag: Pyridine) have been considered.

3.2.1.3 Copper -MOP electrochemistry

The cyclic voltammetric response of the Cu-MOP system was also investigated within the same potential windows, as that of the other coinage metal systems, i.e. 0.4V to -0.8V at 20 mV/s. The first scan cyclic voltammetry of the Cu-MOP complex spontaneously formed in solution by the addition of 0.25mM $CuSO_4$ to an aqueous solution of 100 mM K_2SO_4 and 100mM MOP is shown by the black trace in Figure 3.7.

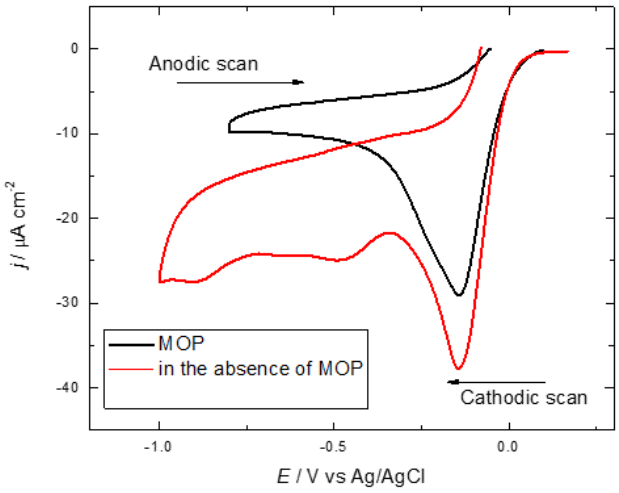

Figure 3.7. Cyclic voltammograms (20 mV/s) of ITO electrodes in 0.25 mM $CuSO_4$ aqueous solution of 0.1 M K_2SO_4 in the presence and absence of 0.1 M 4-methoxypyridine.

Scanning the potential of the ITO working electrode negative from the open circuit potential (0.4V), showed only one irreversible reduction peak at ca. -0.14V. In the presence of MOP (the black CV), the copper complex does not seem to stable in comparison to the absence of MOP. The CV implies that MOP is not complexing with the Cu^{2+} ion to form a stable complex. The CV feature differs from voltammograms reported for Cu^{II} complexes involving pyridine ligands in nonaqueous solvents[26]. As the copper-MOP complex formed showed no difference in the reduction potential in the presence and absence of the ligand (see the red trace in Figure 3.7), it seemed less interesting to pursue further for this research work.

3.2.2 Electrodeposition of metal nanoparticles on indium tin oxide (ITO)

Electrodeposition experiments were performed to investigate if MOP directs anisotropic growth of metal nanoparticles electrodeposited on the ITO electrode. The potentiostatic electrodeposition of the nanostructures was achieved by biasing a pristine ITO sample at the respective peak potentials until an integrated current provided 75 mC cm^{-2} of charge. The electrodeposited nanostructures on the ITO surface were further characterized using scanning electron microscopy.

3.2.2.1 Silver nanoparticles

The electrodeposition of silver nanostructures was achieved by biasing the ITO electrode at - 0.12 V. As shown in the Figure 3.8 b, the surface was seen to be populated with quasi-spherical nanostructures.

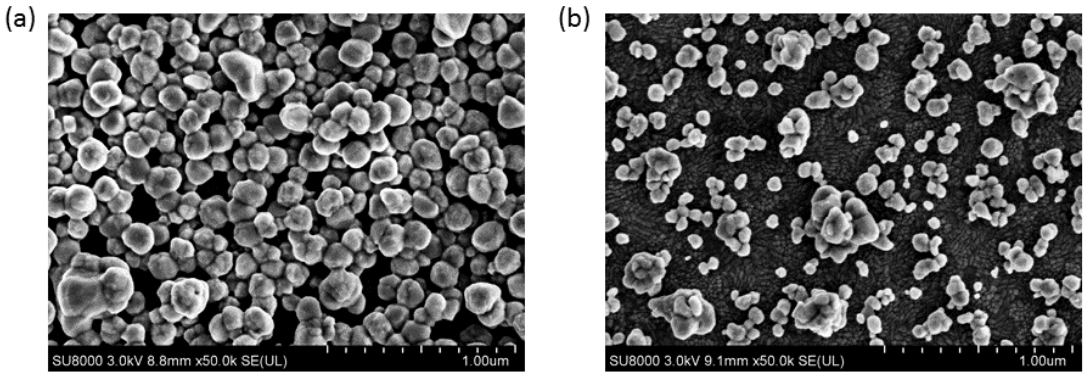

Figure 3.8. SEM images of ITO electrode after depositing silver from 0.25 mM $AgNO_3$ and 0.1 M MOP in 0.1 M KNO_3 (a) Deposition potential was -0.43 V (b) Deposition potential was -0.12 V.

Although these nanostructures were slightly faceted, no signs of significant anisotropy were observed in the presence of MOP. Electrodeposition by biasing the ITO electrode on the second potential at -0.43V observed similar nanostructures as that of the initial peak potential deposition (Figure 3.8a). The significant difference observed for the electrodeposition of silver nanostructures at the above two potentials was their population density. The silver nanostructures deposited at

more negative deposition potential were observed to be more densely packed on the ITO working electrode compared to those formed at the more positive deposition potential.

3.2.2.2 Gold nanoparticles

The electrodeposition of gold nanostructures was achieved by biasing the ITO electrode at the second peak potential at -0.43 V. The surface was seen to be decorated with a dense layer of anisotropic crystallites, as shown in Figure 3.9a, and a higher magnified image of the same surface (Figure 3.9b) showed the multipodal nature of the electrodeposited features.

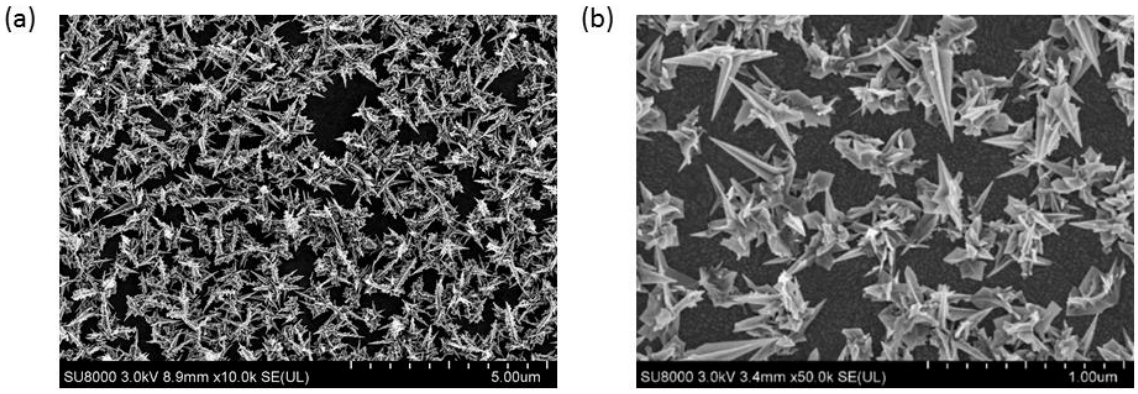

Figure 3.9. SEM images of ITO electrode after depositing gold from 0.25 mM $KAuCl_4$ and 0.1 M MOP in 0.1 M NaCl (a) Deposition potential was -0.43 V (b) magnified image of (a).

These nanostructures deposited in the presence of MOP exhibited high aspect ratio branches with the arms extending several hundred nanometers. The nanostructures are referred to as nanodaggers as their branches were distinctively tapered with a dagger-like appearance. Previous studies have shown that pyridine molecules adsorbed on specific crystal facets can act as shape directing agents[27]. The shape directing role of 4-methoxypyridine was further confirmed by electrodepositing 0.25 mM $KAuCl_4$ and 100 mM NaCl in the absence of the pyridine derivative, as shown in the Figure 3.10.

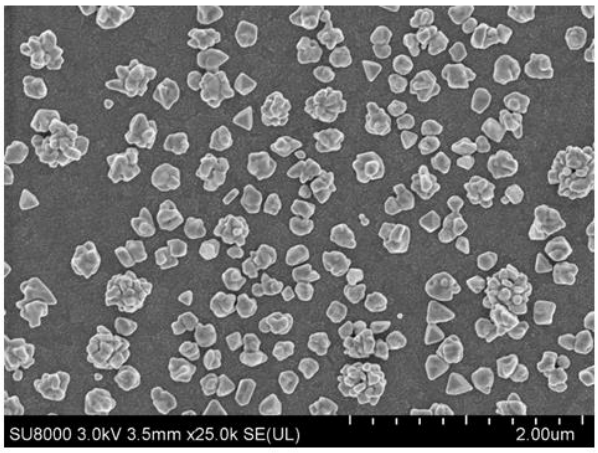

Figure 3.10. SEM images of ITO electrode after depositing gold from 0.25 mM $KAuCl_4$ in 0.1 M NaCl in the absence of MOP. Deposition potential was -0.43 V.

It is quite evident from the SEM image that the electrodeposition from a pyridine free solution generated quasi-spherical nanoparticles with some visible faceting. However, the formation of nanodaggers is not observed in the absence of a pyridine derivative. The presence of highly anisotropic nanostructures in the presence of MOP was intriguing, and further studies were performed on nanoparticle dispersions to re-confirm the presence of anisotropy in these nanostructures.

3.2.3 4- Methoxypyridine stabilized nanoparticle dispersions

Metal nanoparticles stabilized with 4-methoxypyridine were prepared by following the method described by Danger *et al.* [28]. All solutions were prepared using Millipore (18.2 MΩ cm) water. Aqueous solutions of 100 mM MOP and 10 mM $NaBH_4$ were prepared. The latter solution was kept in an ice bath at all times and freshly made after no more than 2 hours. Metal nanoparticles synthesized by the borohydride reduction of corresponding metal salts showed characteristic differences among the coinage metals, gold and silver. Nanoparticle formation was further confirmed by UV-Vis-NIR spectroscopy and transmission electron microscopy.

3.2.3.1 Gold nanoparticle dispersion

Nanoparticle synthesis was achieved by adding 100 μL of 100 mM $KAuCl_4$ to 4 mL of MOP solution in a three-dram vial. An orange color was noted immediately after addition, which quickly (less than 1-2 s) turned bright yellow. If borohydride was not added, this solution slowly turned faint yellow over time (10-20 min). The addition of 100 μL of cold $NaBH_4$ led either to immediate coloring of the solution or the presence of a near-transparent solution that slowly developed into a pronounced color depending on the value of τ which is the reaction time between the gold salt and the MOP. The color of the solutions (as shown in Figure 3.11) formed from the borohydride reduction of the gold salt in the presence of MOP was found to be highly dependent on the time lapse between the preparation of the $AuCl_4$-MOP mixture and the addition of the reducing agent.

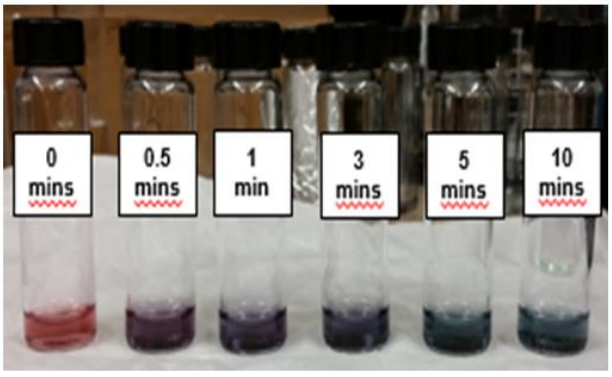

Figure 3.11. Varying optical appearances of the gold dispersions obtained by the addition of 100 μL of cold 10 mM $NaBH_4$ to 100 μL of 100 mM $KAuCl_4$ and 4 mL of 100 mM MOP at various τ values .

Minimal values of τ (less than 5 s) led to ruby red colors, intermediate values of τ provided green to purple colored solutions, and longer values of τ (~10 min) provided blue colored solutions. The solutions were stable on the bench for hours to days, depending on the final color with the smaller values of τ showing higher resistance to flocculation. In contrast, sedimentation of the colloidal dispersions was more pronounced in the blue colored solutions. The varying optical appearances of the gold dispersions were indicative of the formation of different sizes and shapes of nanocrystals. Further information pertaining to the shape and size of the nanocrystals can be

extracted from the optical and near-infrared (NIR) extinction spectra, as described in the optical characteristics section of this chapter.

3.2.3.2 Silver nanoparticle dispersion

The synthesis of silver nanoparticles followed the same procedure as that used for gold nanoparticles. The synthesis was achieved by adding 100 µL of 100 mM $AgNO_3$ to 4 mL of MOP solution in a three-dram vial. A white color was noted immediately after mixing of the above solutions, which quickly disappeared. The addition of 100 µL of cold $NaBH_4$ led to a yellow colored solution. The lapse time, τ, between the preparation of the $AgNO_3$-MOP mixture and the addition of the reducing agent seemed to have no effect in determining the color of the solutions (Figure 3.12).

Figure 3.12. Silver dispersions obtained by the addition of 100 µL of cold 10 mM $NaBH_4$ to 100 µL of 100 mM $AgNO_3$ and 4 mL of 100 mM MOP at various τ values (left to right - 0 min,1 min,3 min,5 min and 10 min).

All values of τ resulted in yellow colored solutions. The solutions were stable on the bench for days, and the optical appearances of the silver dispersions were indicative of the formation of nanospheres. Nanoparticle solutions were left to age for approximately 1 hour before their characterizations were carried out.

3.2.4 Characterization of nanoparticle dispersions

The nanoparticle formed in the solutions were characterized by transmission electron microscopy (TEM).

3.2.4.1 TEM results

Transmission electron micrographs were obtained with a Hitachi 410 microscope operating at 100 kV. Concentrations of the nanoparticle solutions were the same as those used for UV-Vis analysis described later in this section. Thirty minutes after the addition of borohydride, the nanoparticle solution was drop cast on a carbon-coated copper TEM grid and evaporated in the air. The TEM results, as shown in the Figure 3.13, revealed the differences in shapes and sizes of the gold nanostructures from silver nanostructures. The average size and the distribution of the metal nanoparticles were shown clearly from the TEM images.

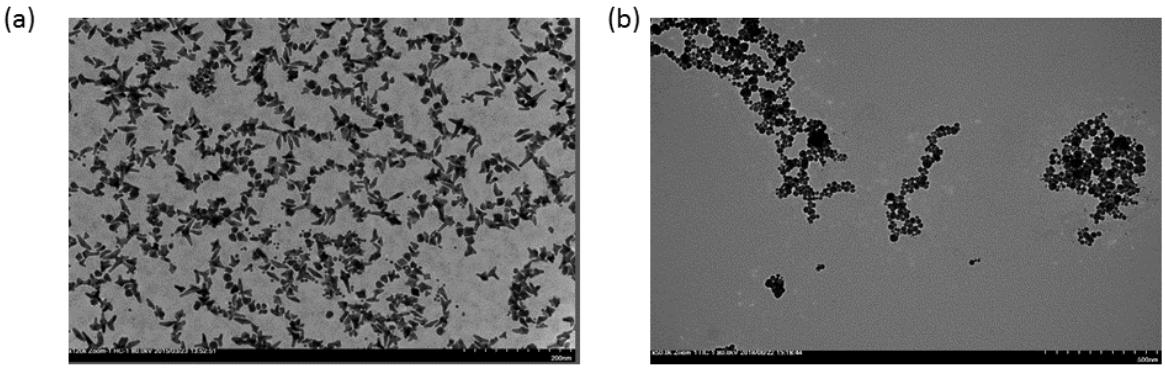

Figure 3.13. TEM images (a) transmission electron micrograph of gold nanocrystals formed from the $NaBH_4$ reduction of $KAuCl_4$ in the presence of MOP at τ = 10 min (b) transmission electron micrograph of silver nanocrystals formed from the $NaBH_4$ reduction of $AgNO_3$ in the presence of MOP at τ = 10 min.

The silver nanostructures synthesized by the reduction of silver nitrate using borohydride in the presence of 4-methoxypyridine were observed as aggregates of nanospheres with a diameter size of less than 50nm. However, the gold nanostructures, synthesized likewise by the reduction of gold Au^{3+} species in the presence of MOP were smaller and clearly showed anisotropy in their shapes.

These uniqueness of the Au-MOP system for forming anisotropic structures by chemical reduction is quite consistent with the appearance of the nanostructures formed by electrodeposition.

3.2.5 Optical characterizations

3.2.5.1 UV-Vis-NIR analysis

The optical properties of the particles made by the chemical reduction of MOP-metal complexes was investigated using UV-Vis-NIR spectroscopy. The resulting MOP stabilized gold and silver nanoparticles were monitored by an optical-NIR spectra recording the absorbance spectrum in the 300-1800 nm region using standard quartz cuvettes and a Cary 6000i (UV-Vis- NIR) spectrometer. The as-synthesized MOP stabilized metal nanoparticles were further diluted to adjust the absorbance to approximately unity. All glassware used for the synthesis and UV-Vis analysis of the nanoparticles were treated with *aqua regia* (3 parts HCl, 1-part HNO_3), rinsed in Millipore water, and oven-dried before use.

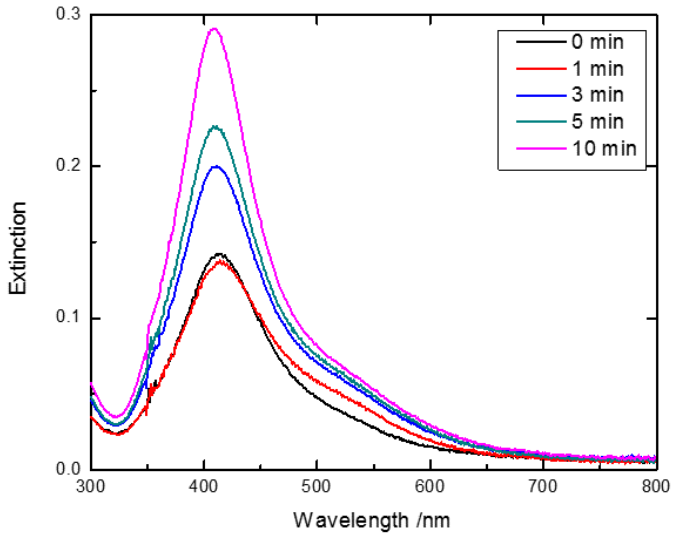

Figure 3.14. UV-Vis-NIR extinction spectra of silver nanoparticles at different τ times with MOP.

Figure 3.14 presents the absorption spectra of diluted MOP-silver nanoparticles after the borohydride reduction. The delay time of the borohydride addition to the solution containing MOP and silver nitrate did not affect the position of the localized surface plasmon polariton resonance, as all the colloidal solutions turned equally yellow in color (Figure 3.12). The extinction spectra

for all Ag nanoparticle dispersions display a single, distinctive peak at 410nm that corresponds to the dipolar resonances of the nanospheres [29, 30]. The broadening of the peak may be due to the aggregation of the nanoparticles in solution. This is consistent with some degree of nanoparticle aggregation as shown by the TEM images in Figure 3.13b.

The UV-Vis-NIR spectral analysis shown in Figure 3.15 demonstrates that the delay time, τ, of borohydride addition and the pyridine ligand, MOP both play an essential role in the stability of MOP-Au nanoparticles.

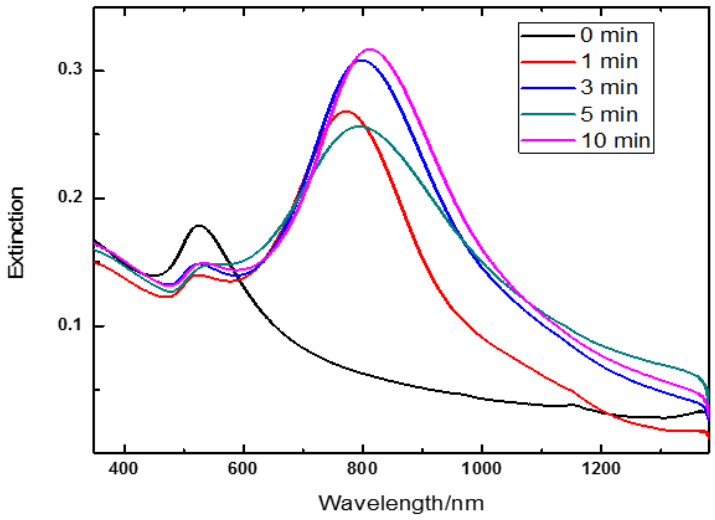

Figure 3.15. UV-Vis-NIR extinction spectra of gold nanoparticles at different τ times with MOP.

A common peak was observed at ~525 nm, which is attributed to the surface dipole commonly observed for spherical gold nanoparticles and the transverse, dipolar modes of nanorods [31]. The position and intensity of this band varied only slightly with τ indicating subtle changes in the size and number density of the dimension that gives rise to this localized surface plasmon resonance [31]. A second extinction maximum was observed that developed with increasing values of τ. The absorbance spectra revealed that the higher wavelength peak slightly redshifts extending into the NIR region for the longer τ solutions. The observation of a second plasmon mode was highly

indicative of the presence of anisotropic nanoparticles [32, 33], as observed from the corresponding TEM image (Figure 3.13a).

3.3 Conclusions

The electrochemical behaviour of coinage metals and their adsorption with MOP was studied in this chapter. A brief survey on the electrochemistry of coinage metals such as copper, silver and gold was explored using cyclic voltammetric studies. It has been demonstrated from the Au-MOP cyclic voltammograms that the system itself is quite unique in its ability to lead anisotropic nanoparticles. It was revealed that there occurred two reduction processes in the Au-MOP electrochemistry, and the metallic gold was formed on the most negative reduction potential. The electrochemical results leads to new questions as of why two peaks appears in the cathodic scan, what are the species present in the solution and so forth. Subsequent chapters in this thesis attempt to provide answers to the above questions posed by the AuMOP system. In contrast to gold, the presence of MOP did not create a considerable change in the reduction potentials of Cu (II) and hence was not an interesting subject of study. The silver electrochemistry, on the other hand, had a similar voltammogram as that of the gold but in the presence of MOP, silver nanostructures failed to reveal anisotropy and were again excluded from the subject of study.

Further research was performed on the colloidal nanoparticle solution. MOP stabilized metal nanoparticles were studied using UV-Vis spectroscopy and transmission electron microscopy. It has been observed that the higher wavelength peak redshifts with longer reaction time between the gold salt and MOP, before the reducing agent, was introduced. The varying optical appearances were more prominent on the gold dispersions than the silver ones. These results can be used to offer insight into the role MOP plays in stabilizing colloidal gold. Additionally, the work demonstrates how the electrolytes have no role in determining the shapes and sizes of the gold nanostructures. The electrochemistry was mostly identical for both NaCl and NaF electrolytes. The shape directing pyridine ligand, MOP, achieved anisotropic gold nanostructures with high aspect ratios, and these were named nanodaggers. The property of anisotropy demonstrated by the gold nanoparticles and the complex chemistry behind the reaction was further investigated in the following chapters of this thesis.

3.4 References

1. Zafar, M.N., et al., *Pyridine and related ligands in transition metal homogeneous catalysis.* Russian Journal of Coordination Chemistry, 2016. **42**(1): p. 1-18.

2. Pal, S. *Pyridine: A Useful Ligand in Transition Metal Complexes*. 2018.

3. C, L., Journal de Pharmacie de Belgique., 1948. **17**(3).

4. Calzolari, J., *Doppelrhodanide des zweiwertigen Kupfers und des Kobalts mit organischen Basen.* Berichte der deutschen chemischen Gesellschaft, 1910. **43**(2): p. 2217-2230.

5. Leussing, D. and P. Gallagher, *The heats and entropies of formation of the Copper(II)-Pyridine complexes.* The Journal of Physical Chemistry, 1960. **64**(11): p. 1631-1633.

6. Allan, J.R., et al., *Pyridine complexes of iron(II), copper(II), zinc(II), and cadmium(II) halides.* Journal of the Chemical Society A: Inorganic, Physical, Theoretical, 1966(0): p. 1031-1034.

7. Mathews, J.H., E.L. Krause, and V.L. Bohnson, *A contribution to the thermal chemistry of Pyridine.* Journal of the American Chemical Society, 1917. **39**(3): p. 398-413.

8. R., V., Comptes Rendus de l'Académie des Sciences., 1891. **112**: p. 390.

9. Wilke-Dörfurt, E. and G. Balz, *Zur Kenntnis der Borfluorwasserstoffsäure und ihrer Salze.* Zeitschrift für anorganische und allgemeine Chemie, 1927. **159**(1): p. 197-225.

10. Drew, M., R. Matthews, and R. Walton, *The crystal structure of silver (II)-bis (pyridine-2, 3-dicarboxylate) dihydrate.* Inorganic and Nuclear Chemistry Letters, 1970. **6**(3): p. 277-280.

11. Corbo, R., et al., *Facile Formation of Homoleptic Au(III) Trications via Simultaneous Oxidation and Ligand Delivery from [PhI(pyridine)2]2+*. Journal of the American Chemical Society, 2014. **136**(35): p. 12415-12421.

12. Gabbiani, C., et al., *Structural Characterization, Solution Studies, and DFT Calculations on a Series of Binuclear Gold(III) Oxo Complexes: Relationships to Biological Properties.* Inorg. Chem., 2008. **47**(7): p. 2368-2379.

13. Li, J., et al., *Catalytic activities and properties of Au(III)/Schiff-base complexes in methanol oxidative carbonylation.* Journal of Molecular Catalysis A: Chemical, 2011. **340**: p. 53-59.

14. Serratrice, M., et al., *Synthesis, Structural Characterization, Solution Behavior, and in Vitro Antiproliferative Properties of a Series of Gold Complexes with 2-(2'-Pyridyl)benzimidazole as Ligand: Comparisons of Gold(III) versus Gold(I) and Mononuclear versus Binuclear Derivatives.* Inorganic Chemistry, 2012. **51**(5): p. 3161-3171.

15. Fernández, E.J., et al., *Pyridine gold complexes. an emerging class of luminescent materials.* Gold Bulletin, 2007. **40**(3): p. 172-183.

16. Farha Jr, F. and R.T. Iwamoto, *The preparation and infrared examination of the 2-, 3-, and 4-cyanopyridine complexes of copper (I), silver (I), and gold (I) perchlorates.* Inorganic Chemistry, 1965. **4**(6): p. 844-848.

17. Link, S. and M.A. El-Sayed, *Size and Temperature Dependence of the Plasmon Absorption of Colloidal Gold Nanoparticles.* J. Phys. Chem. B, 1999. **103**(21): p. 4212-4217.

18. Creighton, J.A. and D.G. Eadon, *Ultraviolet-visible absorption spectra of the colloidal metallic elements.* J. Chem. Soc., Faraday Trans., 1991. **87**(24): p. 3881-91.

19. Akhavein, A. and J.E. House, *Thermal studies on solid complexes of silver nitrate with substituted pyridines.* Journal of Inorganic and Nuclear Chemistry, 1970. **32**(5): p. 1479-1484.

20. Bruehlman, R.J. and F.H. Verhoek, *The basic strengths of amines as measured by the stabilities of their complexes with silver ions.* J. Am. Chem. Soc., 1948. **70**: p. 1401-4.

21. Molina, M. and S. Tabak, *Interaction of ion silver(I) with pyridines.* Journal of Inorganic and Nuclear Chemistry, 1972. **34**(9): p. 2985-2987.

22. Murmann, R.K. and F. Basolo, *The stability of silver(I) complexes of some 3- and 4-substituted pyridines.* J. Am. Chem. Soc., 1955. **77**: p. 3484-6.

23. Peard, W.J. and R.T. Pflaum, *Interaction of metal ions with heterocyclic amines. Silver(I) complexes.* J. Am. Chem. Soc., 1958. **80**: p. 1593-6.

24. Popa, G., C. Luca, and V. Magearu, *Effect of solvent on the stability of complex compounds. II. Complexes of silver with pyridine and its derivatives in acetone-water and dioxane-water solutions.* J. Chim. Phys. Phys.-Chim. Biol., 1965. **62**(4): p. 449-53.

25. Popa, G., V. Magearu, and C. Luca, *The effect of the solvent on the stability of complex compounds. III. Silver complexes of pyridine derivatives in ethanol-water solutions.* J. Chim. Phys. Phys.-Chim. Biol., 1965. **62**(7-8): p. 853-5.

26. Ourari, A., W. Derafa, and D. Aggoun, *A novel copper(ii) complex with an unsymmetrical tridentate-Schiff base: synthesis, crystal structure, electrochemical, morphological and electrocatalytic behaviors toward electroreduction of alkyl and aryl halides.* RSC Advances, 2015. **5**(101): p. 82894-82905.

27. Vivek, J.P. and I.J. Burgess, *Crystallographic dependence of 4-dimethylaminopyridine electrosorption on gold.* Electrochim. Acta, 2013. **88**: p. 688-696.

28. Danger, B.R., et al., *Electrochemical Studies of Capping Agent Adsorption Provide Insight into the Formation of Anisotropic Gold Nanocrystals.* ACS Nano, 2012. **6**(12): p. 11018-11026.

29. Carlberg, M., et al., *Optical response of heterogeneous layer containing silver nanospheres and nanoprisms.* Materials Today: Proceedings, 2017. **4**: p. S3-S11.

30. Bastus, N.G., J. Piella, and V. Puntes, *Quantifying the Sensitivity of Multipolar (Dipolar, Quadrupolar, and Octapolar) Surface Plasmon Resonances in Silver Nanoparticles: The Effect of Size, Composition, and Surface Coating.* Langmuir, 2016. **32**(1): p. 290-300.

31. Eustis, S. and M.A. el-Sayed, *Why gold nanoparticles are more precious than pretty gold: noble metal surface plasmon resonance and its enhancement of the radiative and nonradiative properties of nanocrystals of different shapes.* Chem Soc Rev, 2006. **35**(3): p. 209-17.

32. Hu, M., et al., *Gold nanostructures: engineering their plasmonic properties for biomedical applications.* Chemical Society Reviews, 2006. **35**(11): p. 1084-1094.

33. Pérez-Juste, J., et al., *Gold nanorods: Synthesis, characterization and applications.* Coordination Chemistry Reviews, 2005. **249**(17): p. 1870-1901.

CHAPTER 4

THE HOMOGENEOUS CHEMISTRY OF 4-METHOXYPYRIDINE (MOP) AND $KAUCL_4$

4.1 Introduction

It is quite essential to construct nanostructures on substrates to develop functional nanodevices. Nanoscale structures support surface plasmon propagation, which is primarily responsible for the underlying physical effect in surface-enhanced Raman scattering (SERS).[1, 2] Though many efforts have been made to understand and control the surface growth of nanoparticles,[3-7] the preparation of nanoparticles on solid substrates with well-defined shape and size is still a challenge. Potential controlled electrodeposition [8] from a homogenous solution is one possible means to generate a uniform layer of nanostructures on substrates. In such instances, a conductive substrate is immersed in a plating bath containing a metal ion and the application of an external electric potential causes the reduction, nucleation, and growth of metal islands on the substrate. In many cases, the nature of the metal ion, and the various additives in the plating bath, play a critical role in determining the shape, texture, and morphology of the deposited metal.

Empirically, in this thesis, it will be shown that the electrodeposition of gold from the solution that results from the mixing of $KAuCl_4$ with 4-methoxypyridine outcomes the formation of a film of highly anisotropic gold nano structures. Considerable effort will be spent in Chapter 5 describing the complex electrochemistry of this system. However, the goal of the current Chapter is to describe the various chemical processes that occur in the aforementioned solution without the application of an external potential (i.e. at the so-called open circuit potential).

The chemistry that arises upon the addition of 4-methoxypyridine (abbreviated hereafter as *Py*) with $KAuCl_4$ is remarkably complex. Mass spectrometry analysis (Figure 4.1) of a mixture of a solution of $KAuCl_4$ and an excess of *Py* at (or near) equilibrium revealed that the primary species in solution were three Au^{III} species ($AuPy_2(OH)_2^+$, $AuPy_2Cl(OH)^+$ and $AuPy_2Cl_2^+$) and a single Au^I species, $AuPy_2^+$. This indicates that the system undergoes ligand-exchange, redox and heterogeneous electron transfer reactions. Explaining the observed speciation requires both a thermodynamic and kinetic analysis.

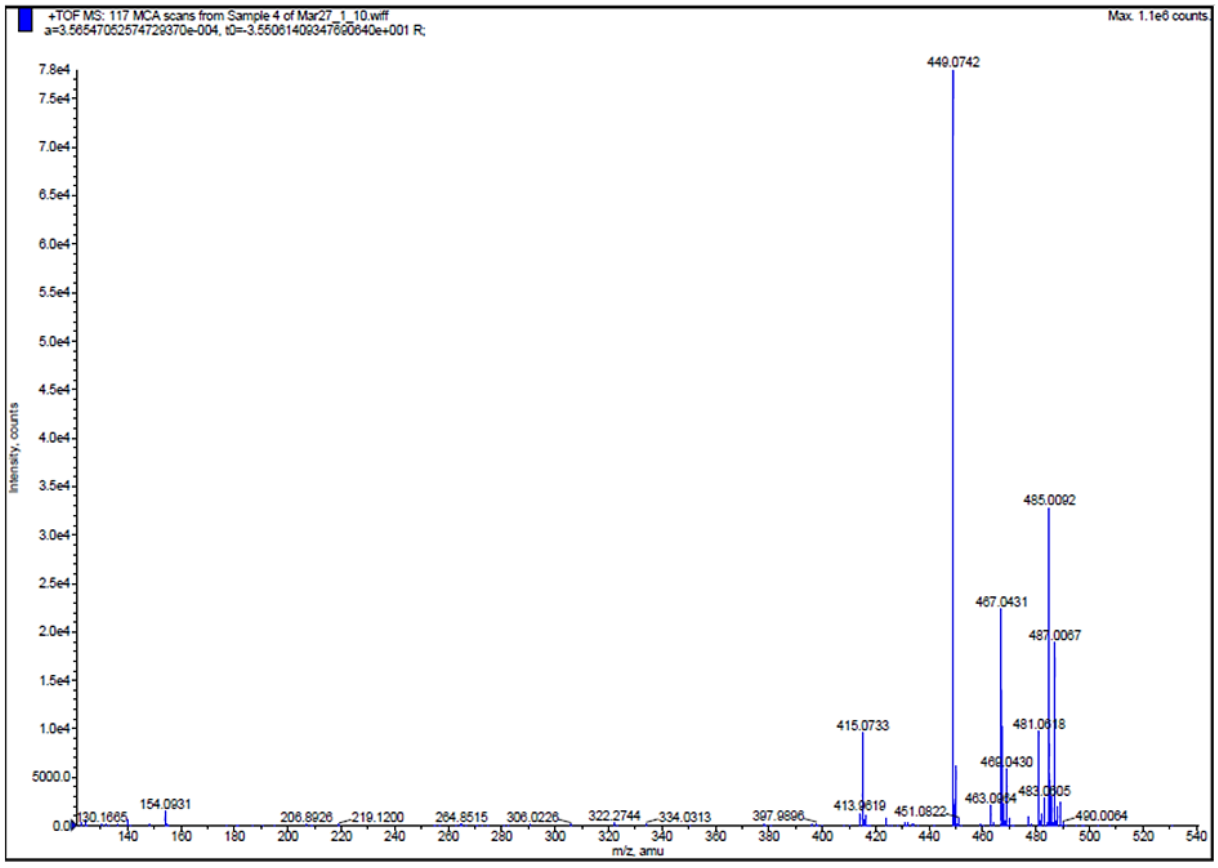

Figure 4.1. Positive-mode ESI (electron spray) mass spectrum recorded on an Au-*Py* sample after 4 hours of reaction time, examined by diluting approximately 50 ul of sample with 1 ml of methanol. Theoretically calculated masses of $AuPy_2^+$; $AuC_{12}H_{14}N_2O_2$ (m/z 415), $AuPy_2(OH)_2^+$; $AuC_{12}H_{16}N_2O_4$ (m/z 449), $AuPy_2Cl(OH)^+$; $AuC_{12}H_{15}N_2O_3Cl$ (m/z 467), $AuPy_2Cl_2^+$; $AuC_{12}H_{14}N_2O_2Cl_2$ (m/z 485) was within the < 2% ppm error.

4.2 Electrochemical measurements

The addition of 0.25mM $KAuCl_4$ to an aqueous solution of 0.1M NaCl and 0.01M MOP showed two irreversible voltammetric peaks on the cathodic scan from the open-circuit potential as seen in Figure 4.2. Voltammetric studies have been extensively studied and discussed in the next chapter and this section is used only to briefly describe the electrochemistry of the AuMOP system. The voltammetry implied a two-step reduction process involving the formation of an Au^I intermediate species (peak I) and its subsequent reduction to Au^0 (peak II). Every individual scan was performed on a pristine ITO electrode over the course of time. In the two-step reduction process, as the solution was aged over time, the magnitude of the peak current for I was observed to decrease, whereas that of peak II was found to increase. The electrochemical results provide additional evidence that a spontaneous redox reaction occurs in the bulk of solution and the time scale of the reduction must be slow as the cyclic voltammogram shows changes happening over the course of hours.

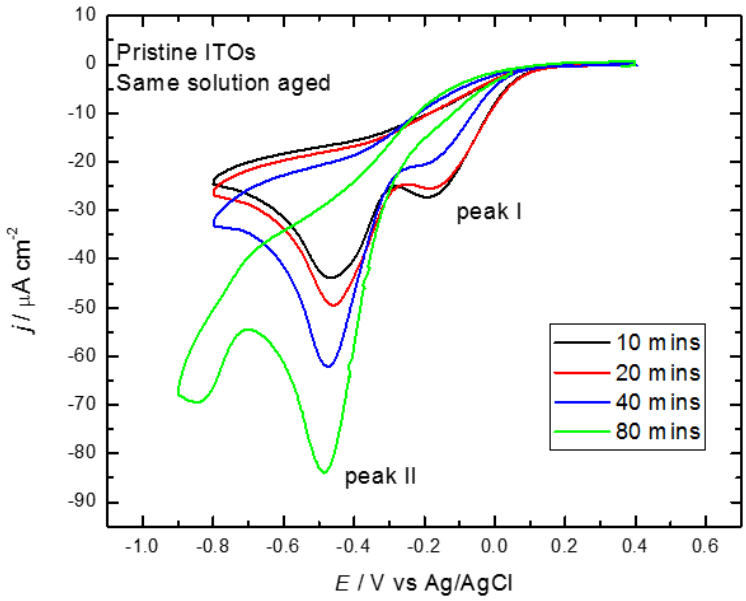

Figure 4.2. Cyclic voltammograms (20 mV/s) of pristine ITO electrodes in 0.25 mM $KAuCl_4$ aqueous solution of 0.1 M NaCl and 0.01 M 4-methoxypyridine (*Py*) at different time scale. (black, red, blue, and green solid lines).

4.3 Thermodynamic analysis

The starting source of gold in the reaction under the open circuit potential (OCP) condition is $KAuCl_4$ but the hydrolysis of tetrachloroaurate must be considered to identify the probable species participating in the ligand exchange with 4-methoxypyridine. The gold salt solution consisted of 0.1 M NaCl and 0.5 mM $KAuCl_4$ (pH ~ 6) which was mixed with a second solution consisting of 0.1 M *Py* and 0.1 M NaCl (pH ~ 9.8). The pH of the final solution was ~ 9. The speciation of the Au^{III} complex in solution prior to ligand exchange with *Py* can be determined by considering the equilibria,

$$AuCl_4^- + jH_2O \; f \quad AuCl_{4-j}OH_j^- + jCl^- + jH^+ \qquad \beta_j \qquad 4.1$$

Or

$$AuCl_4^- + jOH^- \; f \quad AuCl_{4-j}OH_j^- + jCl^- \qquad \beta_j' \qquad 4.2$$

where β is the stability constant and $1 \leq j \leq 4$. Equilibria 4.1 and 4.2 are related through the autoprotolysis of water, hence $\beta_j = K_w\beta_j'$ .Mironov and Tsvelodub [9] have reported the stability constants for these reactions (as shown in Table 4.1).

Table 4.1. Stability constants for the reaction of $AuCl_4^-$ with water where $1 \leq j \leq 4$. Reprinted from an open access journal. Copyright © 2000 Mironov, I. V.; Tsvelodub, L. D.

J	$\log_{10}(\beta_j')$	$\log_{10}(\beta_j)$
1	7.85	-6.15
2	14.79	0.79
3	20.92	6.92
4	25.98	11.98

Two conservation of mass equations can be written using the substitutions; $\left[AuCl_4^-\right] \equiv A$, $\left[AuCl_3OH^-\right] \equiv B$, $\left[AuCl_2\left(OH\right)_2^-\right] \equiv C$, $\left[AuCl\left(OH\right)_3^-\right] \equiv D$ and $\left[Au\left(OH\right)_4^-\right] \equiv E$.

$$A_o = A + B + C + D + E \quad (4.3)$$

$$Cl_o + 4A_o = Cl + 4A + 3B + 2C + D \quad (4.4)$$

where A_o and Cl_o are the initial concentrations of tetrachloroaurate and free chloride, respectively. The speciation of the Au^{III} complex can be determined as a function of pH, when the four stability equilibria and the two conservation of mass equations are combined. The results were derived using the symbolic math software, Maple and are shown in Figure 4.3 for A_o = 0.5 mM and Cl_o = 0.1 M.

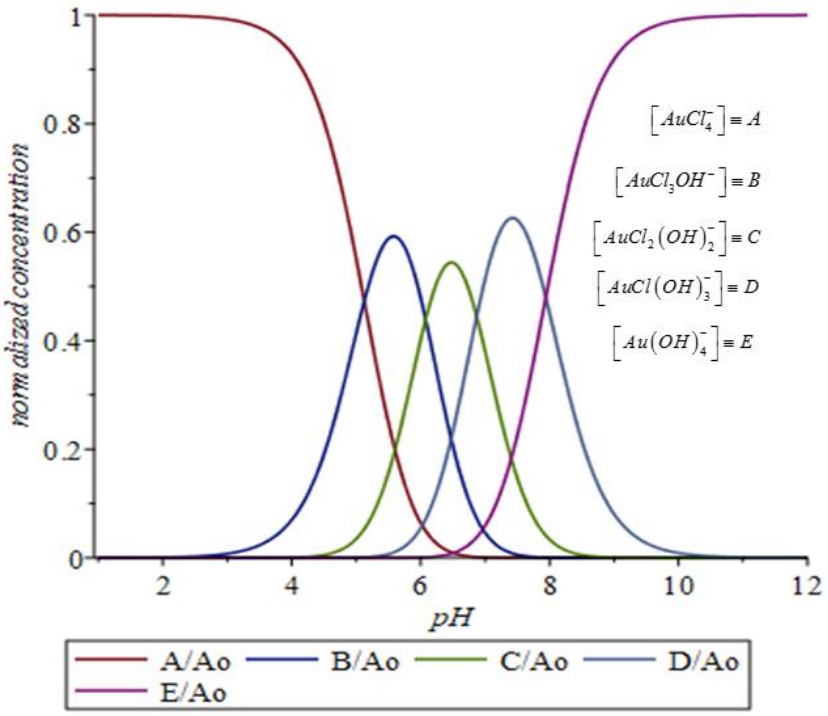

Figure 4.3. Speciation of different Au^{III} complex as a function of pH determined using Maple software.

Figure 4.3 indicates a mixture of several species with the majority components being *B*, *C* and *D* in the initial gold solution. The pH of the mixture after combining the *Py* and the Au solutions is ~ 9. As the solutions are prepared in aqueous medium (excess water), we assume that the rates of the hydrolysis reactions to be essentially instantaneous. The species participating in subsequent

ligand exchange reactions with *Py* are an almost exclusive mixture of $AuCl(OH)_3^-$ and $Au(OH)_4^-$ There is mass spectroscopic evidence for the presence of $AuPy_2^+$ in the reaction mixture and this indicates an electron transfer reaction. However, it is not obvious which species acts as the reducing agent. There are several literature reports describing the reduction of Au^{III} during ligand exchange studies by halides heavier than bromide.[10] For example, Elding and Olson [11] reported that the addition of free iodide to tetrachloroaurate led to the reduction of the latter and the formation of polyhalide species. However, ligand exchange by bromide was observed to proceed without reduction of the metal centre.[12] These observations are explained by considering the homogeneous redox reaction,

$$AuCl_4^- + 2X^- \rightarrow AuCl_2^- + X_2 + 2Cl^- \qquad 4.5$$

where X is a halogen. According to the standard electrode potentials provided in Table 4.2, the oxidation of the halide ion is favoured satisfactorily for iodide and not for bromide or chloride to make the above reaction thermodynamically possible. We therefore exclude chloride as the reducing agent in the present study. Similar reductions during ligand exchange have been reported for several species including thiourea, nitrite, dimethyl sulfoxide and pyridine.[10, 12, 13] The latter is highly pertinent to the current study although it is, perhaps, somewhat surprising to think of pyridine participating in redox processes given the very large electrochemical window where it remains inert

Table 4.2. Standard reduction potentials at 298 K for different reduction half reactions. Referenced partly from Petrucci, Harwood, Herring, and Madura. General Chemistry: Principles and Modern Applications. 9th ed. Pearson Education, 2007.

Rxn	E°
a. $AuCl_4^- + 2e^- \rightarrow AuCl_2^- + 2Cl^-$	0.926 V
b. $AuCl_2^- + e^- \rightarrow Au^0 + 2Cl^-$	1.154 V
c. $AuPy_2^+ + e^- \rightarrow Au^0 + 2Py$	$E_{I/0} = 1.69V + \frac{RT}{2F}\ln\left(\frac{a^2_{AuPy_2^+}}{\beta_I^2 a^4_{Py}}\right)$
d. $AuPy_2Cl_q(OH)^+_{2-q} + 2e^- \rightleftharpoons AuPy_2^+ + (2-q)OH^- + qCl^-$	$E^0_{III/I} = 1.41V + \frac{RT}{2F}\ln\left(\frac{\beta_I}{\beta_{III,q}}\right)$
e. $AuCl_{4-j}OH_j^- + 2e^- \rightarrow AuCl_2^- + (2-j)Cl^- + jOH^-$	j=0 0.926 V j=1 0.744 V j=2 0.949 V j=3 1.131 V j=4 1.280 V
f. $I_2 + 2e^- \rightarrow 2I^-$	0.535 V
g. $3I_2 + 2e^- \rightarrow 2I_3^-$	0.489 V
h. $I_3^- + 2e^- \rightarrow 3I^-$	0.534 V
i. $Br_2 + 2e^- \rightarrow 2Br^-$	1.087 V
j. $Cl_2 + 2e^- \rightarrow 2Cl^-$	1.396 V
k. $C_6H_5N^+O^- + 2H^+ + 2e^- \rightarrow C_6H_5N + H_2(g)$	1.01 V (estimated)

. Durovic *et al.* proposed that the oxidation of pyridine to form pyridine-N-oxide,

$$C_6H_5N + H_2O \rightarrow C_6H_5N^+O^- + 2H^+ + 2e^- \qquad 4.6$$

was coupled with the reduction of Au^{III} species but did not provide the standard reduction potential for this half-reaction. Using the standard enthalpies of formation of liquid pyridine [14] and crystalline pyridine-N-oxide [15], the standard enthalpy of reaction for $C_6H_5N^+O^-(aq) + H_2(g) \rightarrow C_6H_5N(aq) + H_2O(l)$ is estimated to be -195 kJ/mol. It is assumed that the enthalpy of solvation of pyridine and pyridine-N-oxide are similar. Furthermore, by assuming that the standard reaction entropy for the reaction as written in Eqn 4.6 is dominated by the consumption of H_2 (g), we estimate $\Delta G^o_{rxn} = -156\ \text{kJ/mol}$ and the standard reduction potential to be 1.01 V. An evaluation of the thermodynamic potential for this oxidation to couple spontaneously with the reduction of Au^{III} complex requires consideration of the nature of the complex species. The reduction potential for the Au^{III}/Au^{I} couple in the reaction,

$Au^{III} + 2e^- \rightleftharpoons Au^I$, is determined by the Nernst Equation,

$$E = 1.41V + \frac{RT}{2F}\ln\frac{a_{Au^{III}}}{a_{Au^I}} \qquad 4.7$$

Equation 4.7 can be combined with the stability coefficients for complex formation for both oxidation states of the Au. Mass spectrometry reveals three different Au^{III} complexes in solution; $AuPy_2(OH)_2^+$, $AuPy_2Cl(OH)^+$and $AuPy_2Cl_2^+$. The stability constants for these various species, $\beta_{III,\,q}$, are unknown but can be expressed generally in terms of the following chemical equilibria, with $q \in (0,1,2)$

$$Au^{III} + 2Py + qCl^- + (2-q)OH^- \rightleftharpoons AuPy_2Cl_q(OH)_{2-q}^+ \qquad \beta_{III,\,q} \qquad 4.8$$

Similarly, the stability constant for $AuPy_2^+$ is given by Eqn 4.9.

$$Au^I + 2Py\ f \quad AuPy_2^+ \qquad \beta_I \qquad 4.9$$

Substitution of equilibrium expressions into equation 4.7 yields,

$$E_{III/I} = 1.41V + \frac{RT}{2F}\ln\left[\left(\frac{\beta_I}{\beta_{III,q}}\right)\left(\frac{a_{AuPy_2Cl_q(OH)_{2-q}^+}}{a_{AuPy_2^+}a_{OH^-}^{2-q}a_{Cl^-}^q}\right)\right] \qquad 4.10$$

and the standard potential for the reduction of the Au^{III} complex into $AuPy_2^+$is obtained by setting all activities to unity

$$E^0_{III/I} = 1.41V + \frac{RT}{2F}\ln\left[\frac{\beta_I}{\beta_{III,q}}\right] \qquad 4.11$$

For *Py* to be the reducing agent, the right-hand side of Eqn 4.11 must be greater than the standard reduction potential of *Py*-N-oxide. Estimating the latter to be close to the value derived above for

pyridine-N-oxide (i.e. 1.01 V), it is apparent that $\beta_{III,q}$ must be larger than β_I by approximately 14 orders of magnitude. For reference the base 10 logarithm of the stability constants for $AuCl_4^-$, $AuCl_2^-$, $Au(CN)_4^-$ and $Au(CN)_2^-$ (26, 9, 56 and 38 respectively)[16] are consistent with this required ratio and support the contention that 4-methoxypyridine is oxidized to form the N-oxide during the spontaneous reduction of the Au^{III}-complex.

4.4 Kinetic analysis

An understanding of the chemistry that occurs in the Au^{III}-MOP system benefits from an attempt to study the kinetics of the various solution phase reactions. Mass-spectrometry analysis revealed the presence of both a redox reaction (i.e. the formation of $AuPy_2^+$) as well as various Au^{III}-MOP complexes resulting from ligand exchange reactions. The time scale of the homogeneous redox reaction was slow enough that the kinetics of this reaction could be observed on the time scale of tens of minutes. On the other hand, the initial ligand exchange reactions will be shown below to occur on the millisecond time scale and stopped flow spectrophotometry was required to study the kinetics of these reactions.

4.5 Spectrophotometric measurements

UV-Vis spectrophotometry is a convenient tool for studying ligand exchange kinetics [17] and has been used extensively when there is an absorbance change as a function of reaction time. A conventional cell, most commonly used in UV-Vis spectrophotometry, is adequate for reactions with half-lives greater than several minutes. However, reactions that proceed on a timescale of seconds or faster require a specialized equipment known as a Rapid Kinetics Accessory (or Stopped-Flow Apparatus).[18] A Stopped-Flow apparatus can be used to measure fast reactions that provide instantaneous mixing and recording of data on a tens-of-millisecond time scale.

4.5.1 Stopped-flow experimental measurements

Stopped-flow is a type of flow injection analysis with a quartz cuvette as the sample cell. The sample cell usually has a minimal volume allowing good sensitivity for absorption measurements with a 10 mm pathlength. Such a cell has a dead time typically around millisecond range, which

represents the earliest time point at which reactions can be monitored.[18] The kinetic studies of the reaction between $KAuCl_4$ and MOP were determined using the stopped-flow UV-Vis spectrophotometer. The stop-flow apparatus is connected to the UV-Vis spectrophotometer through a remote-send-cable that is attached to an accessory controller port on the instrument. The reactants (aqueous solution of $KAuCl_4$ and MOP) are placed separately in two drive syringes, labelled syringe 1 and 2, as shown in Figure 4.4. Upon pressing the plunger, the solutions travel separately to the cuvette and mix up only upon entering the cell. The previously reacted solution will be ejected into a waste syringe, which moves back until hitting a micro switch. The solution then stops flowing into the cell and data collection begins instantaneously. This eliminates any delay caused by a manual start of the instrument.

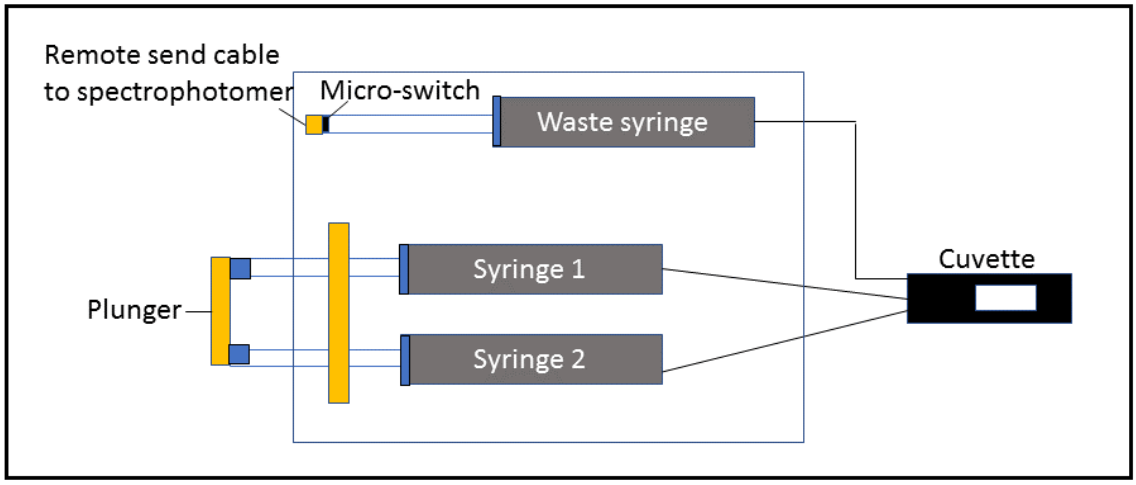

Figure 4.4. Schematic diagram of Stopped-Flow Apparatus

The syringes and the sample cell was rinsed with Milli-Q water after every flow injection. The drive syringes of equal volume were used and operated by gas pressure. The aqueous solutions of $HAuCl_4$ and MOP held in the drive syringes were mixed in different ratios. The kinetics under observation indicates the concentration of components after mixing, whereas pre-existing equilibria reflect the concentration in the drive syringes. The instrument parameters for the stopped-flow apparatus was as follows: chosen wavelength (nm), average time: 0.033s, Y (Abs) min: 0, Y(Abs) max: 1.0, cycle: 0 min, stop time: 5 – 10 min. Multiple series of scan methods and stopped-flow experiments were conducted with a fixed concentration of $AuCl_4^-$ and variable *Py*

concentration or variable NaCl concentration. The addition of *Py* to the gold solution caused a rapid change in the absorbance at specific wavelengths, following a decay path, as explained in the results section of this chapter, the rate of which depends on the concentration of pyridine. The reaction was monitored at 325 nm.

4.6 Results and Discussions

The rapid kinetics of the *Py* ligand exchange when an aqueous solution of gold and *Py* is mixed were studied using UV-Vis spectroscopy. Figure 4.5 shows the progression of time resolved spectra after rapidly mixing an equimolar solution of $AuCl_4^-$ and *Py* (both 0.25 mM) in 0.1 M NaCl.

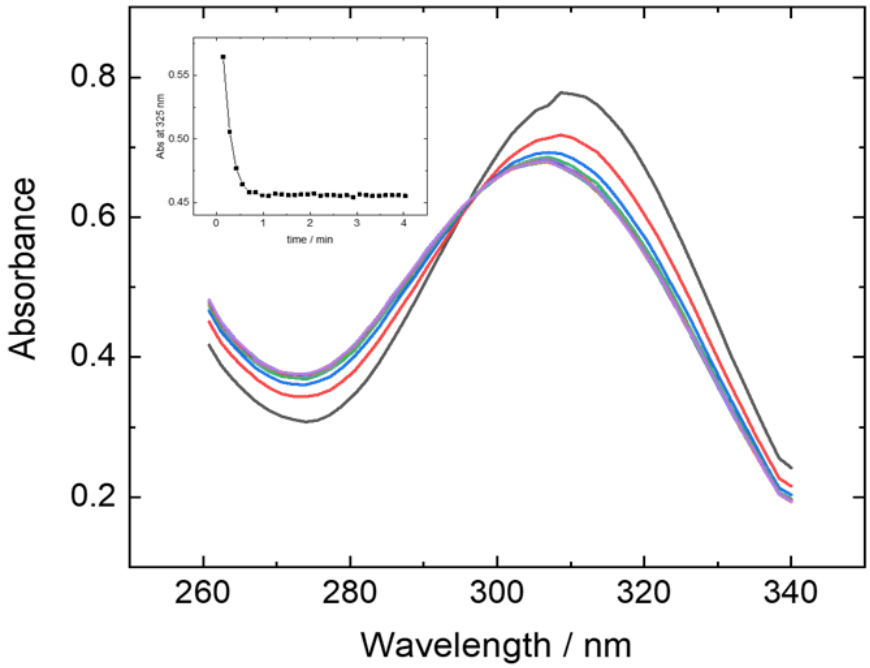

Figure 4.5. Scan absorbance data for lower MOP concentrations at a wavelength range of 250 nm to 340 nm by mixing equimolar solution of $AuCl_4^-$ and *Py* in 0.1M NaCl. (Inset: Absorbance at 325nm vs time).

The pH of the final solution was approximately 8.5 even with this low concentration of 4-methoxypyridine, which is sufficiently basic to allow the assumptions described above to be still valid. The presence of an isosbestic point at 296 nm is consistent with previous reports [12] for the

reaction of pyridine with tetrachloroaurate in aqueous solutions. The inset figure implies that the reaction either runs to completion or reaches equilibrium as the absorption plateaus after ~ 0.5 minutes

The observation of an isosbestic point and the subsequent establishment of a stable spectrum indicates that at stoichiometric (or sub-stoichiometric) ratios of gold and *Py*, the only process that needs to be considered is the simple substitution reaction,

$$AuCl\left(OH\right)_3^- + Py \rightarrow AuPy\left(OH\right)_3 + Cl^- \qquad 4.12$$

The data poses a picture where the ratio of Au-MOP tends to be crucial in deciding the kinetics of the reaction. A minimal gold to *Py* ratio is required so that it reacts to give an isosbestic point and, at the same time, confirms the completion of the reaction. However, UV-Vis absorption experiments involving an excess of *Py* do not show an isosbestic point but rather exhibit a continual decrease in absorption. This is shown in the absorption spectra for a 3:1 ratio of *Py*:Au (Figure 4.6). The continual bleaching of the absorption spectra is consistent with the reduction of Au^{III} to form Au^{I} species as described above based on mass spectrometry and electrochemical results.

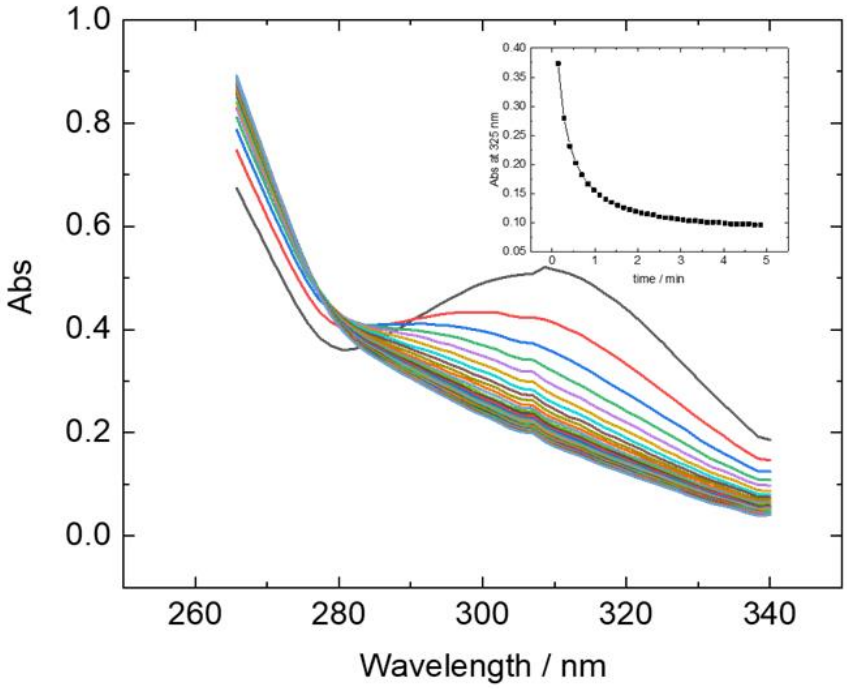

Figure 4.6. Scan absorbance data for 3:1 *Py*:Au concentrations at a wavelength range of 250 nm to 340 nm. (Inset: Absorbance at 325 nm vs time).

The stopped flow experiment measurement of the absorbance at 325 nm, run for a long period of time, after rapid mixing of a 200:1 molar ratio of *Py* and Au^{III} is shown in Figure 4.7. The kinetic trace reveals three distinct slopes labelled *a*, *b* and *c* that occur over considerably different time scales. The first process is extremely fast and is separated from the onset of process *b* by a region where the absorbance at 325 nm largely remains invariant with time. Based on the mass spectrometry results, process *a* is interpreted to be the fast ligand exchange of a single *Py* molecule on the Au^{III} centre (i.e. reaction 4.12). As the final reaction mixture is known to contain two *Py* ligands, process *b* is believed to be the much slower formation of $AuPy_2Cl_q(OH)^{+}_{2-q}$.

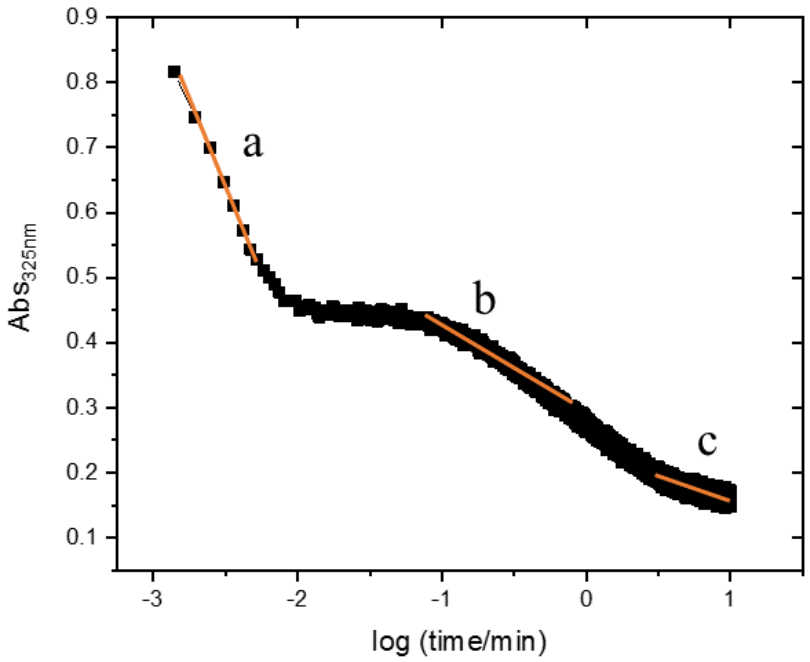

Figure 4.7. Stopped-flow method analysis, describing three different process, at 325nm when 0.05 M MOP is mixed with 0.25 mM $KAuCl_4$ in 0.1 M NaCl.

This is consistent with previous reports that show that the formation of Au^{III} with two pyridine molecules in the inner sphere only occurs in solutions with large excesses of pyridine.[19] The last process occurs much more slowly and is consistent with the timescales of electrochemical studies showing the slow formation of $AuPy_2^+$. The clear separation between processes *a* and *b* indicates that the former runs either to completion or establishes equilibrium on a time scale much faster than the onset of process *b*, which allows the kinetics of this reaction to be decoupled from the subsequent reactions.

Two series of stopped flow experiments were conducted with a fixed concentration of $AuCl_4^-$ and either a) variable *Py* concentration in 0.1 M NaCl or b) variable NaCl concentration in 50 mM *Py*. The short time transients (corresponding to reaction *a*) were fit to a single exponential decay and the apparent rate constant plotted against either [*Py*] or [Cl^-] (Figure 4.8). The plots show that the apparent rate constant increases with increasing concentration of 4-methoxypyridine but decreases with increasing chloride concentration.

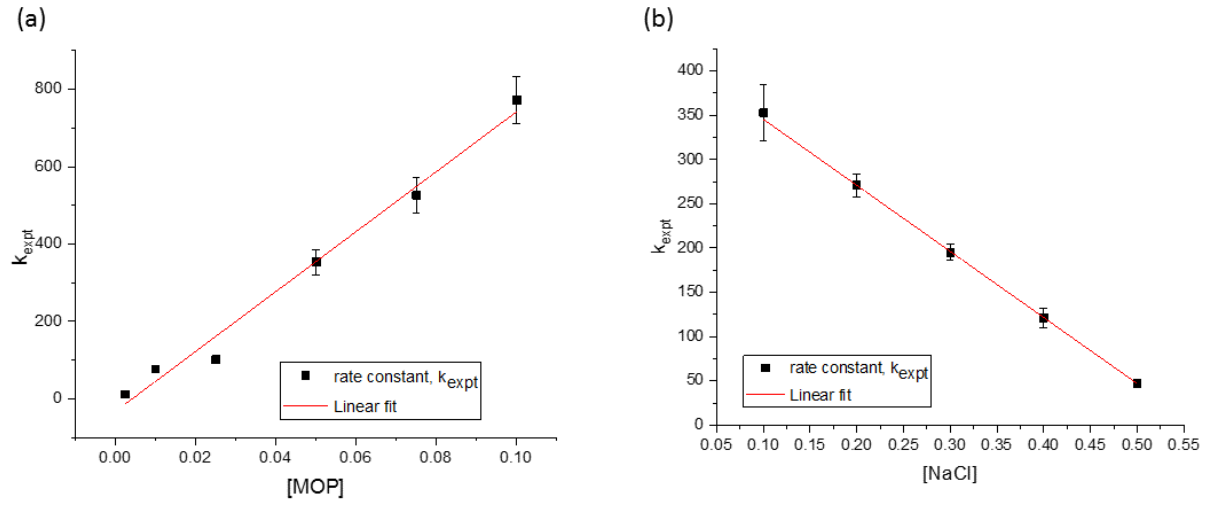

Figure 4.8. Graph relating experimental rate constant with different concentrations of (a) MOP and (b) NaCl.

For understanding the kinetic analysis in homogenous solutions, Gray's study [20] in determining the reaction rates for ligand substitutions in square planar complexes is a good starting place. The parallel (two rate constant) model described in his studies was consistent with the two-step mechanism which has been proposed for ligand substitutions in square planar metal complexes[21] and seems relevant to the current Au-*Py* studies. The general rate law for ligand substitutions in square planar metal complexes is best described [22, 23] as, $Rate = (k_1 + k_2[Y])[ML_4]$, where k_1 and k_2 are first and second order rate constants, respectively, and Y and $[ML_4]$ are the concentrations of the ligand and initial metal complex. Rich and Taube [24, 25] were the first to discover this form of rate law in square planar reactions for the exchange of Cl^- with $AuCl_4^-$. Since then, the kinetics of ligand exchange in square planar complexes has been very consistent with this rate law form with few exceptions.

Gray studied the replacement of a halide ligand in Pt(II) complexes. The two-step mechanism explained in his work primarily involved the slow reaction with water as the solvent followed by a fast exchange with the incoming Y ligand represented by the first order rate constant, k_1. The second order rate constant, k_2, arises from the direct bimolecular reaction (SN_2) between the incoming ligand and the complex. The pseudo first order rate constant, k_{obs}, extracted from the

measurements was given by the equation, $k_{obs} = (k_1 + k_2[Y])$, where plots of k_{obs} vs Y gave straight lines with slopes, k_2 and intercept, k_1. According to Gray, the two-step mechanism was found to agree with the two-term rate law and the kinetic model proposed was verified with other conventional methods such as radioisotope and conductivity methods.

With this understanding of Gray's model, a mechanism for the Au-*Py* system was deduced here. One possibility is that process *a* is the establishment of an equilibrium between $AuCl(OH)_3^-$ and $AuPy(OH)_3$.

$$AuCl\left(OH\right)_3^- + Py \underset{k_b}{\overset{k_f}{\rightleftharpoons}} AuPy\left(OH\right)_3 + Cl^- \qquad 4.13$$

By ensuring that the starting concentration of tetrachloroaurate, $[A]_o$, is much smaller than the concentration of *Py* and Cl^-, pseudo-first order rate constants can be defined.

$$k_b^{/} = k_b\left[Cl^-\right] \qquad 4.14$$

$$k_f^{/} = k_f\left[Py\right] \qquad 4.15$$

Combining the differential rate law with conservation of mass requirements. i.e.

$[A]_0 = [AuCl(OH)_3^-] + [AuPy(OH)_3]$, results in the integrated rate equation

$$\frac{\left[AuCl\left(OH\right)_3^-\right]_t}{\left[A\right]_0} = \left[\frac{k_b^{/}}{k_{app}} + \left(1 - \frac{k_b^{/}}{k_{app}}\right)e^{-k_{app}t}\right] \qquad 4.16$$

with $k_{app} = k_b^{/} + k_f^{/}$. In the limit of large *t*, Eqn 4.16 leads to an expression for the equilibrium concentration of $AuCl\left(OH\right)_3^-$

$$\frac{\left[AuCl\left(OH\right)_3^-\right]_{eq}}{\left[A\right]_0} = \frac{\left[Cl^-\right]}{\frac{k_f}{k_b}\left[Py\right] + \left[Cl^-\right]} \qquad 4.17$$

The pre-equilibrium model predicts that the observed rate constant should increase for both increasing [Cl^-] and increasing [Py], in contrast with the data shown in Figure 4.8. Furthermore, $[AuCl(OH)_3^-]_{eq}$ is predicted to depend on the concentration of both ligands, whereas the experimental absorbance transients show, within some experimental scatter, the same absorbance at 325 nm at the end of process a (Figure 4.9). This implies that the initial ligand exchange reaction runs to completion and invalidates the pre-equilibrium model.

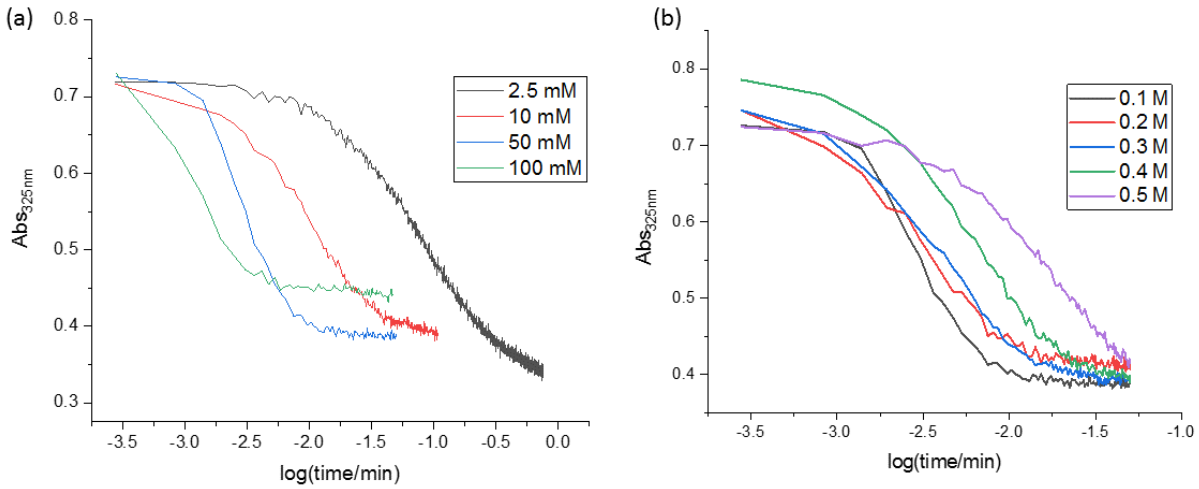

Figure 4.9. Stopped-flow method analysis for process a at 325 nm when (a) different concentration MOP is mixed with 0.25 mM $KAuCl_4$ in 0.1 M NaCl (b) different concentration NaCl is mixed with 0.25 mM $KAuCl_4$ in 0.05 M MOP.

The type of associative mechanism, as explained by Gray for ligand replacement in square planar complexes, involves two parallel paths to the final product. One path proceeds through the formation of an intermediate solvent-metal complex and the second through the direct ligand exchange. If the primary species involved in ligand exchange is $AuCl(OH)_3^-$, the four steps of the associative mechanism are,

$$AuCl(OH)_3^- + H_2O \xrightarrow{k_1} Au(OH_2)(OH)_3 + Cl^- \qquad 4.18$$

$$Au(OH_2)(OH)_3 + Cl^- \xrightarrow{k_{-1}} AuCl(OH)_3^- + H_2O \qquad 4.19$$

$$Au(OH_2)(OH)_3 + Py \xrightarrow{k_a} AuPy(OH)_3 + H_2O \qquad 4.20$$

$$AuCl(OH)_3^- + Py \xrightarrow{k_2} AuPy(OH)_3 + Cl^- \qquad 4.21$$

Reaction 4.19 is only relevant if the concentration of free chloride in the solution is non-zero. If the concentration of free chloride is zero or negligibly small, reaction 4.19 can be omitted and the differential rate law for the concentration of $AuCl(OH)_3^- \equiv D$, is $-d[D]/dt = k_{app}[D]$, where $k_{app} = (k_1[H_2O] + k_2[Py])$, and is consistent with the experimentally observed linear increase in rate constant with increasing [*Py*] under fixed chloride concentration, i.e. $k_{app} = k_1^{/} + k_2[Py]$. However, for the current Au-*Py* system under study, the observed dependence on the rate with the concentration of free chloride indicates that reaction 4.19 must also be accounted in the kinetic analysis. Thus, considering the backward reaction is a necessary modification to the existing parallel two rate law method. With the substitution, $Au(OH_2)(OH)_3 \equiv I$, the differential rate equation becomes

$$\begin{aligned} \frac{d[D]}{dt} &= k_{-1}[I][Cl^-] - k_1[D][H_2O] - k_2[D][Py] \\ &= k_{-1}[I][Cl^-] - k_1^{/}[D] - k_2[D][Py] \end{aligned} \qquad 4.22$$

Under the steady-state approximation, i.e. $d[I]/dt = 0$,

$$[I] = \frac{k_1^{/}[D]}{k_a[Py] + k_{-1}[Cl^-]} \qquad 4.23$$

which, upon substitution into 4.22, provides

$$\begin{aligned} \frac{d[D]}{dt} &= -\left\{ k_1^{/} + k_2[Py] - \frac{k_{-1}k_1^{/}[Cl]}{k_a[Py] + k_{-1}[Cl^-]} \right\}[D] \\ &= -k_{app}[D] \end{aligned}$$

If $k_a[Py] ? \ k_{-1}[Cl^-]$

$$k_{app} \approx k_1^{/} + k_2[Py] - \frac{k_{-1}k_1^{/}[Cl^-]}{k_a[Py]} \quad 4.24$$

For fixed *Py* concentration, the mechanism predicts the observed linear decrease in the measured rate constant with increasing Cl^- concentration. On the other hand, the observed increase in k_{app} with increasing [*Py*] is consistent with Eqn 4.24 if the second term on the right-hand side is dominant.

Thus, the proposed model was successful as it agreed with the experimental results observed for the reaction involved in process a. The kinetic model represented with a steady-state approximation shows the correlation of the rate constants to the changes in the concentrations of *Py* and Cl^- and proposes a two-step mechanism for process a involving a ligand substitution.

4.7 Conclusion

In summary, this chapter reports a detailed study of the kinetics of the Au-*Py* system in aqueous solutions using spectrophotometric and electrochemical methods. The results provide convincing evidence of the existence of Au^I–*Py* complex and importantly, provides new insight into a kinetic model developed using Stopped-flow methods of UV-Vis Spectrophotometry. The kinetic studies presented in this chapter shows that $AuCl_4^-$ undergoes both ligand-exchange reactions and a redox reaction in the presence of 4-methoxypyridine. This reduction of Au^{III} species to Au^I species has also been supported through electrochemical measurements. The increase in the peak current that confirms the reduction of Au^{III} species to Au^I species in the presence of MOP when the solution was aged was the key factor for the start of the research to study the mechanism of the reaction. Three distinct slopes (a, b and c) occurring at different time scales were revealed in the kinetic trace with the help of stopped-flow absorption spectroscopy. Process a is interpreted to be a fast ligand exchange to form $AuPy(OH)_3$ and process b is assigned to slower formation of $AuPy_2Cl_q(OH)_{2-q}^+$ as the final mixture is known to contain 2 *Py* ligands from the mass spectroscopic results. The final process c is again the slow formation of $AuPy_2^+$. The system reveals a spontaneous reduction of the Au^{III} complex, and the stability constant ratio data is

consistent with the idea that it is 4-methoxypyridine that gets oxidised to form the N-oxide. The kinetic model described in this chapter was made on the basis of Gray's model with a significant modification to extract the kinetic parameters from the stopped-flow experiments, with a focus on pseudo-first order kinetic studies and relative rate determinations. It is likely that understanding the intermediates and further the mechanism of the Au-*Py* reaction helps to manipulate the reaction conditions to generate better gold nanostructures. Insight into the homogenous chemistry of the Au-*Py* system explained in this chapter was one of the crucial steps to undertake to perform voltammetric studies and the nucleation and growth study of the gold nanostructures.

4.8 References

1. Abdelsalam, M.E., et al., *Electrochemical SERS at a structured gold surface.* Electrochem. Commun., 2005. **7**(7): p. 740-744.

2. Mahajan, S., et al., *Reproducible SERRS from structured gold surfaces.* Phys. Chem. Chem. Phys., 2007. **9**(45): p. 6016-6020.

3. Liao, H. and J.H. Hafner, *Monitoring Gold Nanorod Synthesis on Surfaces.* J. Phys. Chem. B, 2004. **108**(50): p. 19276-19280.

4. Mieszawska, A.J., G.W. Slawinski, and F.P. Zamborini, *Directing the Growth of Highly Aligned Gold Nanorods through a Surface Chemical Amidation Reaction.* J. Am. Chem. Soc., 2006. **128**(17): p. 5622-5623.

5. Mieszawska, A.J. and F.P. Zamborini, *Gold Nanorods Grown Directly on Surfaces from Microscale Patterns of Gold Seeds.* Chem. Mater., 2005. **17**(13): p. 3415-3420.

6. Taub, N., O. Krichevski, and G. Markovich, *Growth of Gold Nanorods on Surfaces.* J. Phys. Chem. B, 2003. **107**(42): p. 11579-11582.

7. Umar, A.A., et al., *Formation of High-Yield Gold Nanoplates on the Surface: Effective Two-Dimensional Crystal Growth of Nanoseed in the Presence of Poly(vinylpyrrolidone) and Cetyltrimethylammonium Bromide.* Cryst. Growth Des., 2009. **9**(6): p. 2835-2840.

8. Abdelmoti, L.G. and F.P. Zamborini, *Potential-Controlled Electrochemical Seed-Mediated Growth of Gold Nanorods Directly on Electrode Surfaces.* Langmuir, 2010. **26**(16): p. 13511-13521.

9. Mironov, I., Tsvelodub, and Ld, *Equilibria of the Substitution of Pyridine, 2,2'-Bipyridyl, and 1,10-Phenanthroline for Cl- in AuCl- 4 in Aqueous Solution.* Russian Journal of Inorganic Chemistry, 2001. **46**: p. 143-148.

10. Richens, D.T., *Ligand Substitution Reactions at Inorganic Centers.* Chemical Reviews, 2005. **105**(6): p. 1961-2002.

11. Elding, L.I. and L.F. Olsson, *Kinetics and mechanism for reduction of tetrachloro- and tetrabromoaurate(III) by iodide.* Inorganic Chemistry, 1982. **21**(2): p. 779-784.

12. Đurović, M.D., et al., *Studies on the reactions of [AuCl4]− with different nucleophiles in aqueous solution.* Dalton Transactions, 2014. **43**(23): p. 8620-8632.

13. Đurović, M.D., Ž.D. Bugarčić, and R. van Eldik, *Stability and reactivity of gold compounds – From fundamental aspects to applications.* Coordination Chemistry Reviews, 2017. **338**: p. 186-206.

14. Usher, A., D.C. McPhail, and J. Brugger, *A spectrophotometric study of aqueous Au(III) halide–hydroxide complexes at 25–80°C.* Geochimica et Cosmochimica Acta, 2009. **73**(11): p. 3359-3380.

15. Shaofeng, L. and G. Pilcher, *Enthalpy of formation of pyridine-N-oxide: the dissociation enthalpy of the (N□O) bond.* The Journal of Chemical Thermodynamics, 1988. **20**(4): p. 463-465.

16. Marsden, J. and I. House, *The chemistry of gold extraction*. 2006: SME.

17. De Caro, C. and C. Haller, *UV/VIS Spectrophotometry - Fundamentals and Applications*. 2015.

18. Bagshaw, C.R., *Stopped-Flow Techniques*, in *Encyclopedia of Biophysics*, G.C.K. Roberts, Editor. 2013, Springer Berlin Heidelberg: Berlin, Heidelberg. p. 2460-2466.

19. Peshchevitskii, B.I., G.I. Shamovskaya, and G.D. Mal'chikov, *Reactivity of pyridine toward [AuCl4]*. Zh. Neorg. Khim., 1971. **16**(2): p. 347-50.

20. Gray, H.B., *Rates of some substitution reactions of platinum(II) complexes.* J. Am. Chem. Soc., 1962. **84**: p. 1548-52.

21. *Mechanisms of Inorganic Reactions. By Fred Basolo and Ralph G. Pearson. John Wiley and Sons, Inc., New York, 1958. xi + 426 pp. 15 × 22.5 cm. Price $11.75.* Journal of the American Pharmaceutical Association, 1958. **47**(11): p. 838-838.

22. Basolo, F., et al., *Kinetics of the reaction of alkyl and aryl compounds of the nickel group with pyridine.* J. Chem. Soc., 1961: p. 2207-15.

23. Basolo, F., H.B. Gray, and R.G. Pearson, *Mechanism of substitution reactions of complex ions. XVII. Rates of reaction of some Pt(II) and Pd(II) complexes with pyridine.* J. Am. Chem. Soc., 1960. **82**: p. 4200-3.

24. Rich, R.L. and H. Taube, *The uncatalyzed exchange of Cl- and AuCl4.* J. Phys. Chem., 1954. **58**: p. 1-5.

25. Rich, R.L. and H. Taube, *The induced exchange of Cl- and AuCl4-. Evidence for Au(II).* J. Phys. Chem., 1954. **58**: p. 6-11.

CHAPTER 5

ELECTROCHEMISTRY OF AU-MOP COMPLEXES ON INDIUM TIN OXIDE (ITO)

5.1 Manuscript Author Contributions

The current Chapter is part of the manuscript published in *J. Phys. Chem. C* 2016, 120, 45, 26150–26158 which was authored by four members of the Burgess group. Even though the majority of the research work was performed by the first author (the thesis writer), the contributions from the co-authors are substantial. First, and foremost, to be mentioned is the role of Ian. J. Burgess. He not only supervised my research work but also had the chief role in writing the manuscript. The work performed by the second and third authors are discussed in the next chapter (Chapter 6) as it is a subsequent continuation of the current chapter. All the co-authors have been notified about the plan to incorporate their sections into my thesis and their permissions would be available upon request.

5.2 Introduction

An electrochemical approach that precisely controls the reduction conditions to nucleate and grow nanostructures on conductive electrodes has advantageous compared to other techniques that produce nanoparticles. In principle, electrochemical methods provide a simple route to generate a homogenous and densely populated metal nanoparticle films. Such metal nanostructured surfaces have great applications in electrocatalysis [1, 2] and surface enhanced Raman scattering (SERS) based sensing in biomedical and other related applications.[3-5]

The size and shape of metal nanocrystals also play crucial roles in dictating optical properties, and a variety of electrodeposited metal structures have been reported including spheres,[6-9] nanoflowers,[10-12] plates,[2, 13] rods,[1, 14] urchins,[15] spikes,[16] and dendrites[17, 18] either through the use of shape directing surfactants or by controlling the electrodeposition parameters.[19, 20] Two limiting cases that exist for electrochemical deposition and crystal growth are (i) deposition near-equilibrium conditions where surface free energies govern the resulting nanocrystal shapes[21] and (ii) nonequilibrium conditions where surface kinetics and material transport determine the crystal shape.[22] The latter often results in the formation of branched and dendritic shapes.[23-25] Dendritic growth can be promoted if the growth rate of the deposited phase exceeds the flux of precursor (gold ions) to the electrochemical interface. However, this can be difficult to quantitate as the growing nanocrystallites significantly distort the diffusion layer at the electrochemical interface.[19] Capitalizing on the advantages offered by electrodeposition in manipulating the growth rate of nanocrystals requires in-depth knowledge of the electrochemical behavior of the precursor solution. However, the electrochemical behavior of even relatively simple precursor species such as $AuCl_4^-$ is quite complicated,[26] and the presence of surfactants and ligands often provides a medley of electrochemical responses.[27]

Previous members in our group have shown that pyridine derivatives can serve as excellent stabilizers and shape directors in the formation of aqueous dispersions of anisotropic gold nanocrystals.[28-31] An anisotropic nanocrystal growth mechanism was proposed on the basis of electrosorption and potentiometry studies that purported formation of Au^I intermediates and the selective adsorption of pyridine derivatives on specific crystallographic facets of the growing nanoparticles.[28] The former point is intriguing as Xia and co-workers have recently shown that the size and shape of Au nanoparticles formed from the reduction of Au^I species differ from analogous experiments with Au^{III} species.[32] Similarly, the electrodeposition of Au(I) cyanide complexes has been shown to provide unique nanoplates that cannot be formed from $AuCl_4^-$.[2] The absence of d-band electronic transitions in Au^I complexes makes it very difficult to conclusively detect them in situ, and it is challenging to provide direct evidence of their existence and significance when nanocrystals are derived from Au^{III} precursors.

This Chapter thereby reports a detailed study of the electrochemical behavior of Au-*Py* (*Py* = 4-methoxypridine) complexes in aqueous solutions. The results provide compelling evidence of

the existence of Au^{I}–*Py* complexes but, just as importantly, allow new insight into the electrochemistry pertinent to the formation of both dispersed and electrodeposited Au nanoparticles. This insight is used to help engineer densely packed films of highly anisotropic Au nanocrystals on conductive glass (Indium Tin Oxide, ITO) substrates.

5.3 Results and Discussions

5.3.1 Detailed voltammetric study of Au-MOP complexes

An elaborate study on the Au-MOP electrochemistry on ITO electrodes as a function of electrode potential was completed in this chapter. The addition of 0.25mM $KAuCl_4$ to an aqueous solution of 0.1 M NaCl and 0.1 M MOP showed two irreversible voltammetric peaks on the cathodic scan from the open-circuit potential (Figure 5.1).

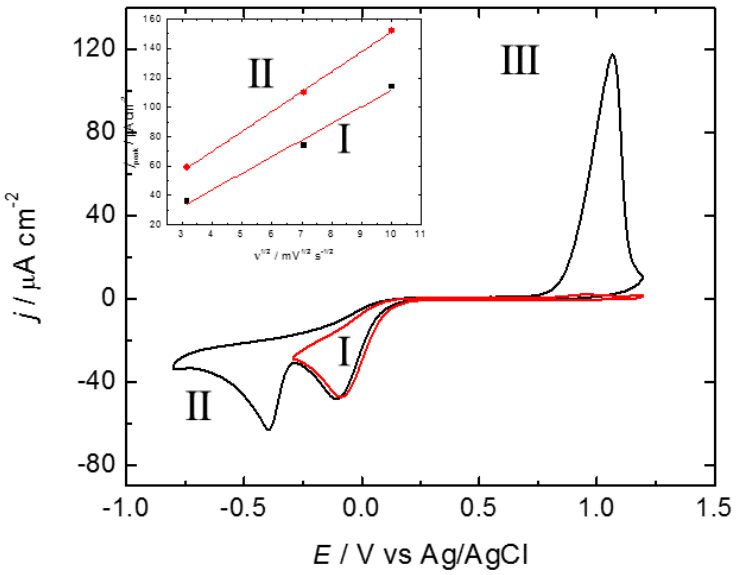

Figure 5.1. Cyclic voltammograms (20 mV/s) of ITO electrodes in 0.25 mM $KAuCl_4$ aqueous solution of 0.1 M NaCl and 0.1 M 4-methoxypyridine (black and red solid lines for full and half CV). The inset shows the scan rate dependence for the peaks I and II. Each scan rate was performed on a fresh sample of ITO.

Peak I appeared at ca. −0.10 V and had a magnitude roughly two-thirds that of the more intense signal (peak II) observed at ca. −0.40 V. It was observed in the earlier chapter (Chapter 4) that the peak currents of both the peaks, peak I and peak II, changed with the reaction time as the peak

amplitudes were dependent on the mixing time of the gold salt and MOP. The return potential sweep to positive potentials showed only a single anodic peak (peak III) at 1.1 V. Peak III was absent if the initial, negative potential scan direction was reversed at −0.25 V. The voltammetry implied a two-step reduction process involving the formation of an Au^{I} intermediate species (peak I) and its subsequent reduction to Au^{0} (peak II), which can be stripped from the anode at highly positive potentials (peak III). Both the cathodic peaks (I and II) were found to be diffusion controlled, as evidenced by the chronoamperometry measurements explained later in this chapter and the fact that the first scan peak currents increase linearly with the square root of scan rate (inset of Figure 5.1). This eliminates the possibility that either of the peaks result from the electrochemistry of surface-adsorbed species, as seen in the case for cyanide-stabilized Au^{I} species [33-35]. A catalytic crossover near 0 V on the anodic scan might also be expected as Au electrodeposition is more facile on Au than on ITO. Its absence may be due to the strong adsorption of the 4-methoxypyridine on the gold that gets deposited on the surface.[31]

The integration of the full-scan CV shown in Figure 5.1 revealed that the charge passed in the cathodic sweep is 2.5 times larger than the charge passed in the anodic scan. This can be partially explained by the incomplete dissolution of electrodeposited Au^{0}, which is known to occur when Au is deposited on non-metallic electrodes.[19] Nevertheless, the amount of residual gold after the potential excursion to stripping potentials is expected to be quite small and cannot fully explain the charge ratios for the anodic and cathodic scans. The integration results suggest that some of the charge passed in the cathodic sweep produces Au^{0} species that do not deposit on the ITO. This research proposes that the disproportionation of electrogenerated Au^{I} to form Au^{0} and Au^{III} is largely responsible for the lower than expected amounts of electrodeposited gold. Although Au^{I} disproportionation is generally a slow process, it is greatly catalyzed in the presence of metallic gold [36], which will begin to form on the ITO at the onset of peak II. The Burgess group has previously shown that 4-methoxypyridine is an excellent gold nanoparticle stabilizer [31], and evidence is provided below (Scheme 5.1), indicating that the Au^{0} formed by disproportionation exists primarily in the form of nanoparticles dispersed in the electrolyte. Double potential step chronoamperometry experiments on the Au-MOP system provided further evidence supporting the interpretation of the voltammetry. The details of the chronoamperometry measurements and

the determination of integrated current at a given potential have already been discussed in Chapter 2.

$$AuCl_4^- + 3H_2O \rightleftharpoons AuCl(OH)_3^- + 3Cl^- + 3H^+ \quad 5.1a$$

$$AuCl(OH)_3^- + Py \rightleftharpoons AuPy(OH)_3 + Cl^- \quad 5.1b$$

$$AuPy(OH)_3 + qCl^- + Py \rightleftharpoons AuPy_2Cl_q(OH)_{2-q}^+ + (q+1)OH^- \quad 5.1c$$

$$AuPy_2Cl_q(OH)_{2-q}^+ + 2e^- \rightleftharpoons AuPy_2^+ + (2-q)OH^- + qCl^-, \text{(Peak I)} \quad 5.2$$

$$3AuPy_2^+ + xCl^- \rightleftarrows (Au^{III}Py_{4-x}Cl_x)^{3-x} + 2Au^o(np) + (x+2)Py \quad 5.3$$

$$AuPy_2^+ + e^- \rightleftarrows Au^o + 2Py, (Peak\ II) \quad 5.4$$

$$Au^0 + 2Py + qCl^- + (2-q)OH^- \rightleftharpoons AuPy_2Cl_q(OH)_{2-q}^+, (Peak\ III) \quad 5.5$$

Scheme 5.1: Proposed reactions of Au-MOP electrochemistry

The results of the chronoamperometry experiments performed are shown in Figure 5.2. The black line in the main body of Figure 5.2 provides the time sequence of the double potential step and the red line plots the resulting current response. It has been observed that if the fresh ITO electrode is initially biased at +0.40 V and then stepped to −0.20 V, the current transient revealed a typical diffusion-controlled response as evidenced by the linear Q vs $t^{1/2}$ plot shown in the inset. However, the current transient associated with the second, subsequent potential step to −0.80V displayed a prominent minimum within the first 0.25 s of the transient. The amplitude and position in time of this minimum is highly dependent on the value of the second-step potential and became increasingly more intense with more negative overpotential. However, it was never observed in transients where the step potential is positive of −0.50 V. Such behavior seemed highly characteristic of nucleation and growth during electrodeposition on foreign electrode surfaces[7, 37, 38] and further supports the fact that only peak II leads to direct electrodeposition of Au^o. A detailed discussion following up on the nucleation and growth model will be discussed in Chapter 7, of this thesis.

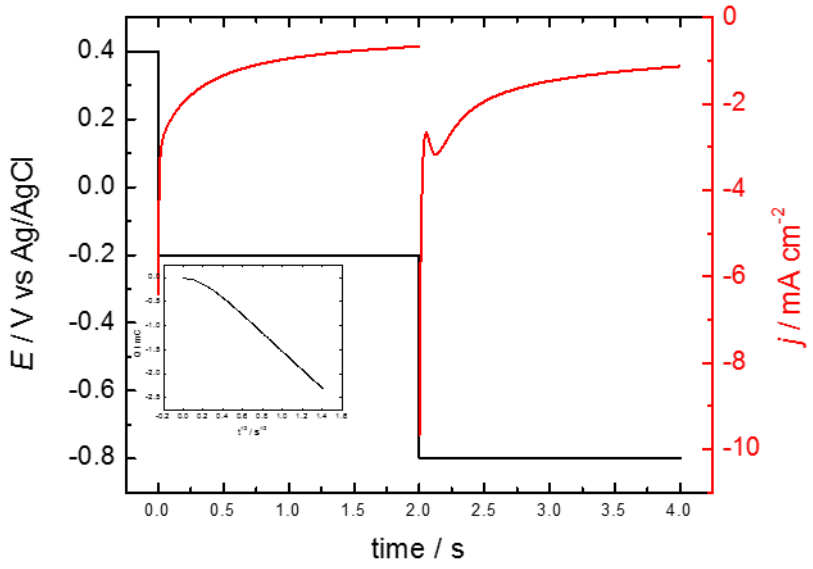

Figure 5.2. The potential step sequence (left axis) and current responses (right axis) for double potential step experiments. The inset shows the integrated current as a function of $t^{1/2}$ for the first potential step.

No metallic gold was expected to form on a fresh ITO working electrode (i.e., one with no residual gold from previous potential cycling) when held at potentials −0.3 V < *E* < −0.1 V, where the disproportionation (Scheme 5.1, reaction 5.3) reaction is kinetically very slow. Evidence of the disproportionation was, however, observed by biasing the electrode at −0.25 V for extended periods (30 min to 2 h). Figure 5.3 shows that roughly half a minute after the electrode potential was scanned through peak I and held at −0.25 V, the distinctive nucleation and growth current minimum appears. Note that the time scale in Figure 5.3 is significantly larger than that shown in Figure 5.2.

This delayed nucleation and growth process was caused by the slow disproportionation of the electrogenerated Au^{I} species and the formation of *Py*-stabilized gold nanoparticles that adsorb on the ITO surface which served as sites for subsequent nucleation and growth kinetics of Au^{0} atoms formed through reactions 2 and 3 of scheme 5.1. As evidenced by SEM images (Figure 5.4a), holding the potential at −0.25 V for extended times led to the presence of gold crystallites on the ITO surface. After passing 75 mC cm^{-2} of charge, two types of structures can clearly be observed

on the ITO surface: individual crystallites and extended aggregates that have a mesh-like appearance.

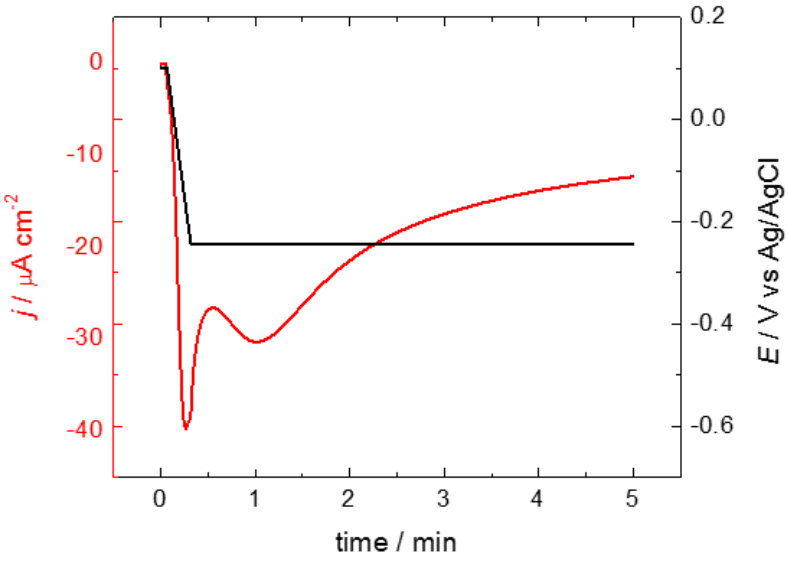

Figure 5.3. The potential (right axis) and current (left axis) transients measured during a potential sweep and hold experiment with a final potential of -0.25V.

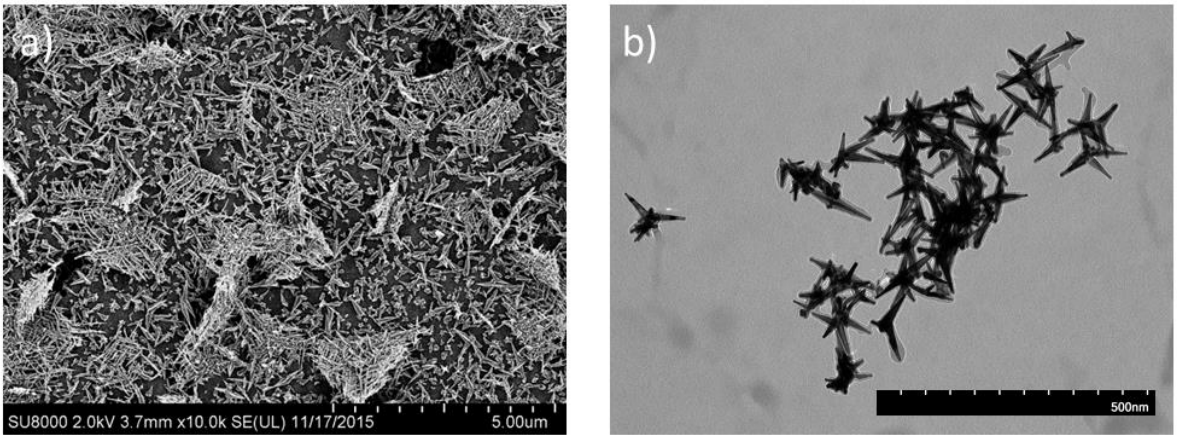

Figure 5.4. (a) SEM image of ITO electrode after depositing gold from 0.25 mM $KAuCl_4$ and 0.1 M MOP in 0.1 M NaCl by applying −0.15 V until the charge passed was 75 mC cm^{-2}. (b)

TEM image of gold nanoparticles formed in aqueous solution by the borohydride reduction of 0.25 mM $KAuCl_4$ in 0.1 M MOP.

The more discrete structures on the ITO surface resulted from Au that deposited directly on the electrode surface, perhaps originating from trace levels of $(Au^{III}Py_{4-x}Cl_x)^{3-x}$ formed as a kinetic competitor to $AuPy_2Cl_q\left(OH\right)_{2-q}^{+}$ in reaction 5.3. The individual structures in the meshes generally had a tripodal shape and were similar to substituted pyridine-stabilized Au nanoparticles formed as dispersions through chemical reduction methods [28, 31] (Figure 5.4b). The large size of the multipods and their high number density in the volume of electrolyte in closest proximity to the working electrode lead to the aggregation and precipitation of the extended networks on the ITO. Unlike the discrete electrodeposited material, the meshes were loosely bound to the ITO and could be removed by gentle sonication in 0.1 M MOP (Figure 5.5).

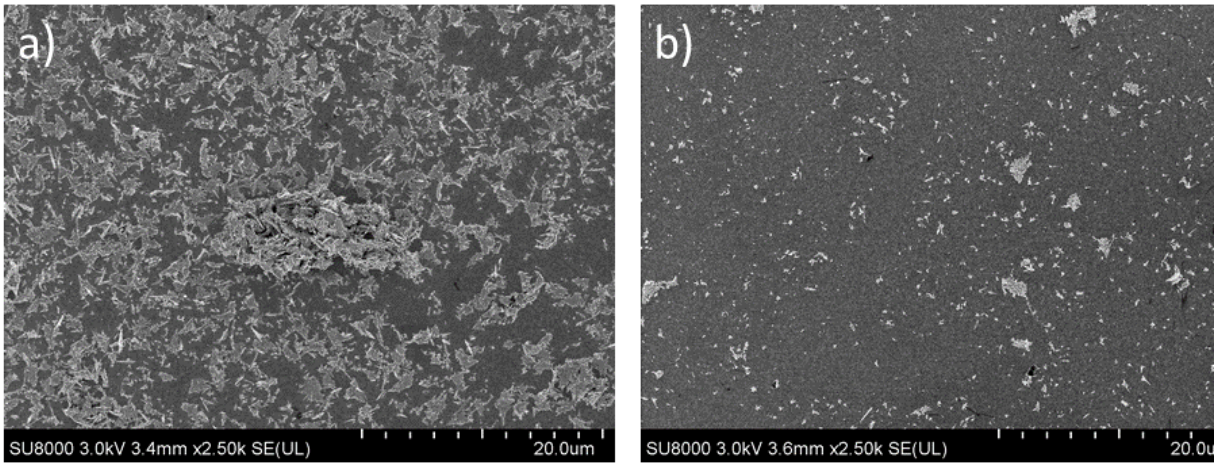

Figure 5.5. (a) SEM images of gold meshes deposited on the ITO surface after application of -0.25 V for ~ 2hrs (a) Before sonication (b) After sonication in 0.1 M MOP.

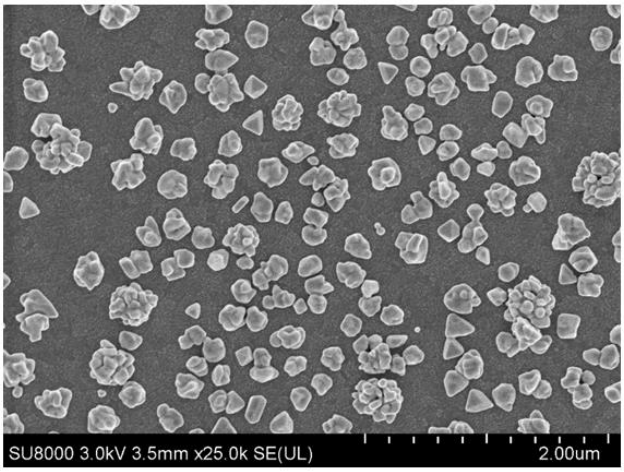

Figure 5.6. SEM image of ITO electrode after depositing gold at −0.20 V and passing charge of 75 mC cm^{-2} from 0.25 mM $KAuCl_4$ in 0.1 M NaCl in the absence of MOP.

The importance of 4-methoxypyridine was further confirmed by electrodepositing 0.25 mM $KAuCl_4$ and 0.1 M NaCl in the absence of the pyridine derivative. Tian *et al.* [20] have shown that pyramidal, spherical, and rod-like structures can all be obtained from such electrolytes by manipulating the deposition potential and the concentration of tetrachloroaurate ions. Figure 5.6 shows that electrodeposition from a *Py*-free solution generates quasi-spherical nanoparticles, although faceting is visible, and some particles are slightly elongated, multipodal, or octahedral in appearance. Figure 5.7 shows nanodaggers obtained in the presence of *Py*.

Plowman *et al*. [16] produced gold nanoplates at low overpotential and gold nanospikes at higher deposition potential by electrochemical reduction of $HAuCl_4$ but noted that the presence of Pb^{2+} ions was critical to the formation of such highly anisotropic shapes. The Pb^{2+} ions were proposed to bind preferentially on Au {110} and Au {100} faces, leading to preferred growth along ⟨111⟩ directions as confirmed by XRD measurements. Previous studies have shown that pyridine derivatives are also preferentially adsorbed on non-Au{111} facets [39] and should lead to relatively accelerated growth in ⟨111⟩ directions. Further detailed discussion on the characterization of the gold nanodaggers are presented in Chapter 6.

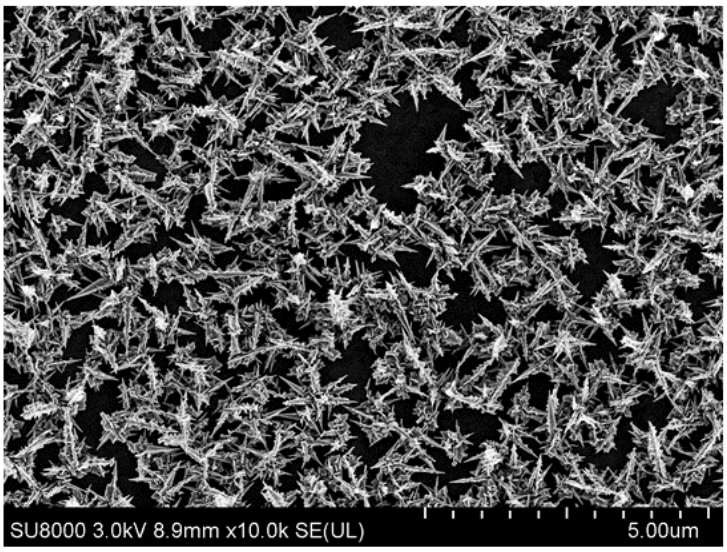

Figure 5.7. SEM images of ITO electrode after depositing gold from 0.25 mM $KAuCl_4$ and 0.1 M MOP in 0.1 M NaCl at -0.43 V with charge passed 75 mC cm^{-2}

5.3.2 Thermodynamics and kinetics of disproportionation

This section is utilized to explain further the aspects of the disproportionation reaction in the proposed reactions of the AuMOP electrochemistry (Scheme 5.1). Mass spectrometry results indicate the formation of $Au^{I}Py_2^+$ as detailed in Chapter 4. This species is formed both through a slow, galvanic reaction at open circuit potential and electrochemically by the application of a potential negative of peak I in the CV shown in Figure 5.1. Au^{I} systems are known to be susceptible to disproportionation reactions. Disproportionation is a redox reaction that results when a species of intermediate oxidation state undergoes both oxidation and reduction. In the terms of the present case of the Au-MOP system, the disproportionation reaction is given by the following equation

$$3AuPy_2^+ + (2-q)OH^- + qCl^- \rightleftarrows 2Au^o + AuPy_2Cl_q(OH)_{2-q}^+ + 4Py \qquad 5.6$$

The disproportionation equilibrium constant, $K_{disp,}$ assuming unit activity for the metallic form of gold for the above reaction is,

$$K_{disp} = \frac{a_{AuPy_2Cl_q(OH)^+_{2-q}}}{a^3_{AuPy_2^+}} \left(\frac{a^4_{Py}}{a^{2-q}_{OH^-} a^q_{Cl^-}} \right) \qquad 5.7$$

And the two half reactions (written in the form of reductions) of the overall disproportionation reaction can be written as,

$$AuPy_2Cl_q(OH)^+_{2-q} + 2e^- \rightleftharpoons AuPy_2^+ + (2-q)OH^- + qCl^- \quad : E_{III/I} \qquad 5.8$$

$$AuPy_2^+ + e^- \rightleftarrows Au^o + 2Py \quad : E_{I/0} \qquad 5.9$$

The accurate determination of the equilibrium constant can be developed by writing the Nernst equation for the above two reactions. Beginning with the known standard reduction potential [40] for $Au^{III} + 2e^- \rightleftarrows Au^I (E^0 = 1.41V)$ and $Au^I + e^- \rightleftarrows Au^o (E^0 = 1.69V)$ with the stability constants for $AuPy_2Cl_q(OH)^+_{2-q}$ and $AuPy_2^+$ defined by $\beta_{III,q}$ and β_I, the Nernst expression can be written as ,

$$E_{III/I} = 1.41V + \frac{RT}{2F} \ln \left[\left(\frac{\beta_I}{\beta_{III,q}} \right) \left(\frac{a_{AuPy_2Cl_q(OH)^+_{2-q}}}{a_{AuPy_2^+} a^{2-q}_{OH^-} a^q_{Cl^-}} \right) \right] \qquad 5.10$$

$$E_{I/0} = 1.69V + \frac{RT}{2F} \ln \left[\left(\frac{1}{\beta_I^2} \right) \left(\frac{a^2_{AuPy_2^+}}{a^4_{Py}} \right) \right] \qquad 5.11$$

By equating the left-hand side of both the equations 5.10 and 5.11 under the assumption that the potential of either the solution or the interface where the reaction occurs is defined by mixed-potential conditions, leads to the relationship between the extent of disproportionation and the two stability constants.

$$\ln K_{disp} = \frac{0.56F}{RT} + \ln \left(\frac{\beta_{III,q}}{\beta_I^3} \right) \qquad 5.12$$

The disproportionation is thermodynamically favoured when the ratio in the right-hand side of Equation 5.12 is greater than ~ 10^{-8}. An analysis of the requirement that $\beta_{III,q}$? β_I reveals that the

standard reduction potential $E_{I/0}$ must be more positive than $E_{III/I}$ in order for the disproportionation to be thermodynamically favoured. It is interesting to note that Eqn 5.12 can be applied also to the chloride and cyanide systems and doing so provides ln K_{disp} values of 19.5 and -114 respectively and explains why $AuCl_2^-$ disproportionates whereas $Au(CN)_2^-$ does not.

It is interesting to compare the thermodynamic requirements for disproportionation to the experimentally measured voltammetry. As described above, the electrochemical analysis indicates that nucleation and growth of Au^0 on the ITO surface only occurs on the time scale of a voltammogram at potentials negative of the second peak (~0.40 V). This indicates that the $Au^{III/I}$ redox event is observed at potentials more positive than the $Au^{I/0}$ redox process. This seems contradictory to the thermodynamic requirements needed to explain the observed disproportionation. This apparent discrepancy can be explained by considering the electron transfer kinetics.

The process of disproportionation of Au^I is known to be very slow in the absence of metallic gold, whereas, the presence of Au^0, catalyses the disproportionation reaction. [36] Metallic gold, Au^0, in either the form of electrodeposited crystallites on the ITO or dispersed nanoparticles would provide active surfaces to accelerate the disproportionation. In order to reconcile the experimental voltammetry with the thermodynamics of disproportionation explained above, the heterogeneous electron transfer rates between the ITO working electrode and both the gold complexes, $AuPy_2Cl_q\left(OH\right)_{2-q}^{+}$ and $Au^IPy_2^+$, must be very slow. I hereby propose that the order of the observed voltammetric reduction peaks in the AuMOP system (Figure 5.1) are reversed from that expect from thermodynamic considerations due to the need for much higher overpotentials to nucleate gold and slow electron transfer kinetics. This relates to the idea that the gold species near the electrode is not governed by the Nernst equation until very large overpotentials are established at the electrode/solution interface. It is well known that large overpotentials are required to nucleate and grow a metal phase on a foreign substrate with poor wettability,[41] and this requirement of an extra driving force beyond that predicted by the Nernst equation is partially responsible for the inversion of the two redox processes. Thus, it implies that the two reduction peaks ($2e^-$ and $1e^-$) observed in the voltammetry are much more negative of the true formal potentials. Evidence supporting the contention that the electron transfer kinetics are very slow

comes from the absence of an oxidation peak (red trace in Figure 5.1) , i.e. the re-oxidation of $Au^{I}Py_2^{+}$ to reform $AuPy_2Cl_q\left(OH\right)_{2-q}^{+}$, in the voltammetry. The oxidation of metallic gold (black trace in Figure 5.1) is likely caused by the initial dissolution of Au to form $AuCl_4^-$ (aq) which then undergoes rapid ligand exchange with solution phase pyridine species.

5.3.3 Detailed study on the electrochemical response of the Au-MOP system

To recap the voltammogram described in Figure 5.1, the addition of 0.25mM $KAuCl_4$ to an aqueous solution of 0.1 M NaCl and 0.1 M MOP showed two irreversible voltammetric peaks on the cathodic scan of a potential sweep from the open-circuit potential. As soon as the gold salt is introduced, there occurs a ligand exchange reaction between the chloride and the MOP in the first 5-10 mins to form $AuPy_2Cl_q\left(OH\right)_{2-q}^{+}$. This has been established in our study on the kinetics of Au^{III} ligand exchange in Chapter 4. The electrochemistry and the relevant reactions occurring on the time scale of the voltammogram thus starts off with $AuPy_2Cl_q\left(OH\right)_{2-q}^{+}$ as summarized in Scheme 5.2.

According to Scheme 5.2, the black line corresponds to the first reduction peak in the voltammogram which is the 2-electron reduction to form $AuPy_2^{+}$. Due to very slow heterogeneous electron transfer kinetics and the need for a large overpotential to nucleate gold on ITO, this species becomes a metastable species rather than immediately reducing to Au^0. As the potential is swept further negative, the heterogenous electron transfer rate constant and the overpotential become large enough to nucleate and grow the electrodeposited Au^0 on defect sites of the conductive working electrode, ITO. The heterogeneous one-electron reduction of $AuPy_2^{+}$ is shown by the red line in the scheme.

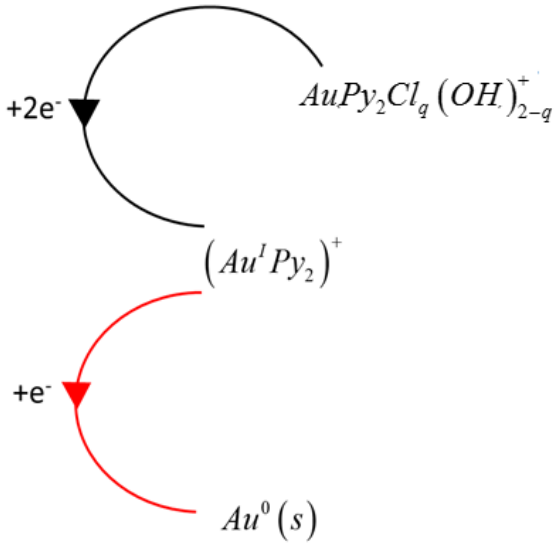

Scheme 5.2. Au-MOP electrochemistry: reaction occurring during first peak in CV (black line), reactions occurring during second peak in CV (red line).

In an effort to better understand the redox chemistry associated with Peak I, the potential applied to an ITO electrode was held at -0.15V after scanning from the OCP. This hold potential corresponds to an intermediate value between the two reduction peaks and the initial expectation was that it would result in no deposited Au as the peak is attributed to the exchange of two electrons involving soluble Au^{III} and Au^{I} species. When this intermediate potential was applied for approximately two hours, the corresponding SEM image (Figure 5.4a) revealed a surface composed of strongly adhered individual metallic crystallites and loosely adhered extended aggregates that have a mesh-like appearance. Scheme 5.3, attempts to explain this observation.

The black line corresponds to the first reduction peak in the voltammogram which is the 2-electron reduction to form $AuPy_2^+$ and the potential hold occurs between the first and second reduction peaks. In the beginning of the potential hold experiment, as the potential is not sufficiently large enough to reduce the Au^{I} species to Au^0, the disproportionation reaction would be kinetically slow in the absence of metallic gold. But as the time progresses, the disproportionation reaction slowly occurs and generates Au^0. The Au^0 remains dispersed in the solution near the electrode in the form of nanoparticles stabilized by the adsorption of excess MOP. This explains the formation of mesh-

like structures as the density of these particles eventually leads to aggregation and sedimentation on the electrode surface.

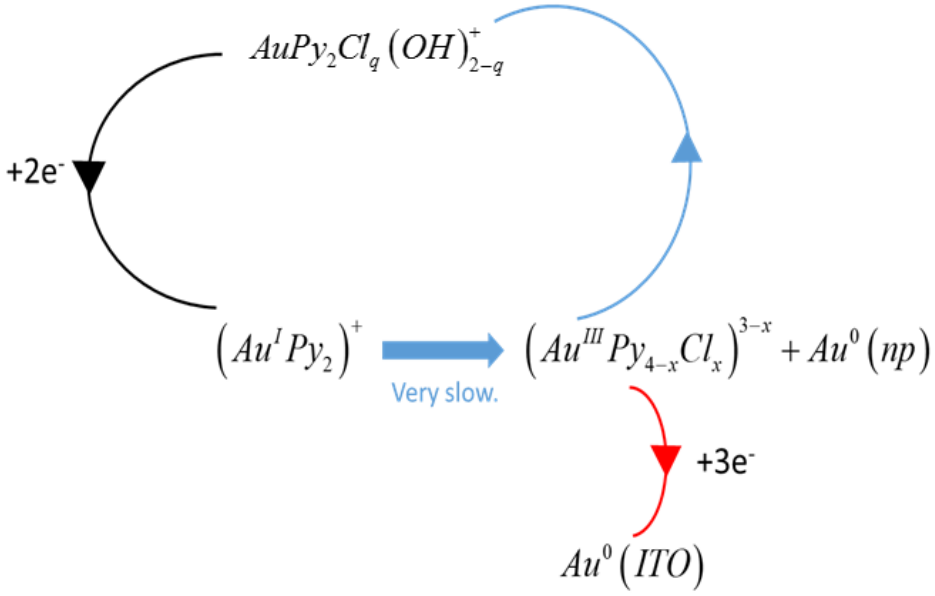

Scheme 5.3. Au-MOP electrochemistry – potential hold experiment: reaction occurring during first peak in CV (black line), disproportionation and solution phase reaction (blue line), Au^{III} reduction to Au^0 as hold time progresses (red line).

As explained in the earlier scheme, the Au^{III} formed from the disproportionation can either be recycled to $AuPy_2Cl_q(OH)^+_{2-q}$ (blue path) depending on the rate of ligand exchange or directly reduced on the ITO surface. Subsequently, the rate of disproportionation begins to accelerate as the amount of metallic Au (either dispersed as nanoparticles or as deposited crystallites on the ITO) increases. Thus, the formation of individual metallic crystallites occurs.

5.3.4 Electrochemistry of Au-MOP complex in different supporting electrolyte

As the chloride ion is known to strongly adsorb on gold, it was conceivable that some of the shape directed growth might be caused by the presence of chloride ions in solution. In an effort to determine if the halide ion was playing a critical role, analogous experiments were performed using NaF as the supporting electrolyte. Unlike, chloride, the fluoride ion does not specifically

adsorb on Au [42]. A representative cyclic voltammetric scan of the Au-MOP complex in NaF as the electrolyte is shown in Figure 5.8a.

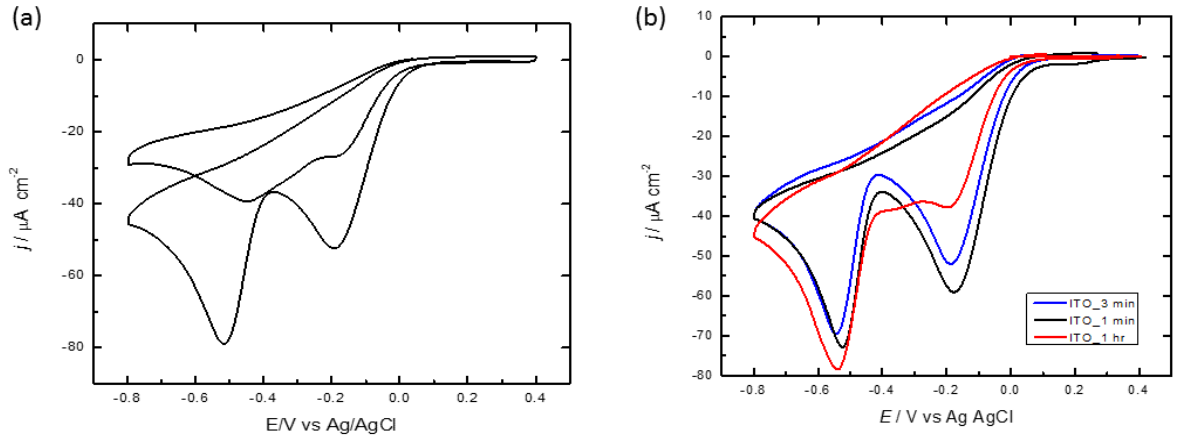

Figure 5.8. Cyclic voltammograms (20 mV/s) of ITO electrodes in 0.25 mM $KAuCl_4$ aqueous solution of 0.1 M NaF and 0.1 M 4-methoxypyridine (a) first and second CV's (b) at different ageing times of the electrolyte.

The cyclic voltammetry yields two irreversible cathodic peaks similar to when NaCl was used as the electrolyte and it is noted that the reductive electrochemistry is largely identical if the NaCl supporting electrolyte is replaced by NaF. However, if the electrolyte and the *Py* are allowed to react for extended periods of time, new shoulders are seen in the voltammetry as shown in Figure 5.8b which is most likely due to the formation of different Au(III) complexes of F^-,Cl^- , and *Py*.

The role of the chloride ions in the supporting electrolyte was investigated further with microscopic imaging to see if the shape-directing properties were attributable to preferential halide adsorption on Au{111} facets.[4] The SEM images in Figure 5.9 show Au electrodeposits produced from 0.1 M MOP using 0.1 M NaF as the supporting electrolyte. These images revealed the same nano dagger structures as formed in the presence of chloride under equivalent conditions, thus indicating that the *Py* molecules and not the halide ions are shape-directing agents. This was readily explained by the fact that the deposition is conducted at potentials below the potential of zero charge.

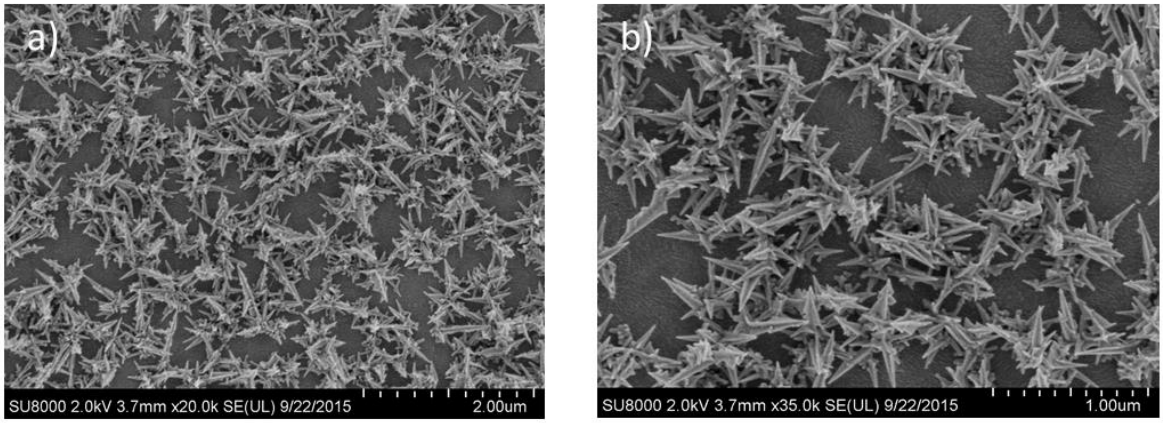

Figure 5.9. SEM images of (a) MOP-stabilized gold nanoparticles in NaF as the supporting electrolyte (b) magnified image of (a)

It is known that pyridine derivatives can displace adsorbed chloride ions on negatively charged Au.[43] For further clarification on the Au-MOP system, a bromide containing electrolyte was also investigated. Figure 5.10 represents the cyclic voltammogram when 0.25 mM $KAuBr_4$ aqueous solution was added to 0.1 M KBr and 0.01 M 4-methoxypyridine solutions. The voltammogram was similar to the chloride system and showed similar characteristics over time as well. This further establishes that the halides has no role in shape-directing the nanostructures.

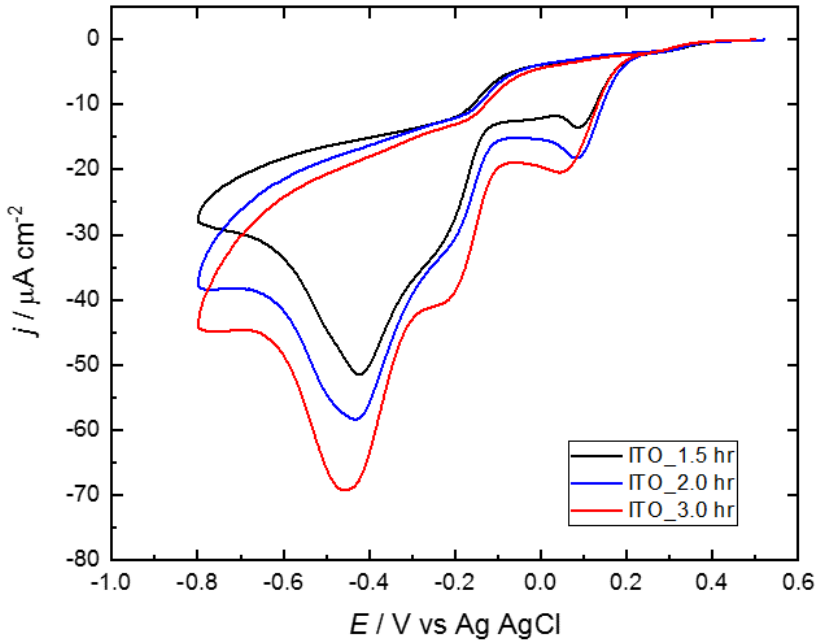

Figure 5.10. Cyclic voltammograms (20 mV/s) of ITO electrodes in 0.25 mM $KAuBr_4$ aqueous solution of 0.1 M NaBr and 0.01 M 4-methoxypyridine.

5.4 Conclusion

The electrochemical analysis presented in this chapter shows that Au^{III} complexes of 4-methoxypyridine undergo a two-step reduction process. The intermediate species in the reduction process, 4-methoxypyridine-Au^{I} complexes, can either be electrodeposited directly on the electrode surface at further negative potentials or undergo a disproportionation reaction to form Au nanoparticle dispersions. A comprehensive discussion on the thermodynamic and kinetic aspect of the disproportionation reaction provided some insight on the proposed reaction mechanism. Sustained polarization of the electrochemical interface at potentials corresponding to the formation of Au^{I} leads to the physical deposition of Au nanoparticle meshes on the ITO surface through a disproportionation reaction. On the other hand, electrochemical deposition provides highly anisotropic nanodaggers with very large aspect ratios. Characterization of the nanodaggers revealing a preferential Au (111) orientation are discussed in detail in the next chapter along with their potential applications.

It is interesting to mention the differences between *Py*-directed growth of nanocrystals formed by chemical and electrochemical reduction. Dispersions of nanoparticles formed by borohydride reduction primarily form tripods emanating from a distinct core, whereas electrochemical reduction produces very elongated crystals, and the arms are more irregular in both length and distribution about the cores. The differences are likely caused by several key factors relating to the rates of nucleation and mass transport. Whereas potentiostatic deposition proceeds under a fixed thermodynamic driving force, the formation of nanoparticle dispersions leads to a rapid consumption of borohydride and results in a weakening of the reductive driving force. This likely causes particle growth to occur primarily through Au(I) disproportionation. The limited investigation provided herein has shown a dependency on the resulting nanoparticle structure on the applied deposition potential. It is likely that these structures can be further manipulated by more complex potential perturbation profiles during electrochemical deposition.

5.5 References

1. Hyun, M., et al., *Simple Electrodeposition of Dendritic Au Rods from Sulfite-Based Au(I) Electrolytes with High Electrocatalytic and SERS Activities. Electroanalysis,* 2011. **23**(9): p. 2030-2035.

2. Seo, B., S. Choi, and J. Kim, *Simple Electrochemical Deposition of Au Nanoplates from Au(I) Cyanide Complexes and Their Electrocatalytic Activities*. ACS Appl. Mater. Interfaces, 2011. **3**(2): p. 441-446.

3. Abdelsalam, M.E., et al., *Electrochemical SERS at a structured gold surface*. Electrochem. Commun., 2005. **7**(7): p. 740-744.

4. Guo, S., L. Wang, and E. Wang, *Templateless, surfactantless, simple electrochemical route to rapid synthesis of diameter-controlled 3D flowerlike gold microstructure with "clean" surface*. Chem. Commun. (Cambridge, U. K.), 2007(30): p. 3163-3165.

5. Mahajan, S., et al., *Reproducible SERRS from structured gold surfaces*. Phys. Chem. Chem. Phys., 2007. **9**(45): p. 6016-6020.

6. Huang, S., et al., *Electrochemical Synthesis of Gold Nanocrystals and Their 1D and 2D Organization*. J. Phys. Chem. B, 2005. **109**(42): p. 19823-19830.

7. Komsiyska, L. and G. Staikov, *Electrocrystallization of Au nanoparticles on glassy carbon from $HClO_4$ solution containing $[AuCl_4]$*. Electrochim. Acta, 2008. **54**(2): p. 168-172.

8. Rahman, M.R., T. Okajima, and T. Ohsaka, *Fabrication of Au(111) nanoparticle-like electrode through a seed-mediated growth.* Chem. Commun. (Cambridge, U. K.), 2010. **46**(28): p. 5172-5174.

9. Sakai, N., et al., *Electrodeposition of gold nanoparticles on ITO: Control of morphology and plasmon resonance-based absorption and scattering*. J. Electroanal. Chem., 2009. **628**(1-2): p. 7-15.

10. Bu, Y. and S.-W. Lee, *Flower-like gold nanostructures electrodeposited on indium tin oxide (ITO) glass as a SERS-active substrate for sensing dopamine*. Microchim. Acta, 2015. **182**(7-8): p. 1313-1321.

11. El-Said, W.A., et al., *Detection of effect of chemotherapeutic agents to cancer cells on gold nanoflower patterned substrate using surface-enhanced Raman scattering and cyclic voltammetry*. Biosens Bioelectron, 2010. **26**(4): p. 1486-92.

12. Wang, J., et al., *An Invisible Template Method toward Gold Regular Arrays of Nanoflowers by Electrodeposition*. Langmuir, 2013. **29**(11): p. 3512-3517.

13. Ma, Y. and L.-Y.L. Yung, *Gold Nanoplate-Based 3D Hierarchical Microparticles: A Single Particle with High Surface-Enhanced Raman Scattering Enhancement*. Langmuir, 2016. **32**(31): p. 7854-7859.

14. McMillan, B.G., et al., *Reflectance and SERS from an ordered array of gold nanorods*. Electrochim. Acta, 2007. **53**(3): p. 1157-1163.

15. Blanch, A.J., M. Doeblinger, and J. Rodriguez-Fernandez, *Simple and Rapid High-Yield Synthesis and Size Sorting of Multibranched Hollow Gold Nanoparticles with Highly Tunable NIR Plasmon Resonances*. Small, 2015. **11**(35): p. 4550-4559.

16. Plowman, B., et al., *Gold nanospikes formed through a simple electrochemical route with high electrocatalytic and surface enhanced Raman scattering activity*. Chem. Commun. (Cambridge, U. K.), 2009(33): p. 5039-5041.

17. Lv, Z.-Y., et al., *Shaped-controlled electrosynthesis of gold nanodendrites for highly selective and sensitive SERS detection of formaldehyde*. Sens. Actuators, B, 2014. **201**: p. 92-99.

18. Mei, L.-P., et al., *Simple electrodeposition of hierarchical gold-platinum nanothorns and their applications in electrocatalysis and SERS*. Electrochim. Acta, 2015. **160**: p. 235-243.

19. Liu, H., et al., *Size-selective electrodeposition of meso-scale metal particles: a general method*. Electrochim. Acta, 2001. **47**(5): p. 671-677.

20. Tian, Y., et al., *Shape-Controlled Electrodeposition of Gold Nanostructures*. J. Phys. Chem. B, 2006. **110**(46): p. 23478-23481.

21. Mann, S., *The chemistry of form*. Angew. Chem., Int. Ed., 2000. **39**(19): p. 3392-3406.

22. Ben-Jacob, E. and P. Garik, *The formation of patterns in non-equilibrium growth*. Nature, 1990. **343**(6258): p. 523-530.

23. Lopez, C.M. and K.-S. Choi, *Electrochemical Synthesis of Dendritic Zinc Films Composed of Systematically Varying Motif Crystals*. Langmuir, 2006. **22**(25): p. 10625-10629.

24. Matsushita, M., et al., *Fractal structures of zinc metal leaves grown by electrodeposition*. Phys. Rev. Lett., 1984. **53**(3): p. 286-9.

25. Sawada, Y., A. Dougherty, and J.P. Gollub, *Dendritic and fractal patterns in electrolytic metal deposits*. Phys. Rev. Lett., 1986. **56**(12): p. 1260-3.

26. Lingane, J.J., *Standard potentials of half-reactions involving +1 and +3 gold in chloride medium. Equilibrium constant of the reaction* $AuCl_4^- + 2Au + 2Cl^- = 3AuCl_2$. J. Electroanal. Chem. (1959-1966), 1962. **4**: p. 332-42.

27. Koelle, U. and A. Laguna, *Electrochemistry of Au-complexes*. Inorg. Chim. Acta, 1999. **290**(1): p. 44-50.

28. Danger, B.R., et al., *Electrochemical Studies of Capping Agent Adsorption Provide Insight into the Formation of Anisotropic Gold Nanocrystals*. ACS Nano, 2012. **6**(12): p. 11018-11026.

29. Quirk, A., B. Unni, and I.J. Burgess, *Surface Enhanced Infrared Studies of 4-Methoxypyridine Adsorption on Gold Film Electrodes*. Langmuir, 2016. **32**(9): p. 2184-2191.

30. Rosendahl, S.M., et al., *Surface Enhanced Infrared Absorption Spectroscopy Studies of DMAP Adsorption on Gold Surfaces*. Langmuir, 2009. **25**(4): p. 2241-2247.

31. Unni, B., S. Simon, and I.J. Burgess, *Electrochemical investigations of 4-methoxypyridine adsorption on Au(111) predict its suitability for stabilizing Au nanoparticles.* Langmuir, 2015. **31**(36): p. 9882-9888.

32. Zeng, J., et al., *AuI: an alternative and potentially better precursor than AuIII for the synthesis of Au nanostructures*. J. Mater. Chem., 2010. **20**(12): p. 2290-2301.

33. Eisenmann, E.T., *Kinetics of the electrochemical reduction of dicyanoaurate*. J. Electrochem. Soc., 1978. **125**(5): p. 717-23.

34. Harrison, J.A. and J. Thompson, *Reduction of gold cyanide complexes*. J. Electroanal. Chem. Interfacial Electrochem., 1972. **40**(1): p. 113-20.

35. Sawaguchi, T., et al., *Electrochemical Scanning Tunneling Microscopy and Ultrahigh-Vacuum Investigation of Gold Cyanide Adlayers on Au(111) Formed in Aqueous Solution*. J. Phys. Chem., 1995. **99**(38): p. 14149-55.

36. Gammons, C.H., Y. Yu, and A.E. Williams-Jones, *The disproportionation of gold(I) chloride complexes at 25 to 200°C.* Geochim. Cosmochim. Acta, 1997. **61**(10): p. 1971-1983.

37. Gunawardena, G., et al., *Electrochemical nucleation. Part I. General considerations*. J. Electroanal. Chem. Interfacial Electrochem., 1982. **138**(2): p. 225-39.

38. Scharifker, B. and G. Hill, *Theoretical and experimental studies of multiple nucleation*. Electrochim. Acta, 1983. **28**(7): p. 879-89.

39. Vivek, J.P. and I.J. Burgess, *Crystallographic dependence of 4-dimethylaminopyridine electrosorption on gold*. Electrochim. Acta, 2013. **88**: p. 688-696.

40. Firdaus, M., et al., *Green synthesis of silver nanoparticles using Carica Papaya fruit extract under sunlight irradiation and their colorimetric detection of mercury ions*. Journal of Physics: Conference Series, 2017. **817**: p. 012029.

41. Guo, L. and P.C. Searson, *On the influence of the nucleation overpotential on island growth in electrodeposition*. Electrochimica Acta, 2010. **55**(13): p. 4086-4091.

42. Clavilier, J. and V.H. Nguyen, *Structure of the double layer on gold electrodes.* J. Electroanal. Chem. Interfacial Electrochem., 1973. **41**(2): p. 193-9.

43. Vivek, J.P. and I.J. Burgess, *Insight into Chloride Induced Aggregation of DMAP-Monolayer Protected Gold Nanoparticles Using the Thermodynamics of Ideally Polarized Electrodes*. J. Phys. Chem. C, 2008. **112**(8): p. 2872-2880.

CHAPTER 6

FORMATION OF ANISOTROPIC GOLD NANOSTRUCTURES FROM AU-MOP ELECTROLYTES

6.1 Manuscript Author Contributions

The current Chapter is part of the manuscript published in *J. Phys. Chem. C* 2016, 120, 45, 26150–26158 which was authored by four members of the Burgess group. Even though the majority of the research work was performed by the first author (the thesis writer), the contributions from the co-authors are substantial. First, and foremost, to be mentioned is the role of Ian. J. Burgess. He not only supervised my research work but also had the chief role in writing the manuscript. The second author of the manuscript, Theophilus I. Olumorin, was a summer student who worked under my direct supervision. His contribution to the research work was the 'Electrodeposition of the gold nanostructures at different conditions' as described by Figure 6.2-6.5 in the current Chapter. Finally, the third author of the manuscript, Bao Guo, was a post doctoral fellow who helped me perform Raman experiments and wrote the 'Calculation of FT-Raman SERS enhancement factors' described in this chapter. All the co-authors have been notified about the plan to incorporate their sections into my thesis and their permissions would be available upon request.

6.2 Introduction

Anisotropic gold nanostructures are of great interest due to the strong correlation between shape and surface plasmon resonances. Understanding and optimizing the morphology of the gold nanostructures allows better tuning of their optical responses. The concept of forming

nanostructured metal directly on a solid substrate, such as ITO, can be technically valuable as any additional preparation step on the metal-substrate connection can be avoided. The formation of nanocrystal films electrodeposited on conductive electrodes presents several advantages compared to the methods that produce nanoparticle dispersions. One of the most significant advantages offered is more precise control of the reductive conditions required to nucleate and grow nanostructures and which in principle, can be used to generate homogeneous and densely populated metal nanoparticle films. Such films serve as excellent platforms for surface-enhanced Raman scattering (SERS) sensors for biomedical and related applications [1-3]. Unlike nanoparticle dispersions, electrodeposited nanoparticles can either be formed in the absence of shape-directing/stabilizing surfactants [4] or readily subjected to conditions that remove unwanted chemical modifiers *post facto* without perturbing the metal structures. This represents a major advantage for SERS applications as the presence of surfactants can negatively affect detection limits if they block the adsorption of analytes or produce strong SERS interferences.

This Chapter describes the characterization of gold nanostructures formed from Au-MOP electrolytes using electron microscopy imaging and other conventional techniques. Efforts have been made to justify the optical extinction behaviour of the anisotropic gold nanostructures formed. Preliminary measurements provided in this chapter illustrate the excellent suitability of these interfaces for FT-Raman applications utilizing near-IR excitation sources.

6.3 Characterization of gold electrodeposits

To determine the size and morphology of the gold nanostructures deposited on ITO glass, the electrodeposited layers were characterised primarily by scanning electron microscopy (SEM). The crystallographic faceting of the electrodeposited gold nanostructures was assessed using lead underpotential deposition (Pb UPD) and XRD techniques. The experimental method details of these surface-sensitive techniques and potentiostatic procedures are discussed in Chapter 2. This section involves the characterization and analysis of the electrodeposited structures.

6.3.1 SEM imaging

Electron microscopy, such as scanning electron microscopy (SEM), with spatial resolution approaching the sub-nanometer region has been useful in determining the size and structural morphology of the gold electrodeposits. The ITO surface, after the potentiostatic electrodeposition of gold nanostructures by biasing a fresh ITO sample at -0.43V (peak II) until the integrated current provided 75mC cm^{-2} of charge as detailed in Chapter 5, was seen to be decorated with a dense layer of anisotropic crystallites as shown in Figure 6.1(a). The multipodal nature of the electrodeposits is revealed in the higher magnification image of the same surface as shown in Figure 6.1(b).

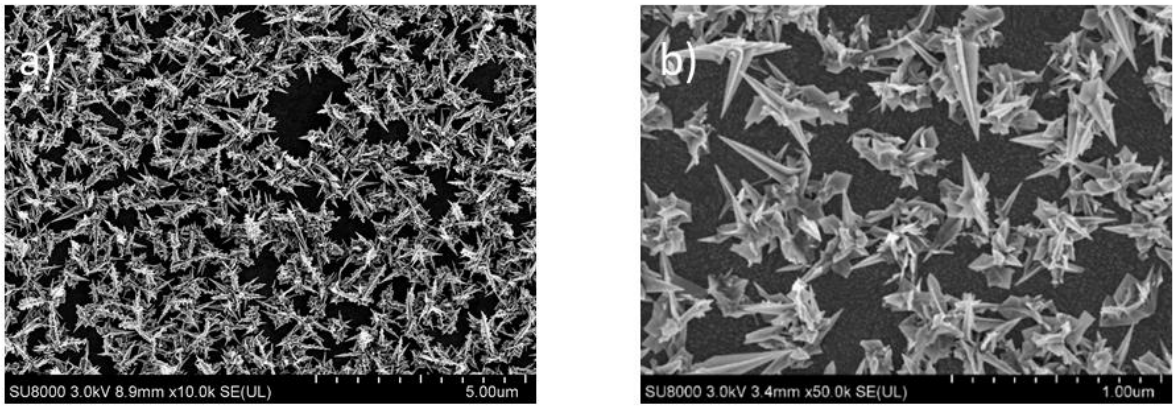

Figure 6.1. SEM images of ITO electrode after depositing gold from 0.25mM $KAuCl_4$ and 0.1M MOP in 0.1M NaCl (a) Deposition potential was -0.43V and charge passed was 75 mC cm^{-2} (b) magnified image of a.

Multipodal gold nanoparticles have been previously reported from the chemical reduction of Au^{III} precursor salts. Selective adsorption of the stabilizing ligand, as well as a high concentration buildup of monomer atoms, are believed to have played key roles in forming such structures.[5-13]. In these previous reports, the crystallites exhibited low aspect ratio branches with the longest arms being ~50 nm, as reported by Danger *et al.* [7] for the borohydride reduction of $AuCl_4^-$ in the presence of 4-(dimethylamino)pyridine. Figure 6.1 revealed that electrochemical deposition in the presence of 4-methoxypyridine stabilizer resulted in arms that can extend several hundred nanometers The SEM images clearly show the distinctively tapered and dagger-like appearances

of the branches. Apart from the high aspect ratio branches with the arms extending several hundred nanometers, smaller arms were also observed. The smaller arms and the centres of the crystallites have a plate-like appearance similar to those produced by Seo *et al*.[14] from the electrochemical deposition of Au $(CN)_2^-$.

The effect of deposition charge and potential as well as the ratio of Au^{III} to 4-methoxypyridine was studied, and representative SEM images are provided in Figures 6.2-6.5.

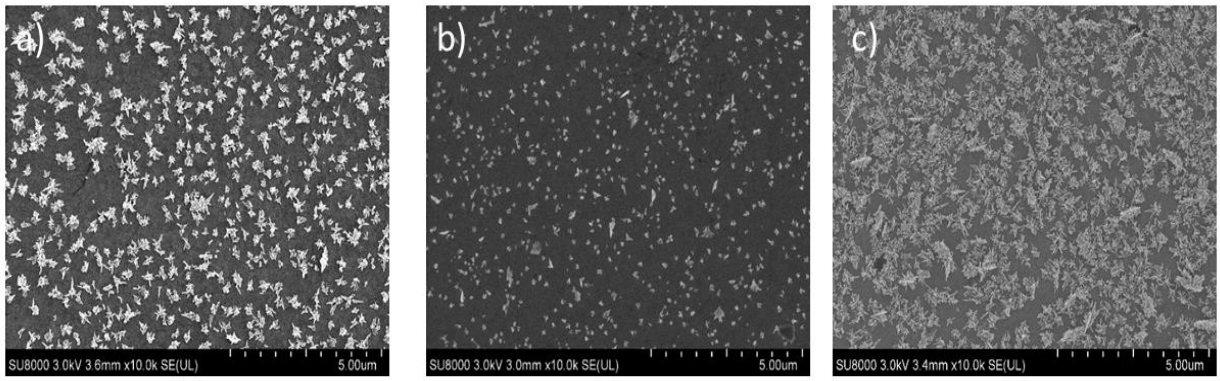

Figure 6.2. The effect of change in concentration of Au (III) precursor on the electrochemical deposition of Au nanostructures. SEM images of Au nanostructures from 0.1 M MOP and a) 0.25 mM $KAuCl_4$ (1:400) b) 0.4 mM $KAuCl_4$ (1:250) c) 1 mM $KAuCl_4$ (1:100) at -0.425V for 25 mC cm^{-2} in 0.1 M NaCl as the supporting electrolyte.

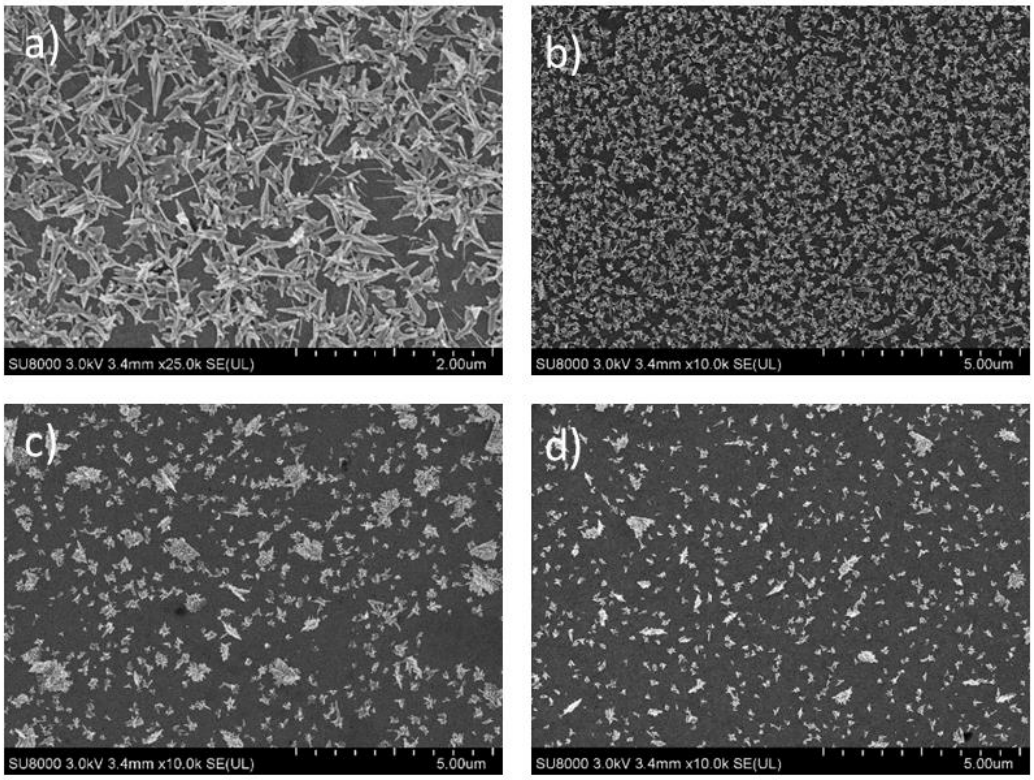

Figure 6.3. The effect of change in concentration of the stabilizing agent 4-methoxypyridine (MOP) on the electrochemical deposition of Au nanostructures. SEM images of Au nanostructures (25.0 k and 10.0 k magnification) from 0.25 mM $KAuCl_4$ and a) 0.1 M MOP (1:400) b) 0.062 M MOP (1:250) c) 0.025M MOP (1:100) d) 0.01 M MOP (1:40) at -0.42V for 25 mC cm^{-2} in 0.1 M NaCl as the supporting electrolyte.

Figure 6.2 represents the effect of change in concentration of the Au(III) precursor and Figure 6.3 depicts the effect of change in concentration of the stabilizing agent 4-methoxypyridine (MOP) on the electrochemical deposition of Au nanostructures The appearance of the electrodeposited gold was seen largely insensitive to the ratio of $KAuCl_4$/MOP, but lower deposition charge leads to smaller crystals with shorter aspect ratio arms. Figure 6.4 represents the SEM images of gold nanostructures from 0.1 M MOP and 0.25 mM $KAuCl_4$ in 0.1 M NaCl deposited at -0.42 V (peak II) with various charge densities and Figure 6.5 represents the SEM images of gold nanostructures at different deposition potentials. It was observed that the deposition at potentials more negative than −0.50 V decreased the aspect ratio of the arms.

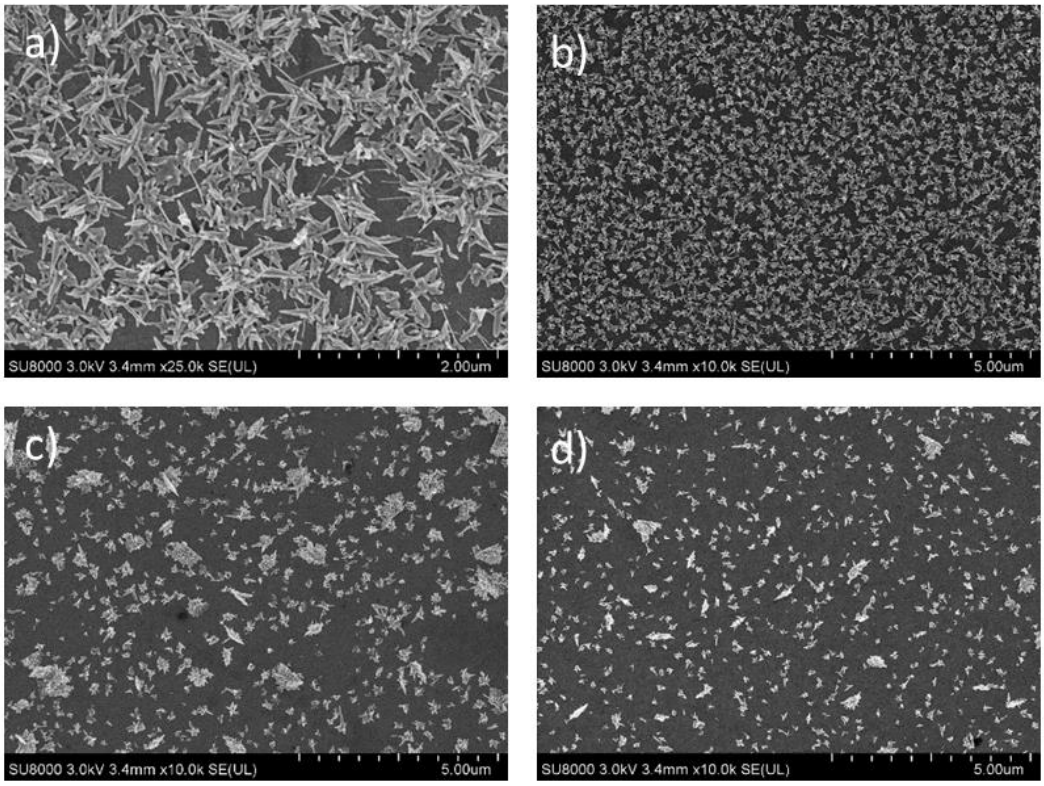

Figure 6.4. SEM images of Au nanostructures (25.0 k and 10.0 k magnification) from 0.1 M MOP and 0.25 mM $KAuCl_4$ in 0.1 M NaCl deposited at -0.42 V with various charge densities a) 75 mC cm^{-2} b) 50 mC cm^{-2} c) 25 mC cm^{-2} d) 11 mC cm^{-2}.

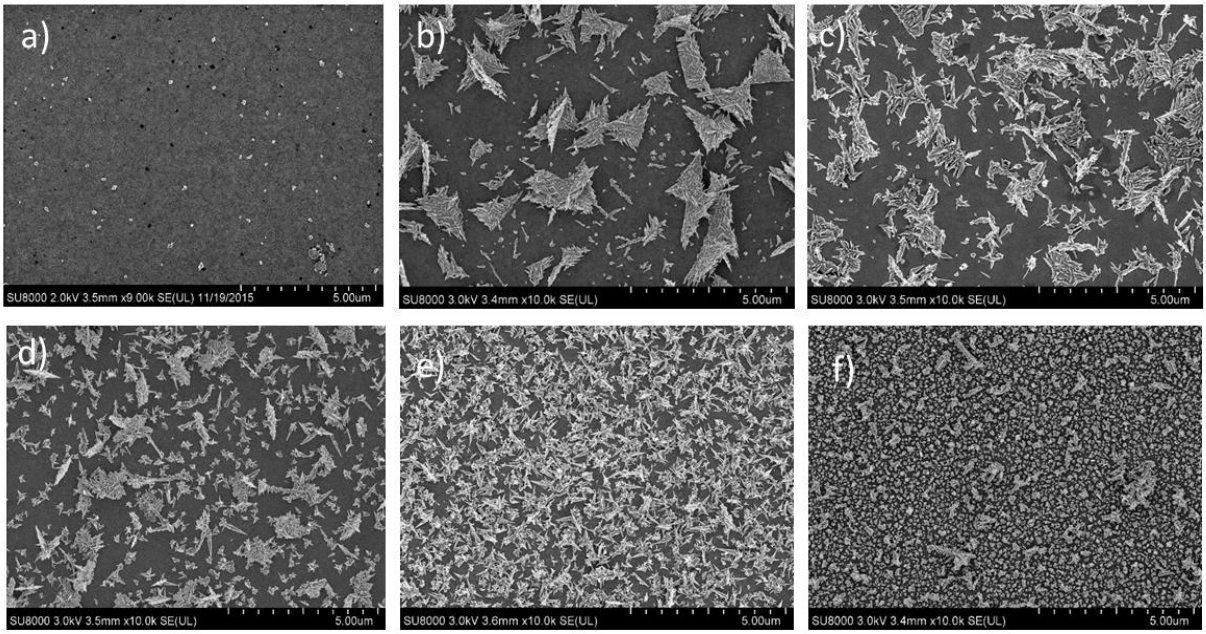

Figure 6.5. SEM images of Au nanostructures from 0.1M MOP and 0.25 mM $KAuCl_4$ in 0.1 M NaCl deposited at different potentials a) 0 V b) -0.13 V c) -0.22 V d) -0.36 V e) -0.42 V f) -0.70 V.

6.3.2 XRD analysis

In structural characterization**,** the X-ray diffraction (XRD) technique has been used to compare the results obtained from electrodeposited gold nanodaggers to polycrystalline gold. The XRD studies were performed for the gold deposited from *Py*-containing electrolyte, and the corresponding XRD pattern is shown in Figure 6.6. The XRD pattern indicated an intense peak at $2\theta = 44.6$, representing a preferential growth in the (111) direction. The XRD intensity ratio of the peaks {111}/{200} is 5:1 and for {111}/{220} is 2.5:1, which strongly suggests that the crystals are grown preferentially such that {111} orientations are dominant. This XRD pattern is typical of pure Au nanocrystals.[15, 16].

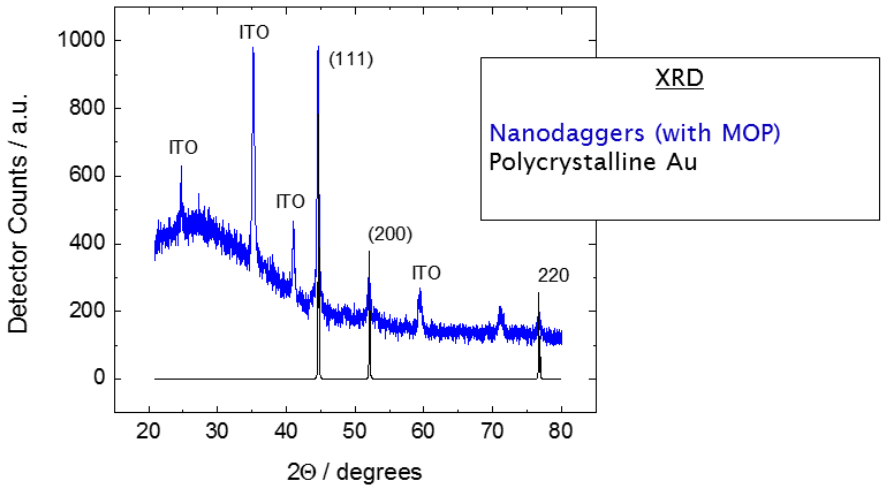

Figure 6.6. XRD on polycrystalline Au bead and Au deposited on ITO from 0.25 mM $KAuCl_4$ in 0.1 M NaCl in the presence of 0.1 M MOP.

6.3.3 Pb UPD analysis

The stripping voltammetry of the underpotential deposited lead was performed in 0.1M KOH and 1.0 mM $Pb(NO_3)_2$ electrolyte. Figure 6.7 shows the stripping (dissolution) of UPD Pd for a gold polycrystalline bead formed by melting and slow cooling of a gold wire (I) and gold electrodeposited on ITO from 0.1 M NaCl with (II) and without (III) the presence of 0.1 M MOP.

The stripping potentials of UPD Pb were diagnostic of both the crystallographic orientation [17, 18] and size [19] of Au facets and the gold bead provided characteristic peaks for narrow (−540 mV) and wide (−529 mV) {111} domains. Weaker signals were seen for {100} facets at −575 mV and −483 mV, and the broad feature centered at −400 mV was assigned to {110}. Currents below −600 mV do not appear on single crystals and have been attributed to steps and kink sites. [20] The stripping results for the nano dagger deposits were dominated by a narrow peak at −534 mV and a broader peak at −390 mV. No evidence of {100} features was apparent, and the dissolution signals below −600 mV were very weak. In comparison to the polycrystalline Au bead, gold deposited from *Py*-containing electrolyte was dominated by preferential {111} faceting. In the absence of *Py*, the Pb stripping results provided a relatively weaker and broader {111} peak. A small peak at −468 mV, which was close to the potential assigned to {100} facets, stronger signals

below −600 mV, and a much broader {110} current that was shifted toward positive potentials were all present. The latter feature is presumed to indicate the presence of wide terraces of high energy crystallographic surfaces.

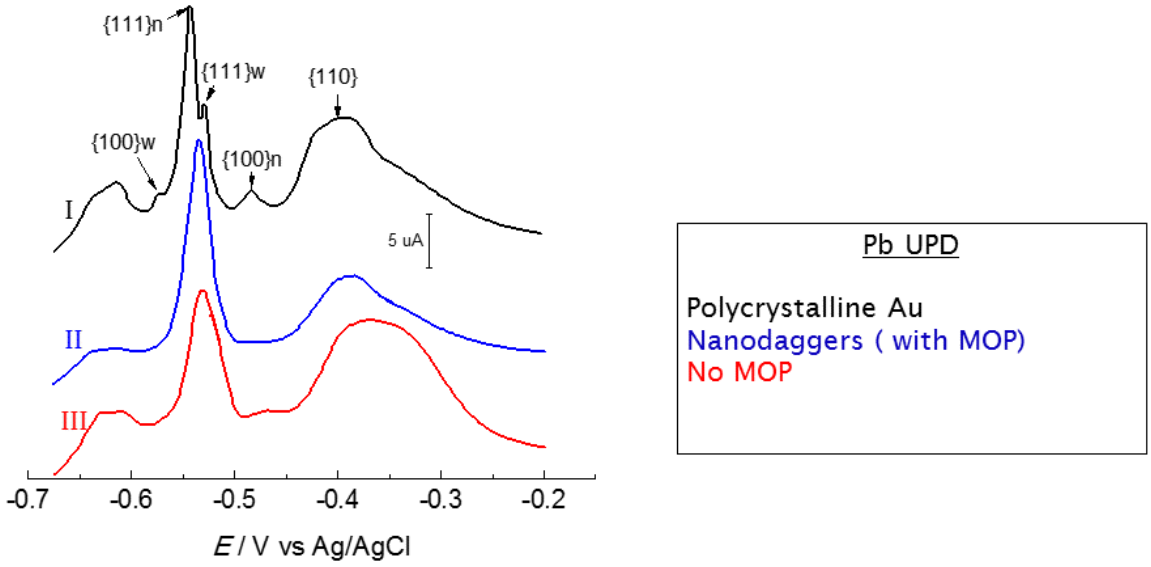

Figure 6.7. Stripping voltammetry of underpotential deposited Pb on (I) polycrystalline Au bead and Au deposited on ITO from 0.25 mM $KAuCl_4$ in 0.1 M NaCl in the presence (II) and absence (III) of 0.1 M MOP. Stripping electrolyte was 0.1 M KOH and 1 mM $Pb(NO_3)_2$. Scan rate: 20 mV/s.

6.4 Application

6.4.1 Surface-enhanced Raman Spectroscopy

The optical properties of gold nanoparticle films are dependent on particle size, shape, and interparticle separations.[21] The interaction of metal nanoparticles with light generates collective oscillations of free electrons (localized surface plasmon resonances, LSPR) that produce intense electric field enhancements at the metal surface and gives rise to a dominant SERS mechanism.[22] Further details on the theory of FT-Raman spectroscopy has been discussed in Chapter 2. Discrete gold nanoparticles typically exhibit LSPR in the visible region of the electromagnetic spectrum and maximum SERS signal enhancement is achieved when the excitation source is nearly resonant with the LSPR of the substrate.[23] Raman scattering intensity scales directly with the source

intensity, but inversely with the fourth power of the wavelength, and large SERS enhancements are typically seen using visible laser lines. However, despite their inherently lower Raman signals, samples with near IR (NIR) plasmonic resonances offer distinct advantages, including operation in the optical transmission window of tissue, the absence of deleterious fluorescent background signals, and much greater compatibility with samples otherwise prone to photobleaching.[24] The optical extinction of electrodeposited gold nanodaggers is shown in the Vis−NIR spectrum provided in Figure 6.8a.

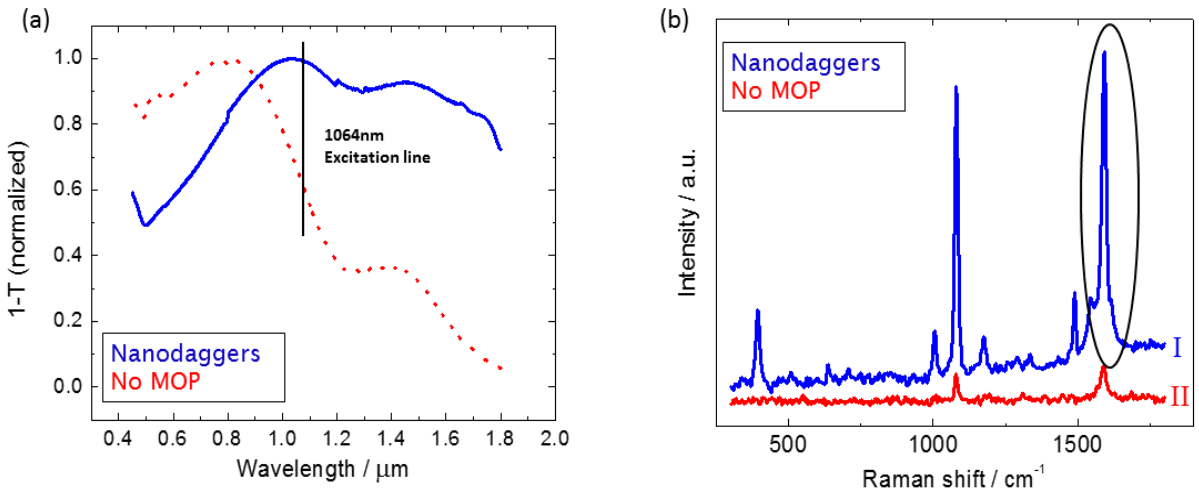

Figure 6.8. (a) Visible−near IR optical properties of gold deposited from 0.25 mM $KAuCl_4$ in 0.1 M NaCl in the presence (nano daggers, blue line) and absence (nanoparticles, red dotted line) of 0.1 M MOP. (b) FT-Raman SERS for monolayers of 4-ATP on nanodaggers (I, blue line) and nanoparticles (II, red line) using 1064 nm excitation. 400 mW laser power and 512 coadded scans. Deposited charge passed was 75 mC cm^{-2} for both samples.

Short wavelengths were dominated by absorption from the ITO support, but strong optical extinction was evident above 500 nm in the form of a broad peak centered at ~1000 nm that extends beyond 1800 nm. The broadness of the optical response indicates that many different LSPR modes are produced from the various length scales of the nanodaggers. However, the peak position was resonant with the 1064 nm Nd:YAG line found in commercial FT-Raman instruments, making these samples particularly attractive for potential SERS applications. In comparison, Figure 6.8a shows that the extinction from an equal amount of gold electrodeposited

in the absence of *Py* has a maximum at considerably shorter wavelengths, although it should be noted that it also exhibits a notable loss of transmitted light intensity in the NIR. A comparison of the NIR SERS of the two types of samples using 1064 nm excitation from a Nd:YAG laser is shown in Figure 6.8b. The performance of these samples as SERS-active substrates was evaluated using a self-assembled monolayer of 4-ATP as the probe molecule. Whereas the nanoparticle film only provides two weak signals, the nanodaggers provide several strong Raman signals superimposed on a smooth and nearly flat baseline. Discrete molecular signatures originating from the a1 vibrations of the C−C (1591 cm^{-1}) and the C−S (1080 cm^{-1}) bonds in the 4-ATP ring modes[25] as well as a medium intensity band at 394 cm^{-1} attributed to a C−S bending mode[26] dominate the spectrum. The enhancement factor for the 1591 cm^{-1} band was determined to be 2×10^6 for the nanodaggers, which was an order of magnitude larger than the enhancement factor for the nanoparticle film. Based on assignments reported by Osawa *et al*.,[25] the remaining weaker bands at 1005, 1175, and 1487 cm^{-1} all arose from a1 modes, and there is no evidence of peaks at 1142, 1389, or 1435 cm^{-1} as reported in the FT-Raman SERS of 4-ATP on Ag nanoparticle films.[26] These bands were initially assigned to the b2 modes of 4-ATP [25], but subsequently, it has been shown that they are likely caused by the catalytic oxidation of 4-ATP to 4,4′-dimercaptoazobenzene.[27, 28] Although, there has been some previous work [29], that has shown that the appearance of these modes is facet-dependent and particularly strong for Au{110} relative to {111} facets,[30] it is likely that their absence in Figure 6.8 is caused by the use of low energy laser excitation, which is insufficient to facilitate the oxidation process.

6.4.1.1 Calculation of FT-Raman SERS enhancement factors

The enhancement factor (EF) was defined as,

$$\mathrm{EF} = \frac{I_{\mathrm{SERS}} / N_{\mathrm{ads}}}{I_{\mathrm{bulk}} / N_{\mathrm{bulk}}} \qquad 6.1$$

The 1591 cm^{-1} band was used for the calculation of EF values. I_{SERS} stands for the intensity of this band in the SERS spectrum of 4-ATP and I_{bulk} for that of the bulk solid sample. From Figure 6.8b, I_{SERS} for nanodaggers and nanoparticles were measured to be 0.0153 and 0.0015, respectively. The FT-Raman spectrum of solid 4-ATP sample under the same measurement conditions is shown in

Figure 6.9, and I_{bulk} was measured to be 0.0054. N_{ads} is the number of 4-ATP molecules adsorbed on the SERS substrate, and N_{bulk} is the number of bulk molecules illuminated by the laser to obtain the corresponding FT-SERS and ordinary Raman spectra, respectively.

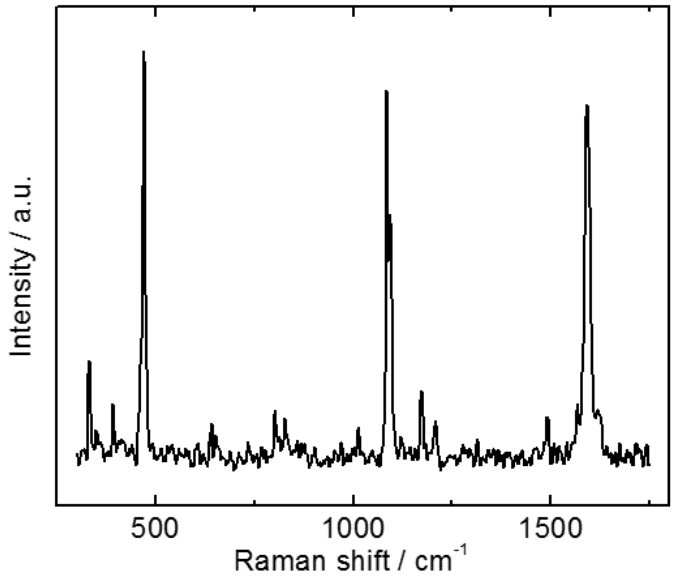

Figure 6.9. FT-Raman spectrum of bulk 4-ATP sample using 1064 nm excitation, 400 mW laser power and 512 scans

According to the proposed method of Orendorff et al [31], N_{ads} on nanoparticle modified substrates can be calculated as:

$$N_{ads} = N_d A_{laser} A_N / \sigma \qquad 6.2$$

where N_d is the number density of the nanoparticles, A_{laser} is the area of the focal spot of laser, A_N is the nanoparticle footprint area, and σ is the surface area occupied by a single adsorbed 4-ATP molecule. Due to the complicated structure of our nanodaggers, it is difficult to obtain N_d and A_N value separately. By slightly modifying Orendorff's equation, N_{ads} can be expressed as,

$$N_{ads} = A_D A_{laser} / \sigma \qquad 6.3$$

where A_D is the area density of the nanostructure in terms of its footprint on the ITO substrate. With the help of scientific image analysis software "Fiji ImageJ" [32], A_D (36.8%) can be obtained from the SEM image in Figure 6.1b. According to the report by Gole [33] σ can be adopted as ~0.2 nm^2/ molecule.

N_{bulk} can be expressed as ,

$$N_{\text{bulk}} = \frac{\rho A_{\text{laser}} D_{\text{p}}}{M / n} \qquad 6.4$$

where ρ is the density of the solid 4-ATP (1.18 g/cm^3), M the molecular weight (125.19 g/mol) and n the Avogadro constant. The penetration depth (D_p) of the focused laser beam is wavelength dependent, and a value of ~180 μm is used.

The EF of the nanodaggers for the 1591 cm^{-1} band can be calculated to be as large as 1.57×10^6 at 1064 nm excitation. Correspondingly, the EF value of gold nanoparticles was also calculated via the similar way. A_D (30.2%) of gold nanoparticles on the ITO substrate can be obtained from the SEM image in Figure 6c. Briefly, the EF value for 1591 cm^{-1} band was calculated to be about 1.8×10^5, which was 10 times lower than that on the nanodaggers. Thus, the enhancement factor was calculated successfully for the nanoparticle film.

6.5 Conclusions

In summary, the formation of anisotropic gold nanostructures from AuMOP solutions have been analysed in this chapter. The potentiostatic electrodeposition of Au (III) salts in the presence of MOP has resulted in the formation of multipodal gold nanostructures. The length scale of the deposited dagger-like shaped gold nanostructures is seen to be dependent on the deposition potential and deposited charge, and arms extending several hundred nanometers have been reported. Characterization of the nanodaggers has revealed a preferential Au{111} orientation. Optical characterisations show extinction extending well into the near-infra red region, which is attributed to the localised surface plasmonic resonances. Near-IR Raman sensing applications have been demonstrated using FT-Raman with 1064 excitation. The optical properties of the

nanodaggers make them well suited for near-IR (FT-Raman) SERS, as demonstrated by the 2×10^6 enhancement factor measured for a monolayer of 4-ATP.

6.6 References

1. Abdelsalam, M.E., et al., *Electrochemical SERS at a structured gold surface. Electrochem. Commun.*, 2005. 7(7): p. 740-744.

2. Mahajan, S., et al., *Reproducible SERRS from structured gold surfaces.* Phys. Chem. Chem. Phys., 2007. 9(45): p. 6016-6020.

3. Yao, J.L., et al., *A complementary study of surface-enhanced Raman scattering and metal nanorod arrays.* Pure Appl. Chem., 2000. 72(1-2): p. 221-228.

4. Guo, S., L. Wang, and E. Wang, *Templateless, surfactantless, simple electrochemical route to rapid synthesis of diameter-controlled 3D flowerlike gold microstructure with "clean" surface.* Chem. Commun. (Cambridge, U. K.), 2007(30): p. 3163-3165.

5. Bakr, O.M., B.H. Wunsch, and F. Stellacci, *High-Yield Synthesis of Multi-Branched Urchin-Like Gold Nanoparticles*. Chem. Mater., 2006. 18(14): p. 3297-3301.

6. Chen, S., et al., *Monopod, bipod, tripod, and tetrapod gold nanocrystals*. J. Am. Chem. Soc., 2003. 125(52): p. 16186-16187.

7. Danger, B.R., et al., *Electrochemical Studies of Capping Agent Adsorption Provide Insight into the Formation of Anisotropic Gold Nanocrystals.* ACS Nano, 2012. 6(12): p. 11018-11026.

8. Nehl, C.L., H. Liao, and J.H. Hafner, *Optical Properties of Star-Shaped Gold Nanoparticles.* Nano Lett., 2006. 6(4): p. 683-688.

9. Sau, T.K. and C.J. Murphy, *Room temperature, high-yield synthesis of multiple shapes of gold nanoparticles in aqueous solution.* J. Am. Chem. Soc., 2004. 126(28): p. 8648-8649.

10. Sau, T.K. and A.L. Rogach, *Nonspherical Noble Metal Nanoparticles: colloid-Chemical Synthesis and Morphology Control*. Adv. Mater. (Weinheim, Ger.), 2010. 22(16): p. 1781-1804.

11. Sau, T.K., et al., *One-Step High-Yield Aqueous Synthesis of Size-Tunable Multispiked Gold Nanoparticles*. Small, 2011. 7(15): p. 2188-2194.

12. Unni, B., S. Simon, and I.J. Burgess, *Electrochemical investigations of 4-methoxypyridine adsorption on Au(111) predict its suitability for stabilizing Au nanoparticles.* Langmuir, 2015. 31(36): p. 9882-9888.

13. Yuan, H., et al., *Shape and SPR Evolution of Thorny Gold Nanoparticles Promoted by Silver Ions.* Chem. Mater., 2007. 19(7): p. 1592-1600.

14. Seo, B., S. Choi, and J. Kim, *Simple Electrochemical Deposition of Au Nanoplates from Au(I) Cyanide Complexes and Their Electrocatalytic Activities.* ACS Appl. Mater. Interfaces, 2011. 3(2): p. 441-446.

15. Sneha, K., et al., *Yucca-derived synthesis of gold nanomaterial and their catalytic potential.* Nanoscale research letters, 2014. 9: p. 627.

16. Wu, C.-M., et al., *Surface characterization and thermomechanical behavior of nanostructured-gold layer for biomedical applications*. J. Alloys Compd., 2019. 782: p. 1114-1120.

17. Hernandez, J., et al., *Characterization of the Surface Structure of Gold Nanoparticles and Nanorods Using Structure Sensitive Reactions.* J. Phys. Chem. B, 2005. 109(26): p. 12651-12654.

18. Sanchez-Sanchez, C.M., et al., *Scanning electrochemical microscopy for studying electrocatalysis on shape-controlled gold nanoparticles and nanorods.* Electrochim. Acta, 2010. 55(27): p. 8252-8257.

19. Hernandez, J., et al., *In situ surface characterization and oxygen reduction reaction on shape-controlled gold nanoparticles.* J. Nanosci. Nanotechnol., 2009. 9(4): p. 2256-2273.

20. Hernandez, J., J. Solla-Gullon, and E. Herrero, *Gold nanoparticles synthesized in a water-in-oil microemulsion: electrochemical characterization and effect of the surface structure on the oxygen reduction reaction*. J. Electroanal. Chem., 2004. 574(1): p. 185-196.

21. Le Ru, E.C. and P.G. Etchegoin, *Chapter 7 - Metallic colloids and other SERS substrates, in Principles of Surface-Enhanced Raman Spectroscopy*, E.C. Le Ru and P.G. Etchegoin, Editors. 2009, Elsevier: Amsterdam. p. 367-413.

22. Guerrini, L. and D. Graham, *Molecularly-mediated assemblies of plasmonic nanoparticles for Surface-Enhanced Raman Spectroscopy applications.* Chem. Soc. Rev., 2012. 41(21): p. 7085-7107.

23. McFarland, A.D., et al., *Wavelength-Scanned Surface-Enhanced Raman Excitation Spectroscopy.* J. Phys. Chem. B, 2005. 109(22): p. 11279-11285.

24. Edwards, H.G., *Fourier Transform Raman Instrumentation, in Encyclopedia of Analytical Chemistry.* John Wiley & Sons, Ltd, 2006. p. 1-24.

25. Osawa, M., et al., *Charge transfer resonance Raman process in surface-enhanced Raman scattering from p-aminothiophenol adsorbed on silver: Herzberg-Teller contribution.* J. Phys. Chem., 1994. 98(48): p. 12702-7.

26. Zheng, J., et al., *Comparison of the surface properties of the assembled silver nanoparticle electrode and roughened silver electrode.* J. Phys. Chem. B, 2002. 106(5): p. 1019-1023.

27. Huang, Y.-F., et al., *When the signal is not from the original molecule to be detected: chemical transformation of para-aminothiophenol on Ag during the SERS measurement.* J. Am. Chem. Soc., 2010. 132(27): p. 9244-9246.

28. Sun, M., et al., *The pH-Controlled Plasmon-Assisted Surface Photocatalysis Reaction of 4-Aminothiophenol to p,p'-Dimercaptoazobenzene on Au, Ag, and Cu Colloids.* J. Phys. Chem. C, 2011. 115(19): p. 9629-9636.

29. Hu, X., et al., *Surface-Enhanced Raman Scattering of 4-Aminothiophenol Self-Assembled Monolayers in Sandwich Structure with Nanoparticle Shape Dependence: Off-Surface Plasmon Resonance Condition.* J. Phys. Chem. C, 2007. 111(19): p. 6962-6969.

30. Nikoobakht, B., J. Wang, and M.A. El-Sayed, *Surface-enhanced Raman scattering of molecules adsorbed on gold nanorods: off-surface plasmon resonance condition.* Chem. Phys. Lett., 2002. 366(1,2): p. 17-23.

31. Orendorff, C.J., et al., *Surface-Enhanced Raman Spectroscopy of Self-Assembled Monolayers: Sandwich Architecture and Nanoparticle Shape Dependence.* Analytical Chemistry, 2005. 77(10): p. 3261-3266.

32. Schindelin, J., et al., *Fiji: an open-source platform for biological-image analysis.* Nat. Methods, 2012. 9(7_part1): p. 676-682.

33. Gole, A., S.R. Sainkar, and M. Sastry, *Electrostatically Controlled Organization of Carboxylic Acid Derivatized Colloidal Silver Particles on Amine-Terminated Self-Assembled Monolayers.* Chem. Mater., 2000. 12(5): p. 1234-1239.

CHAPTER 7

NUCLEATION AND GROWTH STUDY OF 4-METHOXYPYRIDINE STABILISED GOLD NANOSTRUCTURES

7.1 Introduction to nucleation and growth in electrochemistry

The controlled fabrication of anisotropic metal nanostructures has advantages in numerous fields, including plasmonics and catalysis. This controlled morphology can be achieved with precision by studying the nucleation and growth studies of nanostructures. The importance of 4-methoxy pyridine as the shape-directing ligand was confirmed in the earlier chapters. The gold nanostructures electrodeposited in the presence of 4-methoxypyridine were shown to have dagger-like structures and revealed a rather larger polydispersity in nano dagger aspect ratio and overall length whereas in the absence of 4-methoxypyridine, they were qausi-spherical in nature. A detailed understanding of the initial stages of the growth of metal nanostructures formed in the presence of a growth-director such as 4-methoxypyridine may provide additional means to control the overall morphology of the deposited film. A more thorough understanding of the initial stages of deposition and subsequent growth could be used to decrease the degree of polydispersity. Furthermore, controlling the density of the nucleation sites that eventually grow to be nanodaggers would be highly beneficial in controlling the optical responses of the resulting films. This Chapter describes, a systematic study on the electrochemical deposition of Au-MOP under potentiostatic conditions to further understand the deposition mechanism on conductive ITO substrates. Chronoamperometry techniques, as well as morphological microscopy examinations, are presented and compared to the theoretical predictions for nucleation and growth models.

Electrochemistry provides a means by which noble metals can be deposited on conductive surfaces from an electrolyte. Electrodeposition allows the surface morphology, and thickness to be controlled by finely adjusting the deposition parameters. To better understand the basics of electrodeposition and the relationship between the applied potential and morphology, it is important to recognize the nucleation and growth mechanism associated with each process. Nucleation is the first step in the generation of a new phase and is a stochastic process whereby natural fluctuations in particle density leads to the formation of a collection of monomers that overcome the energy threshold needed to form a new phase.[1] Two types of classical nucleation exist - homogenous and heterogeneous nucleation. Homogenous nucleation occurs when the nuclei forms uniformly throughout the parent phase instantaneously whereas heterogeneous nucleation forms at structural inhomogeneities.[2] One of the biggest advantages of electrochemical nucleation [3] (Figure 7.1) over other means to drive nucleation is the ability to precisely control the electric potential which is the driving force for the phase change.

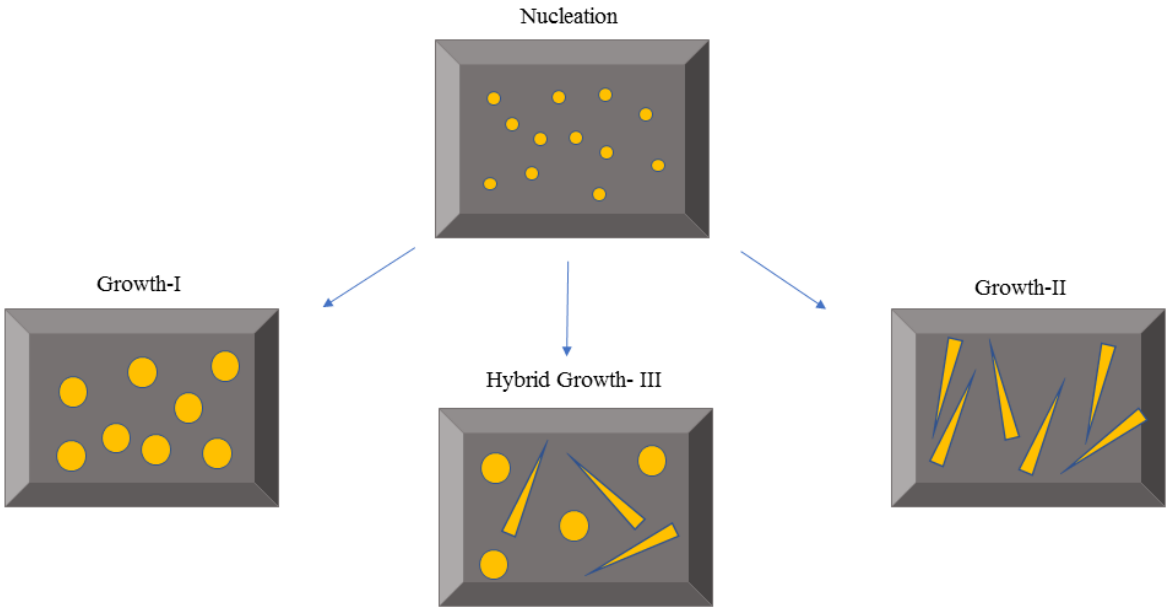

Figure 7.1. Schematic representation of nucleation and growth of nuclei/seeds on an electrode surface.

Growth I and II as shown in Figure 7.1 represents similar shapes obtained when the applied electric potential is precisely controlled whereas hybrid growth is a mixture of two shapes.

Experimentally, there are two means of studying electrochemical nucleation and growth: using potentiostatic conditions or galvanostatic conditions. In the galvanostatic method, the rate of nucleation and growth is indirectly controlled by application of a constant current and the potential required to sustain that rate of reaction is measured as a function of time. In a potentiostatic method, a controlled overpotential is rapidly stepped from a potential where nucleation is thermodynamically impossible to a new potential where a nucleated phase is thermodynamically favoured. In potentiostatic experiments the dependent variable is the current flowing through the interface which provides information on the kinetics of the nucleation and subsequent growth processes. The observed current provides an exact measure of the combined rate of nucleation and growth of the formation of crystallites through various current-potential-time relationships. Thus, by studying the different current transients and comparing them to existing nucleation-growth models, the mechanism of the formation of a new phase can be often deduced.

The formation of a metallic phase from the electrochemical reduction of soluble metal ions is often modeled in terms of the nucleation and growth behavior extensively developed by Scharifker and co-workers.[4] This model describes the mass transport controlled potentiostatic current transients associated with three-dimensional nucleation and growth. According to the model, nucleation occurs at specific surface sites and the number density of these sites is controlled by the applied potential. When a very rapid potential step from an inert potential to a sufficiently large overpotential occurs, the surface sites become active for nucleation and growth. The initial nucleation and subsequent growth in either the size and/or the number of nuclei leads to an increase in the electroactive area. The diffusion-controlled growth of existing nuclei is initially hemispherical in nature but eventually transitions to planar diffusion as the diffusion zones around each nucleus begin to overlap (Figure 7.2).[5]

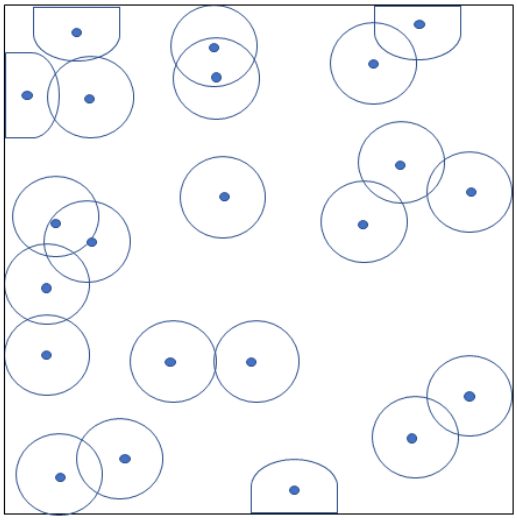

Figure 7.2. Adapted from Scharifker, B. and G. Hill.[5] Schematic plan view of hemispherical nuclei distributed randomly on the electrode surface with the surrounding circles representing their diffusion zones.

The combination of the increased electroactive area from new and growing nuclei, combined with the transition in mass transport conditions, leads to a characteristic maximum in the absolute value of the current transient and is a key diagnostic of nucleation and growth behavior.

In electrodeposition and growth models, the electrode surface is assumed to consist of a limiting number of active sites per unit area, N_o, of sufficiently high enough energy to act as nucleation centres. A sufficient driving force to increase the value of N_o is provided by large overpotentials. However, under potentiostatic conditions, it is not necessary that all active sites immediately convert to *growth* centres and the number density of the latter, N, is, in general, a function of time. The rate of conversion of active sites into growth centres must account for excluded surface areas created by overlapping diffusion zones. This can be modelled by assuming that the time dependent number of un-nucleated sites, n, is described by a first order rate process and a characteristic steady-state nucleation rate constant (per site), A.

$$\frac{dn}{dt} = -An \qquad 7.1$$

Solving Equation 7.1 with the boundary condition that $n = N_o$ at t =0, provides. $n = N_o e^{-At}$. Note that because of the existence of exclusion zones, $n \neq (N_o - N)$. Scharifker and Mostany used Poisson statistics to derive the following expression for the current density transient for nucleation and growth under this model.[5]

$$I(t) = zFc\left(\frac{D}{\pi t}\right)^{1/2}\left\{1-\exp\left[-N_o g\left(t-\frac{\left(1-e^{-At}\right)}{A}\right)\right]\right\} \quad 7.2$$

where *z*, *F*, *c*, and *D* respectively are the valency of the ions undergoing electron transfer with the electrode, the Faraday constant, the concentration of the reactive species diffusing from the bulk of solution and the diffusion coefficient of these species. The parameter *g* depends on the molar volume, V_m, of the metal phase being formed,

$$g = \pi D\left(8\pi c V_m\right)^{1/2} \quad 7.3$$

As described above, nucleation and growth current transients are characterized by a current maximum and it becomes convenient to rewrite Equation 7.2 using a reduced temporal variable (t/t_m) where t_m is the time in the current transient corresponding to the observed maximum. Using the substitutions

$$a = zFc\left(\frac{D}{\pi}\right)^{1/2} \quad 7.4$$

$$b = N_o g \quad 7.5$$

$$x = bt_m \quad 7.6$$

and,

$$\alpha = b/A \quad 7.7$$

Equation 7.1 can be re-written as

$$I = \frac{a}{t^{1/2}}\left\{1-\exp\left[-x\frac{t}{t_m}+\alpha\left[1-\exp\left(-\frac{x}{\alpha}\frac{t}{t_m}\right)\right]\right]\right\} \qquad 7.8$$

The current maximum occurs when $(t/t_m) = 1$, thus defining the maximum current

$$I_m = \frac{a}{t_m^{1/2}}\left\{1-\exp\left[-x+\alpha\left[1-\exp\left(-\frac{x}{\alpha}\right)\right]\right]\right\} \qquad 7.9$$

Finally, a "universal" equation can be obtained by dividing the current transient by the equation for the current maximum,

$$\left(\frac{I}{I_m}\right)^2 = \left(\frac{t_m}{t}\right)\left\{\frac{1-\exp\left[-x\frac{t}{t_m}+\alpha\left[1-\exp\left(-\frac{x}{\alpha}\frac{t}{t_m}\right)\right]\right]}{1-\exp\left[-x+\alpha\left[1-\exp\left(-\frac{x}{\alpha}\right)\right]\right]}\right\}^2 \qquad 7.10$$

Equation 7.10 leads to two limiting forms of nucleation and growth, first described by Scharifker and Hills.[4] In the case of instantaneous nucleation, all growing centres are initiated at the very earliest stages of the potential step. The number of growing nuclei remains constant during the growth stages and hence the age of all nuclei is the same. This equates to very high values of the nucleation rate constant, A, such that equation 7.8 simplifies to

$$I_{inst} = zFc\left(\frac{D}{\pi t}\right)^{1/2}\left\{1-\exp\left[-N_o g t\right]\right\} \qquad 7.11$$

The position of the current maximum in equation 7.11 is obtained from its first derivative and the resulting expressions for t_m and I_m are used to generate the reduced form expression.

$$\left(\frac{I}{I_m}\right)^2_{inst} = 1.9542\left(\frac{t_m}{t}\right)\left\{1-\exp\left[-1.2564\left(\frac{t}{t_m}\right)\right]\right\}^2 \qquad 7.12$$

In the other limiting case, the rate of nucleation is so slow that the number of growth sites changes significantly over an extended period and the nuclei have different ages. If the nucleation rate constant is sufficiently small such that $\left(N_o/A = \alpha/g\right) \to \infty$, and proceeding as described above, the reduced form expression for progressive nucleation becomes,

$$\left(\frac{I}{I_m}\right)^2_{prog} = 1.2254\left(\frac{t_m}{t}\right)\left\{1-\exp\left[-2.3367\left(\frac{t}{t_m}\right)^2\right]\right\}^2 \qquad 7.13$$

7.2 Results and Discussions

7.2.1 Single-step chronoamperometry

Single step chronoamperometry is an electrochemical technique in which the potential of the working electrode is stepped from an initial value to a desired one for nucleation and the resulting current, flowing through the working electrode due to faradaic processes, is measured over the time.[6] Details of the chronoamperometry measurements and the determination of integrated current at a given potential have already been discussed in Chapter 2. The major difference between this technique and the potential sweep techniques relies on the application of a fixed voltage instead of a voltage scan.[6] The three important parameters based on the chronoamperometry curves are: peak current (i_m), time taken to get peak current (t_m) and current (i). The former two parameters, peak current and time, are fundamental to study the metal nucleation process at the early stage of the electrodeposition process.

Single potential step chronoamperometry experiments to study the nucleation mechanism on the Au-MOP system were performed after a minimum of 5 hours of mixing the solutions to ensure the presence of only one redox active species, $Au^IPy_2^+$, thereby reducing the complexity in the system. Thus, before any nucleation studies were performed ageing of the solution was important as it avoided the presence of the Au(III) species. An aged solution of 0.25mM $KAuCl_4$ and 0.01M MOP in 0.1M NaCl allowed the homogenous reduction of the Au^{III} to form the kinetically stable Au^I species. A representative voltammogram of the aged AuMOP system is shown in Figure 7.3. The CV revealed the complete absence of the first peak associated with the two-electron reduction of $AuCl_2Py_2^+$, this implies that the dominant species in solution is $Au^IPy_2^+$, which will be

abbreviated as Au^{I} for the remainder of this Chapter. The cyclic voltammogram was initially performed on pristine ITO substrates to determine the exact peak potential (around -500mV) for the deposition experiments. After this CV, the ITO substrates would undergo stripping voltammetry to remove all the gold from the surface of the working electrode before the nucleation steps. For the nucleation studies, an overpotential is required to nucleate the centres [7] and so potentials negative to the peak potential were always used.

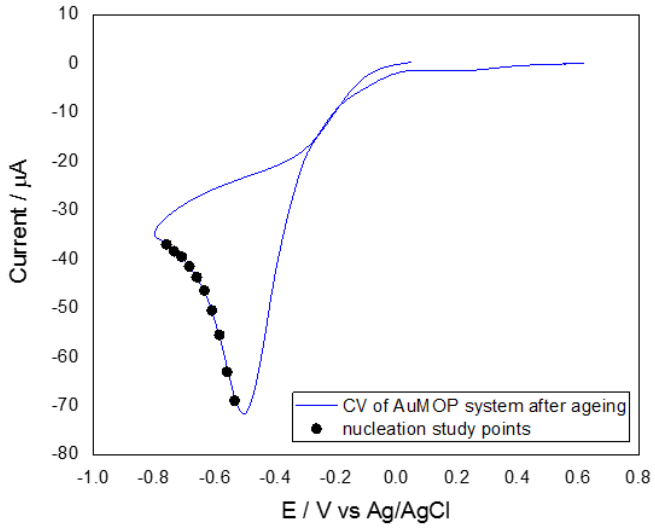

Figure 7.3. Cyclic voltammogram (20 mV/s) of an ITO working electrode in an aged solution (5 hours) of 0.25 mM $KAuCl_4$ aqueous solution, 0.1 M NaCl and 0.01 M 4-methoxypyridine.

The chronoamperometry curves for the electrodeposition process with different deposition voltages ranging from -800 mV to -500 mV were investigated to study the nucleation mechanism and are presented in the following Figure 7.4. The current transient curves of gold electrodeposition with different voltages were observed to be qualitatively very similar, with a characteristic current maximum that occurs at increasingly shorter times with increasingly larger overpotential. A sharp current decrease is observed at the very beginning of each transient and is attributed to the electric double layer charging and possible adsorption-desorption processes.[8] This current contains no analytical information about the nucleation and growth mechanism nor is it accounted for in the nucleation and growth models described above. Hence, this initial current

response is omitted from the analyses. As the gold ions diffuse to the cathode surface and undergo electron transfer reactions, an increase in the cathodic current is observed. This rise in current is attributed to each independent nucleus growing in size and/or an increase in the number of nuclei with the electroactive surface area of the electrode. Subsequently, the cathode current starts to decrease with the rise in the thickness of the diffusion layer. It is noted that the position of the current maximum increasingly overlaps the initial exponential current decay associated with double layer charging of the electrode-solution interface. This limits the step potentials that can be analysed in the nucleation and growth model to those positive of ~ -0.735V. This overall phenomenon verifies that gold electrodeposition on ITO surface exhibits a typical hemi-spherical or, in other words, a three-dimensional nucleation process.[9]

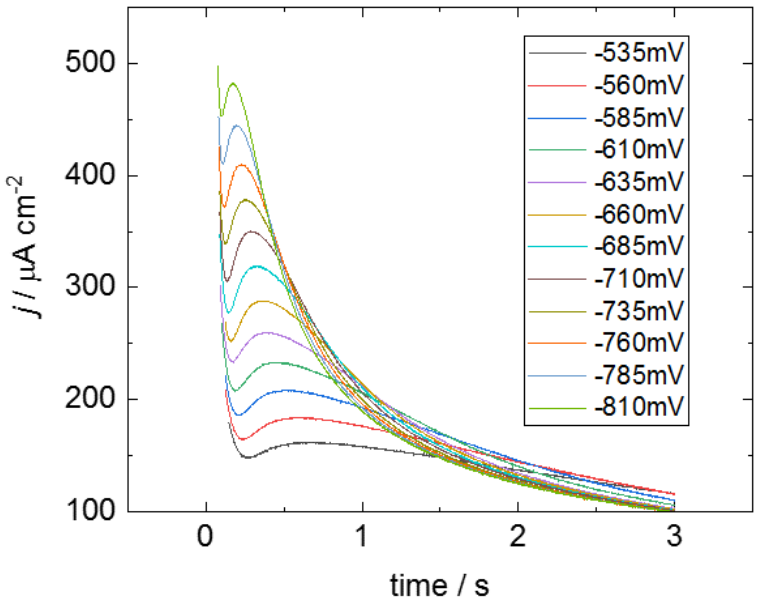

Figure 7.4. Chronoamperometric curves for different deposition voltages ranging from -810 mV to -535 mV.

7.2.2 Cottrell plot

The equations for both instantaneous and progressive nucleation include several possible fit parameters and the reliability of the fitting analyses is improved if some of these parameters can be determined independently. While this is not possible for the nucleation rate and active site

density, the diffusion coefficient can be obtained from a similar chronoamperometric experiment. At large overpotentials, the nucleation and growth processes are relatively rapid, and the measured current transients are dominated by planar diffusion of the redox active species to the electrode. The mathematical description of planar diffusion-controlled transients is well established and is known as the Cottrell equation.

$$j_{Cott} = \frac{I}{A} = zFc\left(D/\pi\right)^{1/2} t^{-1/2} \qquad 7.14$$

where j_{Cott} = current density, in unit A/cm^2, z = number of electrons, F = Faraday constant, 96485 C/mol, A = area of the (planar) electrode in cm^2, c = initial concentration of the reducible analyte in mol/cm^3, D = diffusion coefficient for species in cm^2/s and t = time in s. The current transient (i.e. the current measured over time when stepped to a potential) reveals a typical planar diffusion-controlled response as evidenced by the linear j vs $t^{1/2}$ plot as shown in Figure 7.5 and such plot allow the determination of diffusion coefficient, D.

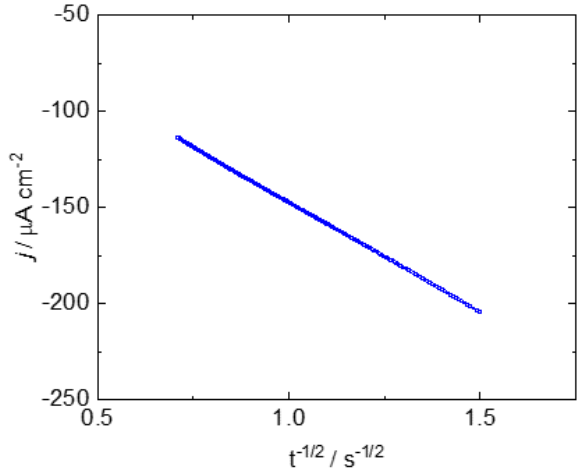

Figure 7.5. Plot of j vs $t^{-1/2}$ for the potential step experiment , -800 mV (blue line), in a solution of 0.25 mM $KAuCl_4$ aqueous solution, 0.1 M NaCl and 0.01 M 4-methoxypyridine.

The Cottrell equation gives the current response, when a potential is a step function of time and any deviation form linearity could be a sign of other processes, such as association /dissociation of ligand, associated with the redox event. Here, in the Au-MOP system, a linear j vs $t^{1/2}$ plot is

observed, and various current transients were analysed at long times where the current is dominated by planar diffusion. The Cottrell plot from the potential step experiment, -800mV (blue line), in a solution of 0.25 mM $KAuCl_4$ aqueous solution, 0.1 M NaCl and 0.01 M 4-methoxypyridine is shown in Figure 7.5. The value of diffusion coefficient, D, has been established as 1.8×10^{-5} cm^2 s^{-1} for the $(Au^IPy_2)^+$ species with more recent set of measurements made by my colleague.

7.2.3 Nucleation rate constant (A) and number density (N_0)

The nucleation rate constant (A) and number density (N_0) were obtained form the current maxima of the potentiostatic experiments by means of a numerical method described by equation 7.10. Thus, in order to extract N_0 and A, the current transients from Figure 7.4 were first normalised by the peak current and plotted as a function of the dimensionless parameter t/t_m and then fit to equation 7.10. The fits obtained were compared to the expected curves for instantaneous and progressive nucleation as both functions rely only on the coordinates of the experimentally observed current maximum as shown in Figure 7.6.

Qualitatively, it can be seen from the figure that the transients at low overpotential fit rather well to the limiting case of instantaneous nucleation and growth whereas the transients at larger overpotentials are intermediate between the two limiting scenarios. Brouwer and Baker (BB) proposed a similar model that describes the simultaneous operation of the nucleation and growth processes and shows the transients existing between the limiting cases of instantaneous and progressive nucleation and growth.[10] The trend is further verified by the fitting analysis of Equation 7.10 from which both A and N_o can be extracted and plotted as a function of step potential (Figure 7.7).

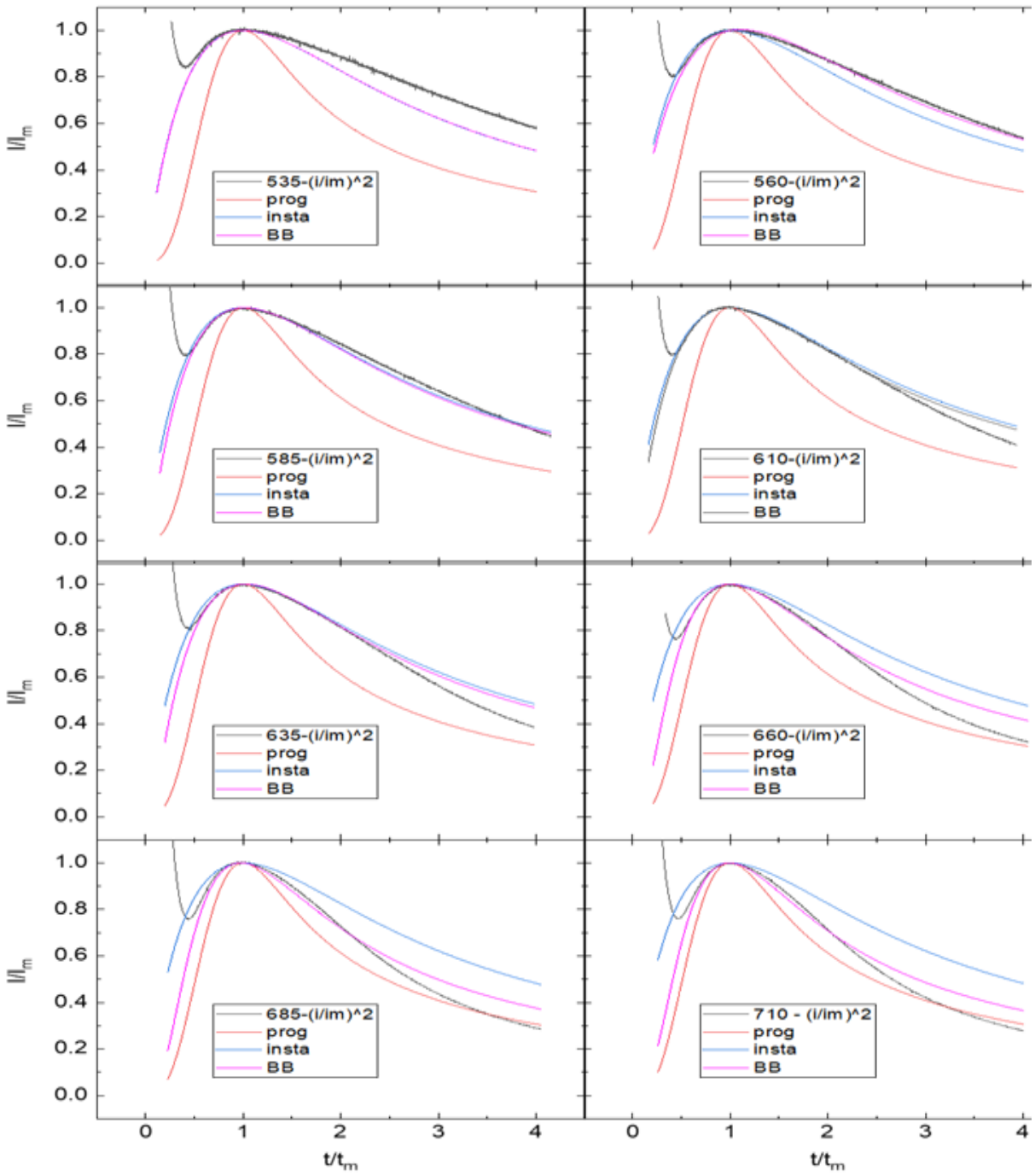

Figure 7.6. Normalised experimental plots of current transients for electrodeposition of gold at different potentials (black line) along with fits to equation 7.10 (pink line) compared to the theoretical curves corresponding to the models for progressive (orange line) and instantaneous (blue line) nucleation.

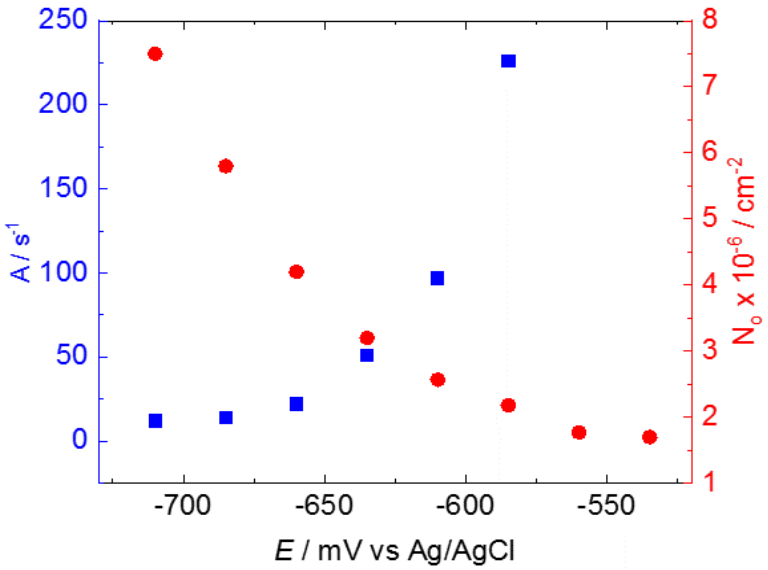

Figure 7.7. Plot of nuclear number density, No, and nucleation rate constant, A, as a function of overpotential.

As expected, the number of active sites increases as the driving potential for reduction is increased (increasingly negative step potentials), however, the decrease in the rate of nucleation with overpotential is counterintuitive and different from previous reports of nucleation and growth.[4, 11]. This is a surprising result and a satisfactory explanation of this result is not obvious. It is possible that the complexity of the fitting provides non-physical results or perhaps the role of concurrent reactions such as disproportionation perturb the current response from the simple model developed by Scharifker and co-workers.

7.2.4 Nucleation and growth analysis

Certain trials were performed to grow the nucleated metal particles after the initial pulse, when an overpotential, η, was applied. The SEM images, as shown in Figures 7.8 and 7.9 for the pulsed growth depositions at different growth time and charge passed, gives a platform to understand how the shapes and sizes of the crystals can be controlled using electrochemistry.

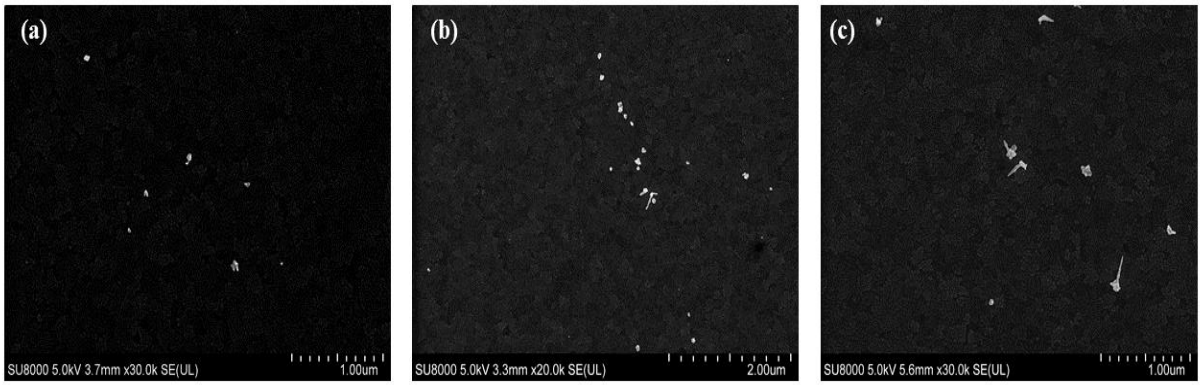

Figure 7.8. SEM images of Au nanostructures from 0.1 M MOP and 0.25 mM $KAuCl_4$ in 0.1 M NaCl nucleated at -800 mV(0.5s) and growth at (a) -500 mV(1s), (b) -500 mV(1.5s), (c) -500 mV(2s) when a charge of 1000 µC cm^{-2} was passed.

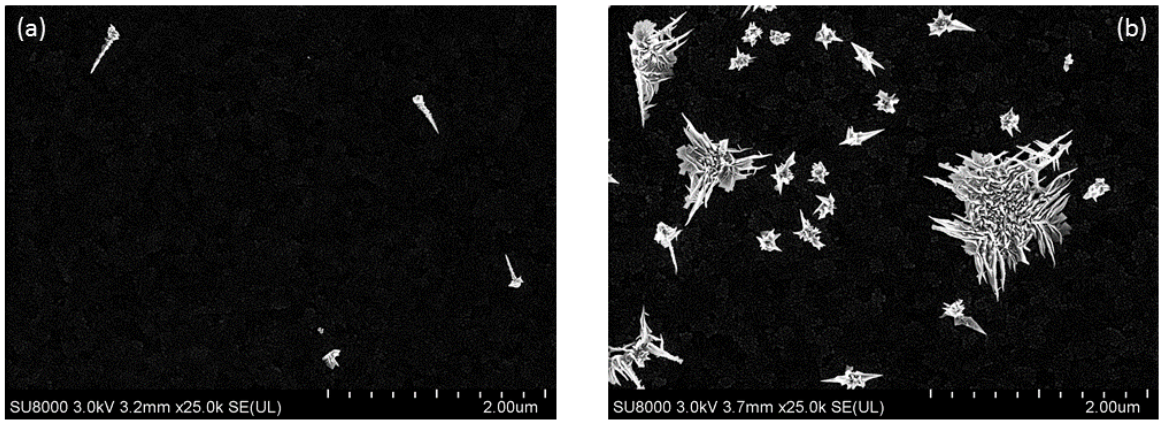

Figure 7.9. SEM images of Au nanostructures from 0.1 M MOP and 0.25 mM $KAuCl_4$ in 0.1 M NaCl (a) nucleated at -800 mV(0.5s) and growth at -500 mV(5s) with various charge densities (a) 1000 µC cm^{-2} (b) 6000 µC cm^{-2}

Figure 7.8 shows how the size and shape of the nuclei varies at the growth potential (-500 mV) for different period but same charge passed on the ITO electrode surface, whereas Figure 7.9 shows the growth of the nanoparticles at various charge densities. Although the literature reviews the size-selective electrodeposition of certain metal particles using a slow-growth method [12], this aspect has been less emphasized in this thesis work. Understanding the nucleation model of the

electrochemical phase formation of gold nanocrystals on the ITO surface had been the preference throughout this chapter.

7.3 Conclusions

Nucleation and growth study is the key to tune sizes and shapes of the nanostructures and hence analysing and understanding the AuMOP system using nucleation models is essential. The nucleation and the growth behaviour of the AuMOP system presented in this chapter shows that the chronoamperometric transients at lower overpotential fit well to the limiting case of instantaneous nucleation and growth whereas the transients at larger overpotentials are intermediate between the two limiting scenarios, instantaneous and progressive nucleation and growth. The current maximum is shown to provide the information required for the simultaneous evaluation of the nucleation rate (A) and nuclei number density (N_0) on the surface of the ITO electrode. It is interesting to see the decreasing trend of the rate of nucleation with overpotential, whereas the number of active sites is shown to increase with increase in the negative step potentials. The role of disproportionation reaction is once again verified in this chapter by extracting the diffusion coefficient of the $Au^{I}Py_2^{+}$ species thereby validating the nucleation behaviour of the system.

Thus, by understanding the nucleation and growth mechanism, one can control the size, shape and density of the deposited nanoparticles. The literature shows how the individual metal particles on the electrode surface can grow independently, from the number and proximity of the neighbouring particles, with the same growth rate.[13] With this uncoupled growth regime, extremely narrow particle size distributions can thus be obtained by varying electrodeposition and nucleation density conditions.

7.4 References

1. Dalmaschio, C.J., C. Ribeiro, and E.R. Leite, *Impact of the colloidal state on the oriented attachment growth mechanism.* Nanoscale, 2010. **2**(11): p. 2336-2345.

2. Thanh, N.T.K., N. Maclean, and S. Mahiddine, *Mechanisms of Nucleation and Growth of Nanoparticles in Solution.* Chemical Reviews, 2014. **114**(15): p. 7610-7630.

3. Gunawardena, G., et al., *Electrochemical nucleation. Part I. General considerations.* J. Electroanal. Chem. Interfacial Electrochem., 1982. **138**(2): p. 225-39.

4. Scharifker, B. and G. Hill, *Theoretical and experimental studies of multiple nucleation.* Electrochim. Acta, 1983. **28**(7): p. 879-89.

5. Scharifker, B.R. and J. Mostany, *Three-dimensional nucleation with diffusion controlled growth: Part I. Number density of active sites and nucleation rates per site.* Journal of Electroanalytical Chemistry and Interfacial Electrochemistry, 1984. **177**(1): p. 13-23.

6. Pinto, A.M.F.R., V.B. Oliveira, and D.S. Falcão, *4 - Experimental methods of characterization*, in *Direct Alcohol Fuel Cells for Portable Applications*, A.M.F.R. Pinto, V.B. Oliveira, and D.S. Falcão, Editors. 2018, Academic Press. p. 113-155.

7. Komsiyska, L. and G. Staikov, *Electrocrystallization of Au nanoparticles on glassy carbon from HClO4 solution containing [AuCl4]−.* Electrochimica Acta, 2008. **54**(2): p. 168-172.

8. Bosco, E. and S.K. Rangarajan, *Electrochemical phase formation: time-dependent nucleation and growth rates.* J. Chem. Soc., Faraday Trans. 1, 1981. **77**(3): p. 483-95.

9. Hills, G.J., D.J. Schiffrin, and J. Thompson, *Electrochemical nucleation from molten salts. I. Diffusion controlled electrodeposition of silver from alkali molten nitrates.* Electrochim. Acta, 1974. **19**(11): p. 657-70.

10. Brouwer, D.H. and M.D. Baker, *Nucleation and Growth of Silver at Zeolite A-Modified Electrodes.* The Journal of Physical Chemistry B, 1997. **101**(49): p. 10390-10397.

11. Mostany, J., J. Mozota, and B.R. Scharifker, *Three-dimensional nucleation with diffusion controlled growth. Part II. The nucleation of lead on vitreous carbon.* J. Electroanal. Chem. Interfacial Electrochem., 1984. **177**(1-2): p. 25-37.

12. Liu, H., et al., *Size-selective electrodeposition of meso-scale metal particles: a general method.* Electrochim. Acta, 2001. **47**(5): p. 671-677.

13. Liu, H. and R.M. Penner, *Size-Selective Electrodeposition of Mesoscale Metal Particles in the Uncoupled Limit.* The Journal of Physical Chemistry B, 2000. **104**(39): p. 9131-9139.

CHAPTER 8

SUMMARY AND CONCLUSIONS

8.1 Summary of work presented

The use of an electrochemical approach to elucidate certain fundamental aspects of anisotropic nanoparticle formation on conductive electrodes has been exemplified in this thesis. It has been demonstrated that a study in this direction, i.e., understanding the homogenous chemistry that leads to the formation of anisotropic nanostructures provides insightful information about tuning the size and shape of a nanoparticle. The role of 4-methoxypyridine as a ligand stabilizer for successfully stabilizing gold nanoparticles has been the core part of this thesis. Two main projects in this regard have been discussed in this thesis: (1) Electrochemical formation of highly anisotropic gold nanostructures stabilized by MOP, (2) Postulating a new kinetic model for the complex Au-MOP system by studying the stopped-flow methods of UV-Vis Spectrophotometry. While efforts towards accomplishing these two major goals have been the highlight of this thesis, relevant fundamental studies on the electrochemical aspect of different coinage metals and understanding the nucleation and growth study of the Au-MOP system have also been the subject of discussion in other chapters.

An electrochemical survey of the coinage metals in forming nanoparticles stabilized by MOP was the first section of the thesis work (Chapter 3). It was instigated from the observation that the presence of a pyridine capping agent can be used to stabilize metal nanoparticles. Research was performed on the synthesis of the colloidal nanoparticle solution. By analyzing the results from UV-Vis spectroscopy and transmission electron microscopy, an evaluation of the anisotropy in the MOP stabilized metal nanoparticles has been done. This chapter's key aspect was to reveal that

4-methoxypyridine ligand stabilizes the gold nanoparticles, imparting anisotropy in their structures than other coinage metals of interest such as silver and copper. Cyclic voltammetric studies also showed a two-reduction process in the Au-MOP electrochemistry which was an interesting part of the thesis work.

A detailed study of the electrochemical behavior of Au-MOP complexes in aqueous solutions followed the initial survey. The results summarised in Chapter 4 and 5 provide compelling evidence of the existence of Au^{I}–MOP complexes but, just as importantly, allow new insight into the electrochemistry pertinent to the formation of electrodeposited Au nanoparticles. Although the observation mentioned the core differences between MOP-directed growth of nanocrystals formed by chemical and electrochemical reduction was interesting, these differences are considered to be likely caused by several key factors relating to the rates of nucleation and mass transport. The shape directing role of 4- methoxypyridine was confirmed through several ways in this thesis work. One of the main experiments was to perform electrodepositions in the absence of the pyridine derivative, and the other method was to change the supporting electrolyte to check if the shape-directing properties were attributable to preferential halide adsorption on Au{111} facets. This work showed that there is no significant difference in the anisotropy of gold nanostructures when chloride ions are replaced with fluoride ions as the supporting electrolyte. This insight into the electrochemistry part of creating nanostructures helped to engineer densely packed films of highly anisotropic Au nanocrystals on conductive glass (indium tin oxide, ITO) substrates that illustrated excellent suitability of these interfaces for FT-Raman applications utilizing near-IR excitation sources.

The mechanism for the reduction process of Au(III) to Au(I) in the presence of MOP has been proposed in Chapter 4. A detailed study of the kinetics of the Au-MOP system in aqueous solutions is described using spectrophotometric methods. Three different reaction pathways were postulated with the help of stopped- flow absorption spectroscopy to understand the kinetics of the Au-MOP system. Although various analysis such as Mass spectrometry was carried out, no direct evidence of the reductant was obtained. However, based on thermodynamic arguments it is very likely that 4-methoxypyridine gets oxidized to form a pyridine N-oxide. The Au-MOP system reveals a spontaneous reduction of the Au^{III} complex, and the existence of $AuPy_2^+$ has been conclusively determined. Understanding the intermediates and the mechanism of the Au-MOP reaction was the

key aspect of this chapter. Understanding the homogenous chemistry of the Au-MOP system was one of the crucial steps to undertake to perform the nucleation and growth study of the gold nanostructures. This chapter has thus made successful attempts to extract the kinetic parameters from the stopped-flow experiments and propose a kinetic model to the Au-MOP system of study.

Apart from the interest growing in the nanoparticle research, understanding the reaction chemistry as well as the nucleation barrier of each system is a fundamental problem in the field of nanoscience. The importance of the nucleation study needs to be highlighted as it gives the underlying idea to tune the sizes and shapes of the nanostructures that could be used in various application fields depending on their different functional desirability. Chapter 7 has shown the type of nucleation that occurs on conductive electrodes with the Au-MOP system of reference, which led to the growth of the highly anisotropic gold nanostructures. Chronoamperometric studies performed in this chapter has helped to analyse the nucleation and growth of the gold nuclei and deduce the type of nucleation - instantaneous or progressive, that occurs for the respective gold nanostructures stabilized by MOP. Thus, the measures necessary to tune the shapes and size of the gold nanostructures through homogenous nucleation and growth study on conductive electrodes has been portrayed in this chapter.

In summary, the research presented in this thesis has contributed to the successful culmination of major objectives in the project. A profound understanding of the kinetics of the complex Au-MOP system (Chapter 4) followed by the electrochemical behaviour of the Au-MOP system (Chapter 5) and their characteristics and application to SERS (Chapter 6) was established. In addition to the perception of MOP's capacity as the capping agent/stabilizing agent for different coinage metals (Chapter 3) and its shape-directing formation of gold nanoparticles, a brief study on the nucleation and growth study of the anisotropic nanoparticles was also conducted (Chapter 7). The chronoamperometric results from the nucleation chapter are promising as it would benefit the nanoparticle research field by forming well-defined arrays of highly anisotropic gold nanoparticles for various applications.

8.2 Scope of future research

This thesis work has provided an insight into the complex chemistry of the Au-MOP system. However, the key to control over the design of anisotropic gold nanoparticles so as to tune their shapes and size to the right perfection needs more elaborate study. By adjusting the deposition parameters, the surface morphology and thickness of the anisotropic nanoparticles electrochemically deposited on conductive surfaces can be altered.[1] More effort and time is required to study the effects on how the changes in the deposition conditions can alter anisotropy in nanostructures. In light of the body of work summarised in this thesis, more elaborate studies on the nucleation and growth studies is required. New chronoamperometric experiments coupled with imaging techniques needed to be designed to further validate the nucleation models described in this thesis. It would also be interesting to consider the effect of functionalization of pyridine molecules on deposition behaviour or a detailed mechanistic study of a different group for adsorption than N-Au bond as a near-future research goal. Further progress of the research can be pursued in using the gold nanodaggers of the perfect size and shape for two main applications - electrocatalysis and SERS.

The use of highly faceted nanostructures with dagger-shaped protrusions of the sub-100nm scale is of great demand in electrocatalysis.[2] The main challenge faced so far in the field of nanotechnology is to fabricate and combine nanoscale building blocks to make useful devices for multiple purposes. Fabricating the nanostructures to the right size for electrocatalytic oxygen reduction is very critical as the larger sized (> 200 nm) nanoparticles are not electrocatalytically active.[3, 4] Therefore, it gets crucial when it drops down to the smaller sized nanostructures. Most of the nanostructures electrodeposited on solid substrates find their applications in electrocatalysis as well as SERS. Higher catalytic activity and better stability for catalysis and better SERS detectors for *in-situ* and *in-operando* studies needs a structure-based analysis. Though it is quite a challenge to achieve the required size and shape of the metal nanostructures, the nucleation study is the tool basis for this research. In part, the success of the story primarily depends on understanding the reaction chemistry of the system and the nucleation model study, the applications of these nanostructures remained for the future goal of this research work.

The control of homogenous and density-controlled metallic nanostructures on conductive substrates is in great demand as it produces good reproducibility and high sensitivity in SERS measurements.[5] Although preliminary studies in this thesis had shown that MOP stabilized gold nanostructures were suitable SERS substrates, detailed research on the application level is one of the potential scopes for future work. The uniform and roughened surface morphology of the metal nanostructures on solid substrates are considered desirable SERS-active substrates with an ultra-sensitive detection limits.[6-9] These solid-type SERS substrates can be used as potential sensors to detect biological molecules with a real-time diagnosis.[10] SERS detection with a picomolar analytical range is a very promising spectroscopic analysis, which, in comparison to other methods such as electrochemical and fluorescence detection, has a primary *in-vivo* application.

8.3 References

1. Sajanlal, P.R., et al., *Anisotropic nanomaterials: structure, growth, assembly, and functions.* Nano reviews, 2011. **2**: p. 10.3402/nano.v2i0.5883.

2. Plowman, B., et al., *Gold nanospikes formed through a simple electrochemical route with high electrocatalytic and surface enhanced Raman scattering activity.* Chemical communications (Cambridge, England), 2009. **33**: p. 5039-41.

3. El-Deab, M.S. and T. Ohsaka, *An extraordinary electrocatalytic reduction of oxygen on gold nanoparticles-electrodeposited gold electrodes.* Electrochem. Commun., 2002. **4**(4): p. 288-292.

4. Hyun, M., et al., *Simple Electrodeposition of Dendritic Au Rods from Sulfite-Based Au(I) Electrolytes with High Electrocatalytic and SERS Activities.* Electroanalysis, 2011. **23**(9): p. 2030-2035.

5. Camden, J.P., et al., *Controlled Plasmonic Nanostructures for Surface-Enhanced Spectroscopy and Sensing.* Acc. Chem. Res., 2008. **41**(12): p. 1653-1661.

6. Bu, Y. and S. Lee, *Optimizing surface-enhanced Raman scattering-active Au nanostructures coated on indium-doped tin oxide glass by combining chemical assembly and electrodeposition methods.* Jpn. J. Appl. Phys., 2013. **52**(10, Pt. 2): p. 10MD02/1-10MD02/4.

7. Gupta, R. and W.A. Weimer, *High enhancement factor gold films for surface enhanced Raman spectroscopy.* Chem. Phys. Lett., 2003. **374**(3,4): p. 302-306.

8. Ye, J., et al., *Excitation wavelength dependent surface enhanced Raman scattering of 4-aminothiophenol on gold nanorings.* Nanoscale, 2012. **4**(5): p. 1606-1611.

9. Yun, S., et al., *Linker-Molecule-Free Gold Nanorod Films: Effect of Nanorod Size on Surface Enhanced Raman Scattering.* J. Phys. Chem. C, 2009. **113**(31): p. 13551-13557.

10. Bu, Y. and S.-W. Lee, *Flower-like gold nanostructures electrodeposited on indium tin oxide (ITO) glass as a SERS-active substrate for sensing dopamine.* Microchim. Acta, 2015. **182**(7-8): p. 1313-1321